INSTITUTO DE PESQUISAS ENERGÉTICAS E NUCLEARES
Autarquia Associada à Universidade de São Paulo

SYNTHESIS AND RADIOLABELING OF A NITROFURAN DERIVATE WITH ^{18}F FOR IDENTIFICATION OF AREAS OF HYPOXIA IN THE TUMOR MICROENVIRONMENT

YASNIEL BABI ARAUJO

Tese apresentada como parte dos requisitos para obtenção do Grau de Doutor em Ciências na Área de Tecnologia Nuclear - Aplicações

Orientador:
Prof. Dr. Emerson Soares Bernardes

São Paulo
2024

INSTITUTO DE PESQUISAS ENERGÉTICAS E NUCLEARES
Autarquia Associada à Universidade de São Paulo

SYNTHESIS AND RADIOLABELING OF A NITROFURAN DERIVATE WITH ^{18}F FOR IDENTIFICATION OF AREAS OF HYPOXIA IN THE TUMOR MICROENVIRONMENT

Versão Original

YASNIEL BABI ARAUJO

Tese apresentada como parte dos requisitos para obtenção do Grau de Doutor em Ciências na Área de Tecnologia Nuclear - Aplicações

Prof. Dr. Emerson Soares Bernardes

São Paulo
2024

Fonte de Financiamento: CNPq

Como citar:

BABI ARAUJO, Y. ***Synthesis and radiolabeling of a nitrofuran derivate with 18F for identification of areas of hypoxia in the tumor microenvironment***. 2024. 158 f. Tese (Doutorado em Tecnologia Nuclear), Instituto de Pesquisas Energéticas e Nucleares, IPEN-CNEN, São Paulo. Disponível em: ‹http://repositorio.ipen.br/› (data de consulta no formato: dd/mm/aaaa)

Ficha catalográfica elaborada pelo Sistema de geração automática da Biblioteca IPEN, com os dados fornecidos pelo(a) autor(a).

Babi Araujo, Yasniel
Synthesis and radiolabeling of a nitrofuran derivate with 18F for identification of areas of hypoxia in the tumor microenvironment / Yasniel Babi Araujo; orientador Emerson Soares Bernardes. -- São Paulo, 2024.
158 f.

Tese (Doutorado) - Programa de Pós-Graduação em Tecnologia Nuclear (Aplicações) -- Instituto de Pesquisas Energéticas e Nucleares, São Paulo, 2024.

1. Radioquimica. 2. Sintese Orgânica. 3. Hypoxia. 4. Imagem Molecular. 5. Tomografía por Emissão de Pósitrons. I. Soares Bernardes, Emerson, orient. II. Título.

APPROVAL SHEET

Author: Yasniel Babi Araujo

Title: Synthesis and radiolabeling of a nitrofuran derivate with ^{18}F for identification of areas of hypoxia in the tumor microenvironment.

Thesis presented to the Postgraduate Program in Nuclear Technology of the University of São Paulo for obtaining the title of Doctor of Sciences

Date:

Examining Committee

Prof. Dr. _____

Institution: _____ Judgement:_____

Prof. Dr. _____

Institution: _____ Judgement:_____

Prof. Dr. _____

Institution: _____ Judgement:_____

Prof. Dr. _____

Institution: _____ Judgement:_____

Prof. Dr. _____

Institution: _____ Judgement:_____

Para la familia, para mi mamá, y para mi hijo como fuente de inspiración en el futuro

Agradecimientos

Agradezco primero a Dios y todo lo que existe por haberme permitido llegar hasta aquí. A mis padres y a toda mi familia por la educación y por enseñarme todos los valores para convertirme en el hombre que soy hoy.

Le agradezco muchísimo a mi orientador, Dr. Emerson Soares Bernardes por la oportunidad que me dio de venir a Brasil y comenzar otra vida, y por la posibilidad de adentrarme en este maravilloso mundo de la ciencia y la investigación. Le agradezco infinitamente por los desafíos y por todo el conocimiento adquirido durante estos 5 años. Muchísimas gracias al Consejo Nacional de Desarrollo Científico y Tecnológico (CNPq), por financiar mi beca en Brasil PEC-PG, proceso 142245/2018-6 desde 07/2018 hasta 04/2023. No hubiera sido posible desarrollar este trabajo sin la ayuda financiera proporcionada. Existe mucho talento y personas con ganas de trabajar en este mundo de la investigación, y ustedes como institución hacen eso posible.

Agradecer a la Universidad de São Paulo (USP) por acogerme y permitirme estudiar y aprender muchísimo durante este tiempo. Al Instituto de Pesquisas Energéticas e Nucleares (IPEN/CNEN); al Centro de Radiofarmacia (CR), Centro de aceleradores de ciclotrones IPEN; colaboradores del Bioterio; a los empleados de la división de posgrado del IPEN. y todos los trabajadores y personas asociadas a estas instituciones por hacer posible este sueño y por la ayuda brindada.

Agradecer a todos los integrantes del grupo Imagen Molecular en Oncología (IMemO), por las vivencias y experiencias compartidas; ayudas, historias y enseñanzas para tornarnos mejores investigadores.

Gracias a mi esposa, gracias por tu dedicación Ismar, paciencia y consejos para llegar hasta aquí. Este triunfo también es tuyo.

Le agradezco mucho a la familia Alberto, siempre los recordaré con mucho cariño.

Agradecer a todos los profesores y educadores que contribuyeron a mi formación, desde niño y hasta hoy. Gracias por su dedicación, esfuerzo y paciencia. No hubiera sido posible llegar hasta aquí sin ustedes.

Agradecer a la Dra. Ivonne Carvalho de la Facultad de Ciencias Farmacéuticas de la USP de Ribeirão Preto por acogerme en su laboratorio. A Filipe Canto por los conocimientos compartidos, y por toda la ayuda en las síntesis llevadas a cabo.

Gracias a la Facultad de Farmacia de la USP de São Paulo por la posibilidad de utilizar equipos y materiales en este trabajo. Gracias Jeanine, Mónica e Inés.

Gracias a la profesora Dra. Daniela Martins de la UFF, RJ, por la oportunidad de aprender junto a ella y sus alumnos, y por los conocimientos adquiridos en su laboratorio.

Agradecer a la Agencia Internacional de Energía Atómica (IAEA), al Dr. Frank Wuest y a todos los integrantes de su grupo por la posibilidad de utilizar su laboratorio y equipos que fueron de mucha ayuda para la terminación de este trabajo.

A los miembros del tribunal examinador por aceptar la invitación, por sus opiniones críticas y sugerencias.

Gracias a todas las personas e instituciones que ayudaron en la realización de este trabajo, y claro agradecer a todos los que contribuyeron en mi formación académica y de valores durante toda mi vida.

Muchas gracias

“El conocimiento es la virtud, y sólo si se sabe se puede divisar el bien.”

Sócrates

ABSTRACT

BABI ARAUJO, Y. ***Synthesis and radiolabeling of a nitrofuran derivate with ^{18}F for identification of areas of hypoxia in the tumor microenvironment.*** 2024, 156 p. Tese (Doutorado em Tecnologia Nuclear) Instituto de Pesquisas Energéticas e Nucleares – IPEN-CNEN/SP. São Paulo.

Hypoxia, one of the hallmarks of cancer, is a pathological condition referred to a relatively low (generally < 2%) oxygen content compared to normal status in a given organ, tissue, or cell type. Positron Emission Tomography (PET) is a non-invasive molecular imaging technique widely known for studying hypoxia mostly employing 2-nitroimidazole-based radiotracer probes that directly report on oxygen levels with high specificity and spatial resolution. In this regard, [^{18}F]FMISO is the most widely used hypoxia imaging radiopharmaceutical, but its high lipophilicity causes slow tracer accumulation, slow plasma clearance, and low tumor-to-background contrast. The mechanism of action of hypoxia-specific radiotracers lies on the selective reduction of the nitroimidazole moiety under hypoxic conditions, but other nitroaromatic compounds with improved reduction capabilities in the absence of oxygen could be used. The objective of this work was to synthesize and evaluate a nitrofuran-based radiotracer probe for detection of hypoxic areas in the tumor microenvironment, (E)-1-(4-[^{18}F]-fluorophenyl)-3-(5-nitrofuran-2-yl)prop-2-en-1-one, baptized as [^{18}F]FNFP, and compare it with [^{18}F]FBNA, a novel hypoxia radioligand synthetized and characterized in a previous work. Initially, precursors for [^{18}F]-labelling and cold standards [^{19}F]FNFP and [^{19}F]FBNA were prepared and characterized by spectroscopic techniques, with a novel improved synthesis in the case of the latter compared to the method reported. Late-stage radiofluorination allowed the introduction of the [^{18}F]-fluoride in a one-step reaction without azeotropic drying, obtaining both [^{18}]FFNFP and [^{18}]FFBNA with >99% radiochemical purity, radiochemical yields of 38,4±3% and 39,1±5% (n=3), total synthesis time of 85 and 70 minutes, and high molar activities of 41.56 GBq/µmol and 43,02 GBq/µmol, respectively. [^{18}]FFNFP was found to be stable in Phosphate-buffered saline (PBS) and serum for up to 6 hours and more hydrophilic than [^{18}F]FMISO ($\log_{10}P$=2.06), with the same partition coefficient as [^{18}F]FBNA ($\log_{10}P$=1.05). PET/CT images using an

MKN-45 gastric cancer tumor model in mice showed that [^{18}F]FNFP, a chalcone derivate, is rapidly excreted by a hepato-biliary-intestinal-renal clearance with no tumor uptake. Similar to its counterparts chalcone-based radiotracers, has a rapid washout from the brain with a high uptake in this organ in the first 15 minutes after injection. *Ex vivo* biodistribution studies showed no interesting tumor uptake for [^{18}F]FNFP. Different from the 2-nitroimidazole-based radiotracer [^{18}F]FBNA, the 5-nitrofuran derivate [^{18}F]FNFP was not nearly as effective as the former in identifying hypoxic regions in the tumor microenvironment, perhaps due to its rapid clearance.

Keywords: [^{18}F]FNFP, [^{18}F]FBNA, synthesis, hypoxia, PET imaging, biological evaluation.

RESUMO

BABI ARAUJO, Y. ***Synthesis and radiolabeling of a nitrofuran derivate with ^{18}F for identification of areas of hypoxia in the tumor microenvironment.*** 2024, 155 p. Tese (Doutorado em Tecnologia Nuclear) Instituto de Pesquisas Energéticas e Nucleares – IPEN-CNEN/SP. São Paulo.

A hipóxia, uma das características do câncer, é uma condição patológica referida a um conteúdo de oxigênio relativamente baixo (geralmente < 2%) em comparação com o estado normal em um determinado órgão, tecido ou tipo de célula. A tomografia por emissão de pósitrons (PET) é uma técnica de imagem molecular não invasiva amplamente conhecida por estudar hipóxia, empregando principalmente radiotraçadores à base de 2-nitroimidazol que relatam diretamente os níveis de oxigênio com alta especificidade e resolução espacial. Nesse sentido, o [^{18}F]FMISO é o radiofármaco para imagem de hipóxia mais amplamente utilizado, mas sua alta lipofilicidade causa acúmulo lento de traçador, depuração plasmática lenta e baixo contraste tumor-fundo. O mecanismo de ação dos radiotraçadores específicos para hipóxia reside na redução seletiva da porção nitroimidazol sob condições hipóxicas, mas poderiam ser utilizados outros compostos nitroaromáticos com capacidades de redução melhoradas na ausência de oxigénio. O objetivo deste trabalho foi sintetizar e avaliar um novo radiotraçador à base de nitrofurano para detecção de áreas hipóxicas no microambiente tumoral, (E)-1-(4-[^{18}F]-fluorofenil)-3-(5-nitrofuran-2 -il)prop-2-en-1-ona, batizado como [^{18}F]FNFP, e compará-lo com [^{18}F]FBNA, um novo radioligante de hipóxia sintetizado e caracterizado em trabalho anterior. Inicialmente, precursores para marcação com [^{18}F] e os padrões frios [^{19}F]FNFP e [^{19}F]FBNA foram preparados e caracterizados por técnicas espectroscópicas, com uma nova síntese melhorada no caso deste último em comparação com o método publicado. A radiofluoração em estágio avançado permitiu a introdução do [^{18}F]-fluoreto em uma reação de uma etapa sem secagem azeotrópica, obtendo tanto [^{18}]FFNFP quanto [^{18}]FFBNA com >99% de pureza radioquímica, rendimentos radioquímicos de 38,4±3% e 39,1±5% (n=3), tempo total de síntese de 85 e 70 minutos e atividades molares elevadas de 41,56 GBq/µmol e 43,02 GBq/µmol, respectivamente. [^{18}]FFNFP foi estável em solução salina tamponada

com fosfato (PBS) e soro por até 6 horas e foi considerado mais hidrofílico que [^{18}F]FMISO ($log_{10}P=2.06$), com o mesmo coeficiente de partição que [^{18}F]FBNA ($log_{10}P=1,05$). Imagens PET/CT usando um modelo de tumor de câncer gástrico MKN-45 em camundongos mostraram que [^{18}F]FNFP, um derivado da chalcona, é rapidamente excretado por uma depuração hepato-biliar-intestinal-renal sem captação tumoral. Semelhante aos radiotraçadores à base de chalcona, apresenta uma rápida eliminação do cérebro com alta captação neste órgão nos primeiros 15 minutos após a injeção. Estudos de biodistribuição *ex-vivo* também não mostraram captação tumoral interessante para [^{18}F]FNFP. Diferente do radiotraçador baseado em 2-nitroimidazol [^{18}F]FBNA, o derivado de 5-nitrofurano [^{18}F]FNFP não foi eficaz quanto o primeiro na identificação de regiões hipóxicas no microambiente tumoral, talvez devido à sua rápida depuração.

Palavras chaves: [^{18}F]FNFP, [^{18}F]FBNA, síntese, hipoxia, imagem PET, avaliação biológica.

1 INTRODUCTION

Cancer, a worldwide public health problem, comprises a large group of diseases in which abnormal cells divide uncontrollably and can invade surrounding tissues and organs [1]. At present, cancer is the second leading cause of death globally only behind cardiovascular diseases [2], and in Brazil 704,000 new cases of cancer are expected for the 2023-2025 period [3].

Hypoxia, one of the most important hallmarks of cancer [4, 5], is a condition where oxygen levels are below the normal physiological concentration in tissues (4-9%) [6], and hypoxic tumors are associated with poor prognosis, an increased risk of invasion and metastasis, and resistance to chemo and radiation therapies [4, 5, 7, 8]. At this time, the gold standard for direct *in vivo* determination of tumor oxygenation is an oxygen electrode, commonly referred as “Eppendorf electrode” or “polarographic electrode”, which suffers from several drawbacks such as its invasive nature, sensitivity for sampling bias and that only easily approachable tumors can be studied [9, 10].

As stated before, hypoxic tissues are more resistant to the effects of radiation than well-oxygenated ones, and to achieve the same level of cytotoxicity, hypoxic cells require about three times the radiation dose that normoxic cells need [11]. Several strategies have been studied and developed to improve the radiosensitivity of hypoxic cells within solid tumors, such as fractionated radiotherapy, increased oxygen delivery, hypoxia inducible factor (HIF)-1 inhibitors, and radiosensitizers [12].

Early on, these hypoxic cell sensitizers were classified into different categories depending on their mechanism of DNA damage and repair by pioneers on the radiotherapy field: (a) suppression of intracellular thiols or other endogenous radioprotective substances; (b) formation of cytotoxic substances by radiolysis of the radiosensitizer; (c) inhibitors of repair of biomolecules; (d) thymine analogs that can incorporate into DNA; and (e) oxygen mimics that have electrophilic activity [13, 14]. With the continuous technological innovation in the field and the discovery of several mechanisms of action for radiosensitization,

radiosensitizers were classified into three categories based on their structures: small molecules, macromolecules, and nanomaterials [15].

The small molecule radiosensitizer category comprises a large group of nitroaromatic and nitroheterocyclic compounds that enhance the tumor response to standard radiation, mimicking oxygen and generating reactive oxygen species and radicals leading to DNA damage in hypoxic cells [16]. Nitroimidazoles and nitrofurans have been largely described as sensitizers [17-19], having a specific mechanism of action involving metabolic changes related to the nitro group accepting electrons from reducing enzymes (nitroreductases) thus generating intermediates that react with DNA to exert toxic and mutagenic effects [18, 20]. These compounds get into the intracellular space by diffusion and under hypoxic condition the process described above takes place, but under normoxic conditions the compound is re-oxidized back to the parent one and diffuses out of the cell [21].

Misonidazole (a 2-nitroimidazole derivate) and metronidazole (a 5-nitroimidazole) were two of the earliest developed sensitizers, with the former been more effective due to a higher electron affinity [22] as measured by one-electron reduction potential, which is a key factor in their efficacy. In preclinical studies, misonidazole showed better radiosensitizing effect than metronidazole in the majority of solid murine tumors [23-25]. Since their introduction in the 1970s, a great number of hypoxic cell radiosensitizers have been screened and have undergone clinical evaluation [12]. However, clinical trials have shown their limited therapeutic benefit, with misonidazole inducing undesirable side effects such as neurotoxicity [26]

Several 5-nitrofuran derivates such as nitrofurantoin, nifurtimox and nitrofurazone have been evaluated as radiosensitizers; however, as radiosensitizers of *in vivo* systems, their rapid metabolism and poor solubility in water were found as disadvantages [27]. More attention was paid to nitroimidazoles derivates, specifically to 2-nitromidazoles, giving rise to a second-generation nitroimidazole radiosensitizers, such as etanidazole or nimorazole [28], and more recently nitroimidazole alkylsulfonamides [29].

The radiopharmaceutical approach to measuring hypoxia is based on the use of these oxygen-mimetic molecules and their capacity to only act under hypoxic conditions [30]. On this point, positron emission tomography (PET) has been extensively used for studying hypoxia, and nitroimidazole moiety have been largely used in this regard [21, 31]. Fluoromisonidazole, [^{18}F]FMISO, a 2-nitroimidazole derivate, is the most extensively used radiopharmaceutical for molecular imaging of tumor hypoxia, being characterized by a lipophilic nature which ensures a feasible cell-membrane penetration [21]. Nonetheless, its high lipophilicity causes slow tracer accumulation, slow plasma clearance, and low tumor-to-background contrast [32], so new radiotracers with improved pharmacokinetic properties are necessary for clinical use.

Several nitroimidazole-based radiotracers (specifically 2-nitroimidazole-based) have been developed over the last 20 years such as [^{18}F]FAZA, [^{18}F]FETNIM, [^{18}F]HX4, [^{18}F]FRP-170 and [^{18}F]FETA [21], and even some of them have undergone preclinical trials ([^{18}F]FETNIM, [^{18}F]FETA, [^{18}F]FAZA, [^{18}F]EF3 and [^{18}F]EF5) [33]. The goal has been the same for all of this probes: overcome the drawbacks presented by [^{18}F]FMISO. Still, Fluoromisonidazole remains the most widely used radiotracer for imaging hypoxia.

The majority, if not all of these new radiotracers are just changing the lateral chain connected to the 2-nitroimidazole moiety in order to improve their pharmacokinetic properties, but increasing the efficacy and general use of these radiopharmaceuticals could be also achieved in theory by raising the redox potential of the nitroheterocycle. 2-nitromidazole derivates have a greater electron affinity than 4-nitro and 5-nitro imidazoles (2-nitro > 5-nitro >> 4-nitro) [34], and this is the reason why the 2-nitro-isomers are the building block for imaging radiotracers to target hypoxia [21]. Their efficiency as radiosensitizers may be qualitatively correlated with their redox potentials with sensitizers of higher redox potentials generally being found to be more efficient [17, 19, 35]. On this matter, it has been broadly discussed in the literature how 5-nitrofuran derivates have a greater reduction potential than 2-nitroimidazole ones [19, 36-38] , and the position of the nitro group on the furan ring plays a pivotal role on the electron affinity properties and activity of these compounds, with 5 nitrofuran derivates being the most active and electron affinitive among its isomers [39].

Up to date, no PET radiopharmaceutical for hypoxia have been widely adopted into routine clinical practice. Given this, in this work is proposed the first use of a nitrofuran-based radiotracer for detection of hypoxic regions in the tumor microenvironment, given the improved electron affinity properties of these nitroheterocycles compared to nitroimidazoles. This compound, (E)-1-(4-(fluoro-^{18}F)phenyl)-3-(5-nitrofuran-2-yl)prop-2-en-1-one ([^{18}F]FNFP), will be evaluated *in vivo* in tumor-bearing mice and compared to [^{18}F]FBNA, a novel 2-nitroimidazole-based radioligand for imaging hypoxia synthetized and characterized by our group [40].

2 OBJECTIVES

To synthesize and characterize a new radiopharmaceutical radiolabeled with [^{18}F], (E)-1-(4-(fluoro-[^{18}F])phenyl)-3-(5-nitrofuran-2-yl)prop-2-en-1-one ([^{18}F]FNFP), for the detection of areas of hypoxia in the tumor microenvironment through PET molecular imaging.

2.1 Specific objectives

i. To chemically characterize the synthetic intermediates and standard final products for the synthesis of [^{18}F]FBNA, [^{19}F]FBNA, [^{19}F]FNFP and [^{18}F]FNFP using Nuclear Magnetic Resonance (NMR), Mass Spectrometry (MS), melting point and Infrared Spectroscopy (IR).

ii. To determine the optimal conditions for radiolabeling [^{18}F]FNFP and [^{18}F]FBNA using a one-step/late-stage radiofluorination synthesis.

iii. To stablish a quality control protocol for [^{18}F]FNFP.

iv. To evaluate the stability of [^{18}F]FNFP in Phosphate-buffered saline (PBS) and serum.

v. To estimate the lipophilicity of [^{18}F]FNFP and compare it with those of [^{18}F]FBNA and [^{18}F]FMISO.

vi. To evaluate the *in vivo* uptake of [^{18}F]FNFP by PET imaging and through *ex-vivo* biodistribution studies in a gastric cancer tumor model and compare it with that of [^{18}F]FBNA

3 LITERATURE REVIEW

3.1 Cancer: general characteristics

Cancer is a term used to describe a group of more than 100 diseases in which abnormal or mutated cells have the ability to replicate intermittently [3]. Cellular changes lead to the involvement of adjacent tissues and can also reach other tissues, through the blood circulation and/or lymphatic system by the metastasis process [4].

Cancer originates from genetic or epigenetic changes resulting from external or internal factors. External factors are classified into physical, chemical, and biological factors such as exposure to ionizing radiation, toxic gases and viral infections, while internal factors refer to inherited mutations [41]. The most relevant mutations in cancer progression tend to affect three main types of genes: proto-oncogenes, tumor suppressor genes and DNA repair genes [42, 43].

The main common characteristics to most cancers, described in great detail by Douglas Hanahan and Robert A. Weinberg [4], one of the most cited and important publications in the history of Biology, correspond to: resistance to cell death, induction of angiogenesis, activation of invasion and metastasis, replicative immortality, evasion of the immune response , evasion of tumor suppressors, sign of continued proliferation and cellular energetic dysregulation.

The gold standard diagnostic method for solid neoplasms is biopsy, which is performed through histological analysis guided by immunohistochemistry with the assessment of morphological characteristics and invasiveness [44]. However, other less invasive techniques have demonstrated high relevance in aiding diagnosis, such as imaging tests [45] and measuring blood biomarkers [46, 47]. An example of these biomarkers are the long noncoding RNAs (lncRNAs), a kind of RNA molecule with a transcription length of more than 200 nucleotides and its own non-coding protein that play an important role in complex cellular processes such as apoptosis, growth, differentiation, and proliferation. Endogenous lncRNAs can be secreted by tumor cells into human biological fluids in the form of microvesicles, exosomes, or protein complexes, thereby forming circulating lncRNAs that are not degraded by RNA and are in a

stable state. Aberrant expression of lncRNAs has been observed in cancer patients, and in this context, endogenous lncRNAs can regulate the basic characteristics of cancer cells by controlling the expression of oncogenes associated with their suppressive and oncogenic functions. Therefore, circulating lncRNAs can be excellent biomarkers and are being studied in cancer diagnosis, prevention, prognosis, and therapy (Figure 1) [46-48].

Figure 1. Diagram summarizing possible clinical applications derived from the analysis of blood-based Long noncoding RNAs (lncRNAs), source Badowski, C., He, B. & Garmire, L.X. [46].

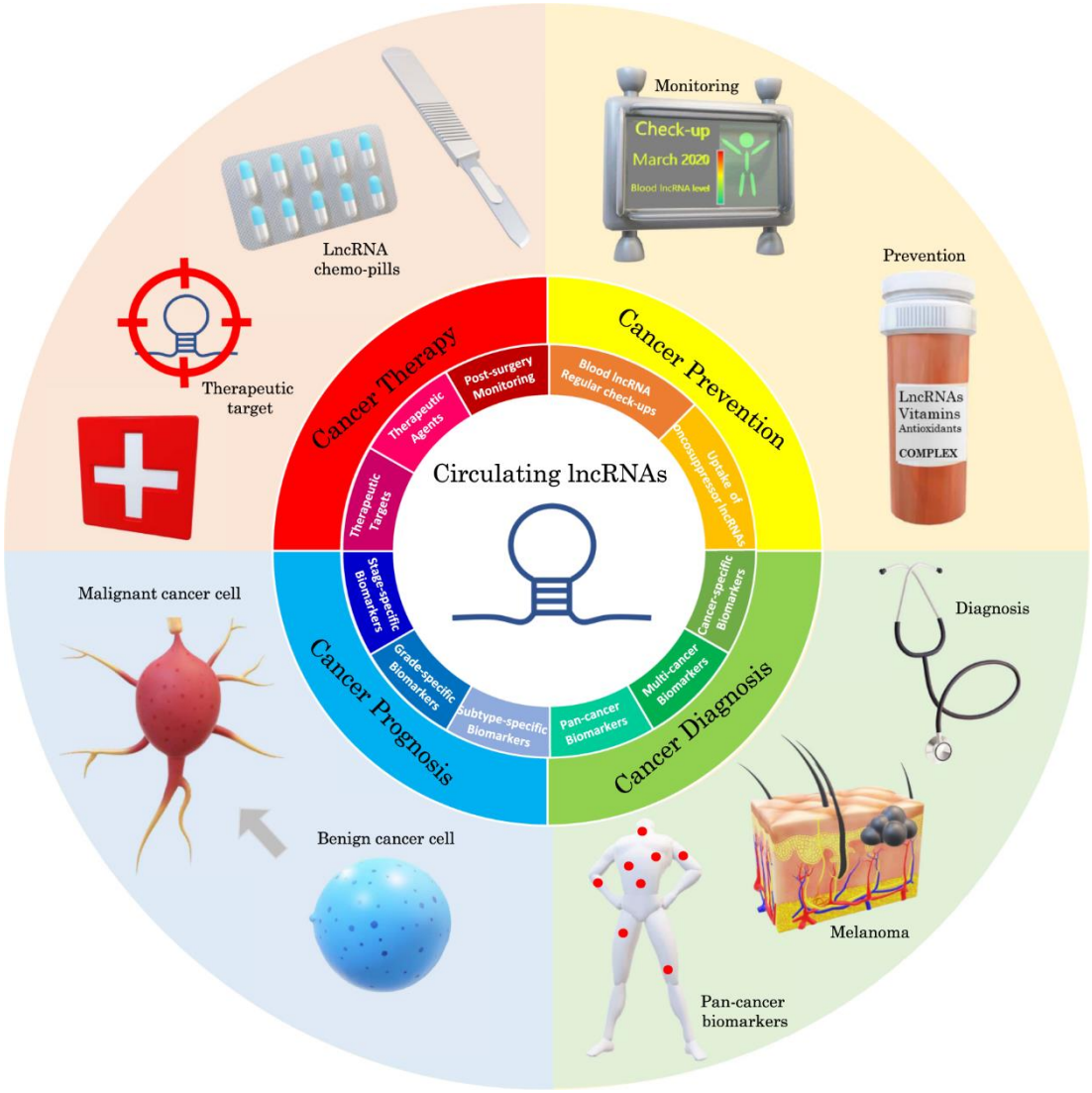

The use of these techniques makes it possible to monitor the progression of tumors and identify molecular markers to direct the most appropriate

treatment [49]. Despite ongoing efforts to develop new treatments and understanding the mechanisms underlying tumorigenesis, it remains difficult to treat cancers, particularly when diagnosed at late stages with a poor prognosis. The high mortality rate associated with cancer is partially due to the lack of early detection methods and/or inaccurate diagnostic tools [46].

Regarding biomedical imaging, one of the main pillars of comprehensive cancer care, these group of techniques and procedures offer many advantages including real time monitoring, accessibility without tissue destruction, minimal or no invasiveness and can function over wide ranges of time and size scales involved in biological and pathological processes [45]. This interdisciplinary field, requiring team effort among chemist, physicians, biologists, pharmacologists, computer scientists and clinicians of different specialties, is useful with time scales going from milliseconds for protein binding and chemical reactions to years for diseases like cancer [50]. Size scales go from molecular to cellular to organ to whole organism in different studies.

Functional-molecular imaging (FMI) information besides morphologic/anatomical changes can at the same time assess a multitude of biological cancer-related processes, improving diagnostic accuracy and the analysis of response to therapy [51]. Several imaging techniques are useful in this aspect, such as dynamic contrast-enhanced MRI (DCE-MRI), DCE-ultrasound (US), dynamic susceptibility contrast-enhanced MRI (DSC-MRI), perfusion CT (PCT), diffusion-weighted imaging (DWI), magnetic resonance spectroscopy (MRS) and spectroscopic imaging (MRSI), arterial spin-labeling (ASL), blood oxygenation level-dependent MR imaging (BOLD-MRI), elastography, positron emission tomography (PET), or single-photon emission computed tomography (SPECT) imaging (Figure 2) [51, 52].

In this way, obtaining molecular diagnostic methods that allow the identification of tumor characteristics, such as stage, tissue origin and present mutations, helps in designing better and more effective therapeutic strategies with a more appropriate pharmacological approach. Therefore, the development of tools for tumor differentiation/stratification becomes as important as obtaining new drugs for treatment.

Figure 2. Main imaging techniques in the evaluation of tumor biology and microenvinroment. Source García-Figueiras, R., Baleato-González, S., Padhani, A.R. et al. [51].

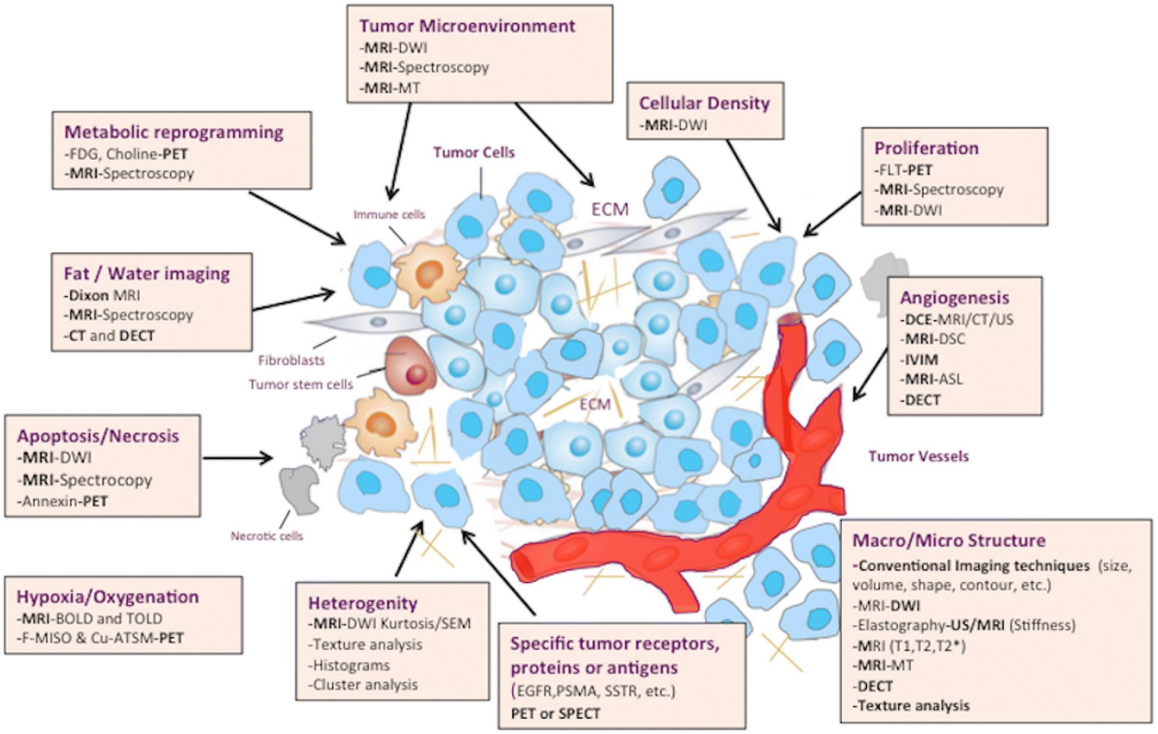

3.2 Hypoxia and cancer

Hypoxia or low oxygen tension, below the basal value of the organ or tissue, is a condition caused by a decrease in blood supply to a certain region of the organism [53]. It is widely accepted that, on average, the oxygen levels in hypoxic tumor tissues lie between 1%–2% below the respective levels in normal tissues [53]. Solid tumors are commonly affected by hypoxia, where uncontrolled cell proliferation often exceeds the ability to satisfy the oxygen demand from the preexisting blood vessels [54].

Traditionally, tumor hypoxia has been linked to potential therapeutic problems making solid tumors more resistant to ionizing radiation, chemotherapy, and other cancer treatments [5, 6, 8]. Moreover, tumors may develop an increased potential for local invasive growth, regional and distant tumor cell spreading [6], and in general hypoxia induces changes in gene expression and subsequent proteomic changes that have many important effects on various cellular and physiological functions, such as apoptosis

suppression [55], autophagy, promoting their survival [56], and anabolic changes in central metabolism [57, 58]. These changes are associated with the Warburg effect [58], one of the hallmarks of cancer [4] that refers to the preference of cancer cells to metabolize glucose anaerobically rather than aerobically, even under normoxic conditions, contributing to chemoresistance (Figure 3).

Figure 3. Relationship between Warburg effect-induced chemoresistance and tumor microenvironment. The hypoxia inducible factor (HIF-1) is a regulator of O_2 homeostasis within cells. As a transcription factor, regulates the expression of different genes that allow cells to survive as O_2 concentrations change. Then the tumor microenvironment undergoes a series of adjustments such as acidosis and stromal cell formation inducing chemoresistance in cancer. Taken from Liu, Chang et al. 2021 [59].

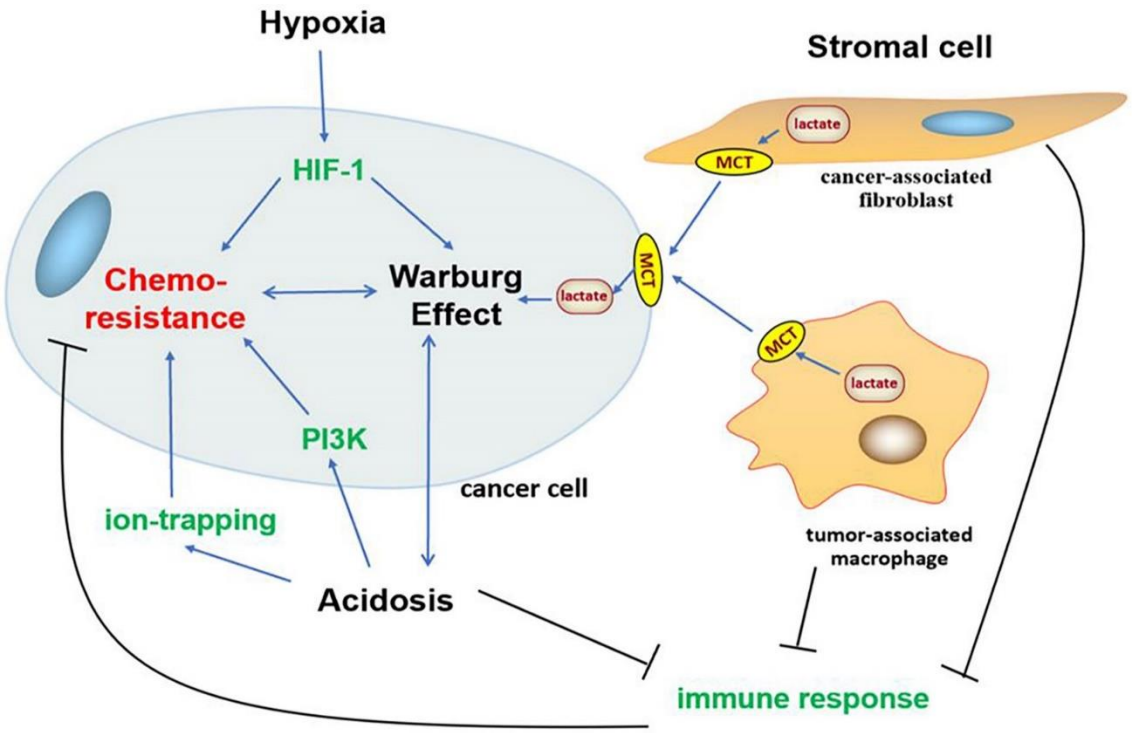

This chemoresistance induced by acidosis according to Figure 3 can be explained as follows: due to an increased anaerobic glycolysis as a result of upregulation of several major glycolytic enzymes, tumor cells produce abundant lactate, exported via monocarboxylate transporters (MCTs) that perform H^+-linked transport of L-lactate across the plasma membrane [60]. This process preserves intracellular acid–base balance and guarantees aerobic glycolysis

and lactate production to be continued; as a result, tumor cells maintain a special pH gradient, which is more acidic extracellularly and more alkaline intracellularly [59, 61, 62]. Most chemotherapeutic drugs are either weak bases or weak acids; only few of them are inner salts (or dipolar ions). Weakly basic drugs are neutralized and protonated under the tumor extracellular acidosis, making it difficult for them to pass through the cytomembrane and exert their function. Even if they get to pass through the cytomembrane, they will be isolated into acidic vesicles of lysosomes and lose their efficacy. Despite weakly acidic drugs increase their distribution in the interstitial fluid, they will become inactive before reaching the target due to intracellular alkalinity, a phenomenon called the “ion trapping mechanism” [63, 64].

As a result of the above-mentioned mechanisms and tumor cells features under hypoxic conditions, hypoxia is a determinant of cancer progression and therapeutic response that affects the curability of solid tumors, regardless of treatment modality. Especially for head and neck cancer patients, tumor hypoxia is linked to poor patient outcomes [65].

3.3 Cellular response mechanisms to hypoxia

Hypoxia-inducible factors (HIFs) are major molecules that respond to hypoxia and regulate multiple processes such as metabolism, proliferation, and angiogenesis. All members are composed of two different subunits, including the α-subunit (HIF-1α, HIF-2α, or HIF-3α) and β-subunit (HIF-1β) [66]. HIF-1α is constantly encountered cross all tissues, while HIF-2α and HIF-3α are expressed in specific ones [66]. In general, under hypoxic conditions, HIF-α combines with HIF-1β subunit to form a dimer, binds to hypoxia response elements (HREs), and causes expression of target genes [67, 68].

When oxygen is available, HIF-1α and HIF-2α undergo constant proteasomal degradation after hydroxylation by prolyl hydroxylases (PHDs), which require oxygen as a cofactor, and binding to the E3-ubiquitin ligase von Hippel-Lindau (VHL) complex [69]. Factor inhibiting (FIH-1) also inhibits HIF-α by binding to HIF-α and impeding the combination of HIF-α to the transcriptional coactivators CBP and p300 interfering with its transactivation (Figure 4) [70, 71].

Figure 4. HIF-1 pathway responses under hypoxic and normoxic conditions, taken from Bao, X., Zhang, J., Huang, G. et al. [72].

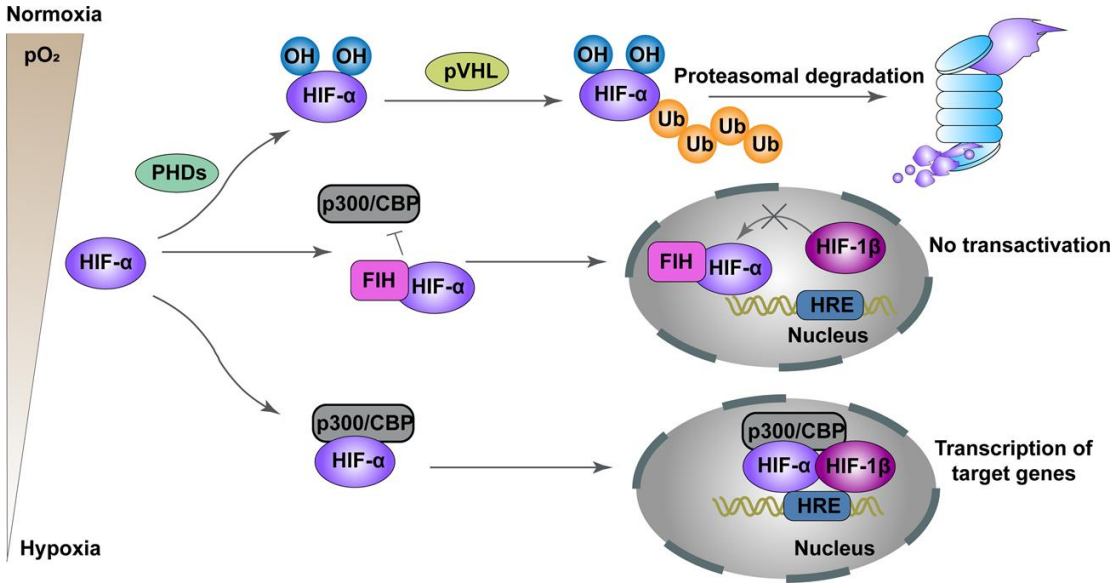

Under hypoxic conditions, PHDs are inhibited, and HIF-α hydroxylation is reduced resulting in accumulation and dimerization with HIF-1β, which leads to the accumulation of HIF-α. Afterwards, HIF-α dimerizes with HIF-1β to comprise a transcriptional activation complex, which binds to HREs and DNA, recruits coactivator proteins, and activates the transcription of more than 30 genes, which encode proteins involved in cell survival, angiogenesis, metabolic reprogramming, immortalization, resistance to radiation and chemotherapy, invasion and metastasis (Figure 4) [73]. Although changes in the HIF-α pathway have also been reported independently of hypoxia, this pathway is considered one of the most important in tumor cell adaptation to hypoxia [69].

The HIF-1 pathway has been explored for the development of compounds for the treatment of cancer through different mechanisms: a) PT2385 (Figure 5), an orally active small-molecule antagonist of HIF2α, was found to be effective in preclinical models of renal cell carcinoma [74]; b) the Geldanamycin analogues 17-AAG (Tanespimycin) and 17-DMAG (Alvespimycin) (Figure 5) are Heat Shock Protein 90 (HSP90) inhibitors that underwent clinical trials [75, 76]. In this case, O_2-dependent degradation of the HIF1α subunit is mediated by PHDs, the von Hippel-Lindau (VHL)/Elongin-C/Elongin-B E3 ubiquitin ligase complex, and the proteasome. Inhibition of HSP90 leads to O_2/PHD/VHL-

independent degradation of HIF1α (Figure 6) [77]. 17-AAG was found to be a potential therapeutic agent for gallbladder cancer [75] and for patients with advanced cancer [78]; on the other hand, 17-DMAG was effective and well-tolerated administered twice weekly in patients with advanced malignancies [79], and in another phase I clinical trial with patients with advanced solid tumors, clinical activity included complete response (castration refractory prostate cancer, 124 weeks), partial response (melanoma, 159 weeks), and stable disease (chondrosarcoma, and renal cancer for 28, 59, and 76 weeks, respectively) [80]; c) 2-methoxyestradiol (2ME2, Figure 5) is an antitumor and antiangiogenic agent that inhibits the synthesis of HIF-1α; Zhe, Nana et al. [81] found out that HIF-1α suppression by 2ME2 significantly induced apoptosis of acute myeloid leukemia (AML) cells, and concluded that 2ME2 may represent a powerful therapeutic approach for patients with AML.

Severe hypoxia leads to increased levels of unfolded proteins in the endoplasmic reticulum, activating the unfolded protein response (UPR) pathway, which is responsible for coordinating a cell's ability to respond to endoplasmic reticulum (ER) stress [82].

Figure 5. Compounds that act on the HIF-1 pathway.

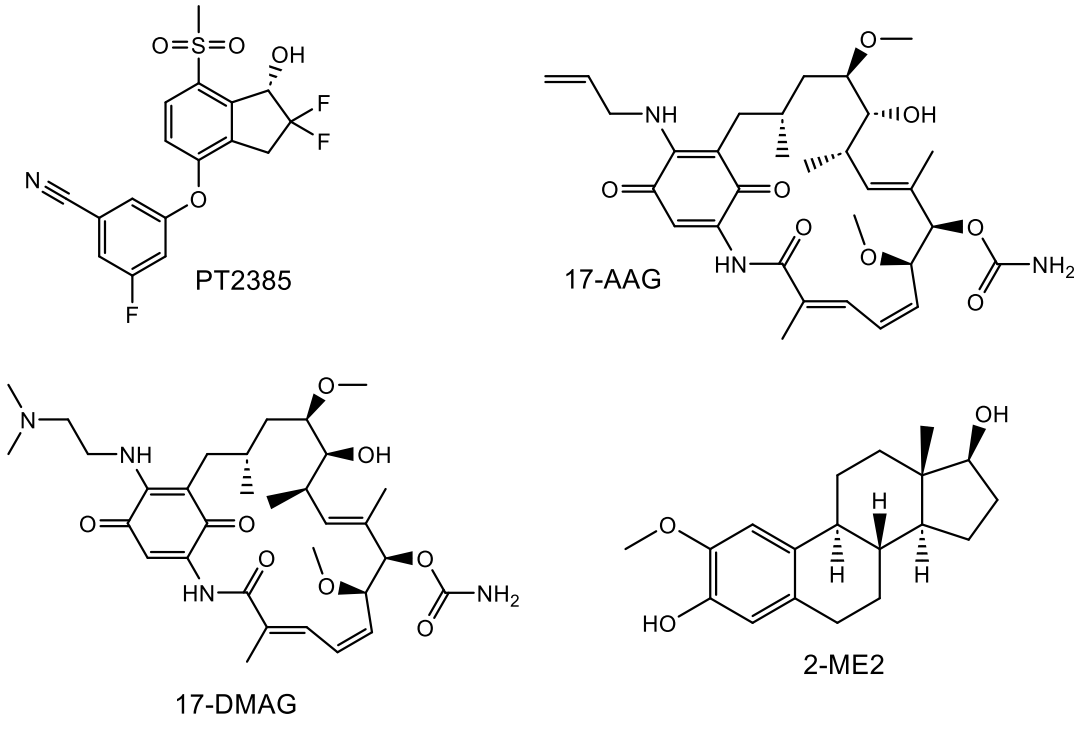

Source: Thesis author

Figure 6. HIFα subunit stabilization as a result of either hypoxia or VHL mutation leads to dimerize with HIF1β to form active HIF to transcriptional activate a panel of hypoxia responsive genes. Taken from Rathmell, W. K., & Chen, S. [83].

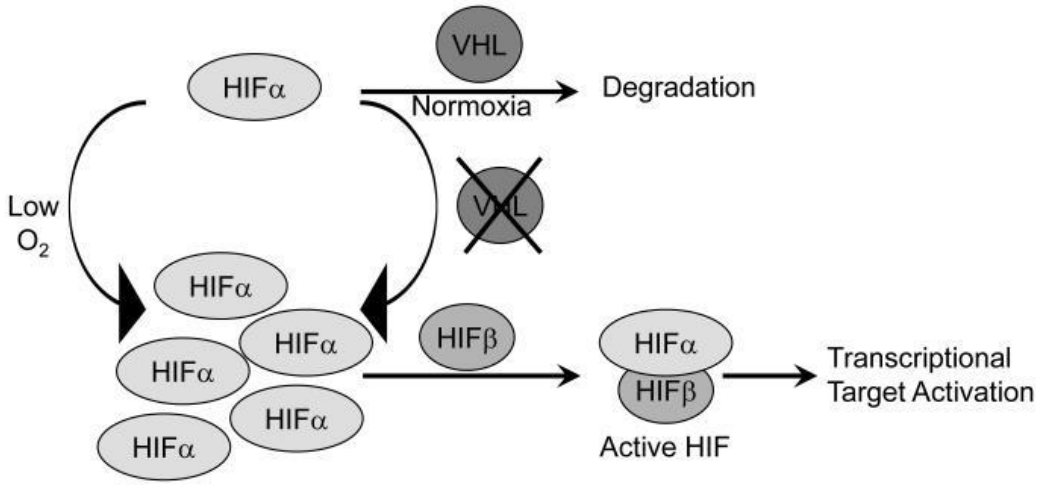

Oxygen acts as a preferential terminal electron acceptor in the protein folding process in the ER, thus the lack of oxygen is one of the causes of the increase in unfolded proteins. In general, the UPR pathway acts after ER stress activates the stress sensors ATF6, IRE1 and PERK, which result in the production of the transcription factors ATF6(N) (the N-terminal cytosolic domain of ATF6, responsible for the up-regulation of ER protein–folding chaperones and enzymes) [84], XBP1 and ATF4, respectively. These factors are responsible for the activation of genes to reestablish homeostasis by suppressing the synthesis or stimulating the degradation of proteins in the ER, and activating apoptosis and autophagy [85] (Figure 7).

Two main drug strategies are being pursued and studied to kill hypoxic cells selectively through UPR targets: 1) UPR inhibition by targeting PERK, ATF4 and IRE1. 2) Exacerbation of ER stress in order to overwhelm the UPR on the assumption that the UPR is near its capacity in hypoxic cells, approach supported by the evidence showed in a study with the ER stressors Thapsigargin and Bortezomib (Figure 8), with both eliciting hypoxia-selective cytotoxicity in vitro with tumor cells [86].

Figure 7. The three main O_2-sensing pathways that promote hypoxia tolerance by regulating transcription and mRNA translation. Taken from Wouters, B., Koritzinsky, M. [82].

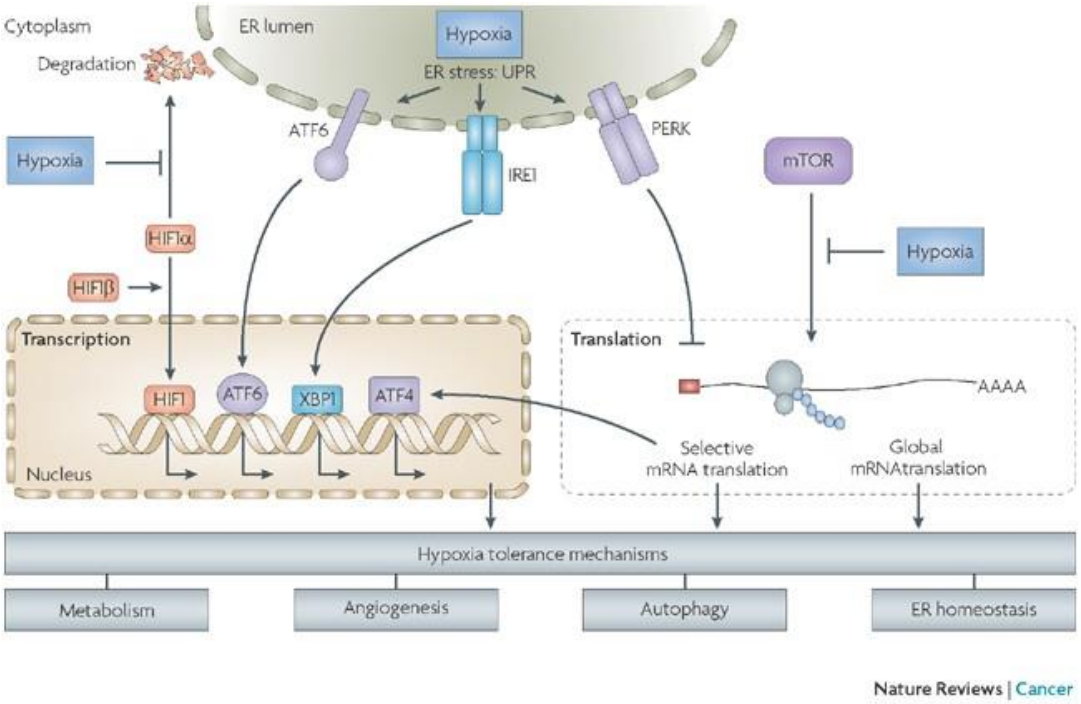

Figure 8. Compounds acting on UPR targets to kill hypoxic cells.

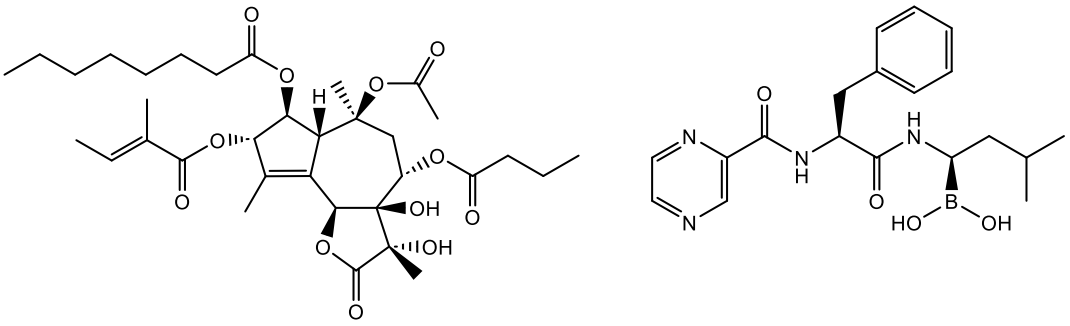

Thapsigargin Bortezomib

Source: Thesis author

Another pathway of increasing relevance corresponds to the mammalian target of rapamycin (mTOR) protein pathway (Figure 7). mTOR functions as a serine/threonine protein kinase that regulates cell growth by controlling mRNA translation, ribosome biogenesis, autophagy, and metabolism. In hypoxia, mTOR kinase complex 1 (mTORC1, one of two protein complexes along with mTORC2) activity is restricted by multiple pathways, resulting in the suppression of protein synthesis to an extent that depends on the severity and

duration of hypoxia. Restriction of mTORC1 leads to selective translation of a specific subset of mRNA, which includes the mRNA that translates HIF1α and vascular endothelial growth factor A (VEGFA) [82], with the latter augmenting cancer metastasis through several mechanisms, including (a) stimulation of tumor angiogenesis; (b) formation of leaky and disorganized primitive vessels in tumors; (c) promoting tumor inflammation; (d) Alteration of tumor hypoxia; (e) promoting interactions between cancer cells and vascular endothelial [87].

mTOR has emerged as a critical effector in cell-signaling pathways commonly deregulated in human cancers. This has led to the prediction that mTOR inhibitors may be useful in oncology, and derivatives of one such molecule, rapamycin (from which mTOR derives its name, Figure 9), are currently in clinical development [88]. In a distinct study carried out with WYE 125132 (Figure 9), another mTOR kinase inhibitor, this compound showed good results in cells under hypoxia by exerting selective antiproliferative effects and blocking the accumulation of HIF1α [89].

Figure 9. mTOR inhibitors.

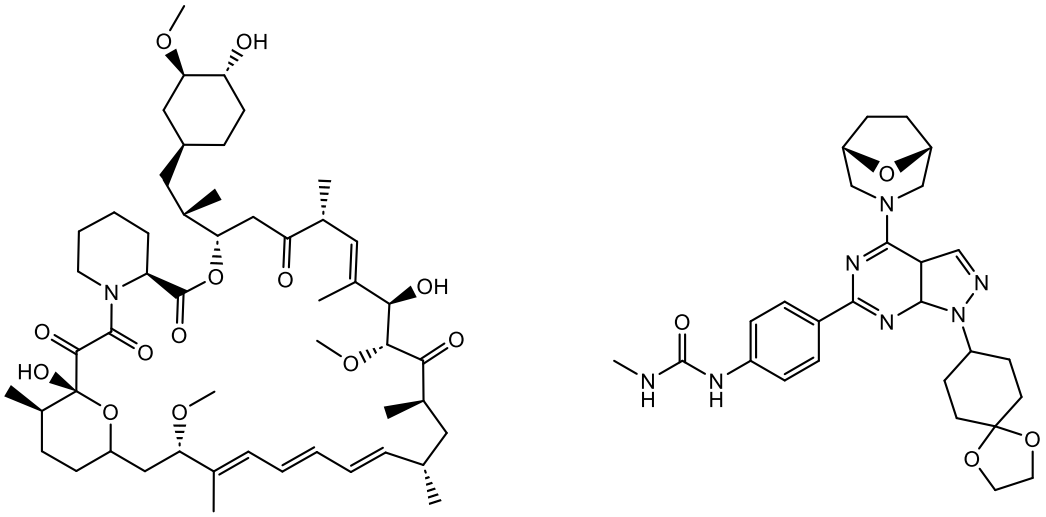

Rapamycin WYE 125132

Source: thesis author

3.4 Diagnosis of tumor hypoxia

Given all the problems and poor prognosis associated with tumor hypoxia, the goal for clinicians has been to identify moderately to severely hypoxic tumors for differential treatment strategies. Tumor hypoxia is linked to poor overall

survival especially in neck and head cancer patients [65], so prior therapy knowledge on the presence and extent of the hypoxia is needed [90].

Procedures for estimating tumor hypoxia are separated into three major groups: methods directly related to assessing the oxygen concentration; methods reporting on the physiologic processes involving oxygen molecules; and methods evaluating the expression of endogenous markers as a response to hypoxia (Figure 10) [65]. Table 1 summarizes some of the available techniques to evaluate tissue hypoxia status.

Direct methods are based on the explicit interaction of oxygen with a selective sensor that provides oxygen concentration data in the vicinity of the probe. Physiological methods rely on processes that also directly involve oxygen molecules. Although these methods do not directly measure oxygen concentrations in tissues, their response is proportional to it. Endogenous markers of hypoxia consist of proteins that are overexpressed in response to a decrease in oxygen supply [65, 91].

Figure 10. Hypoxia imaging methods and the type of information provided by each modality. BOLD MRI, blood oxygen level-dependent magnetic resonance imaging; DCE-MRI, dynamic contrast-enhanced magnetic resonance imaging; EPR, electron paramagnetic resonance; HIF-1α, hypoxia-inducible factor 1α; NIRS, near-infrared spectroscopy; OMRI, Overhauser-enhanced MRI; PALI, photoacoustic lifetime imaging; PAT, photoacoustic tomography; PET, positron emission tomography; PIMO, pimonidazole. Taken from Walsh, J. C. et al. [65].

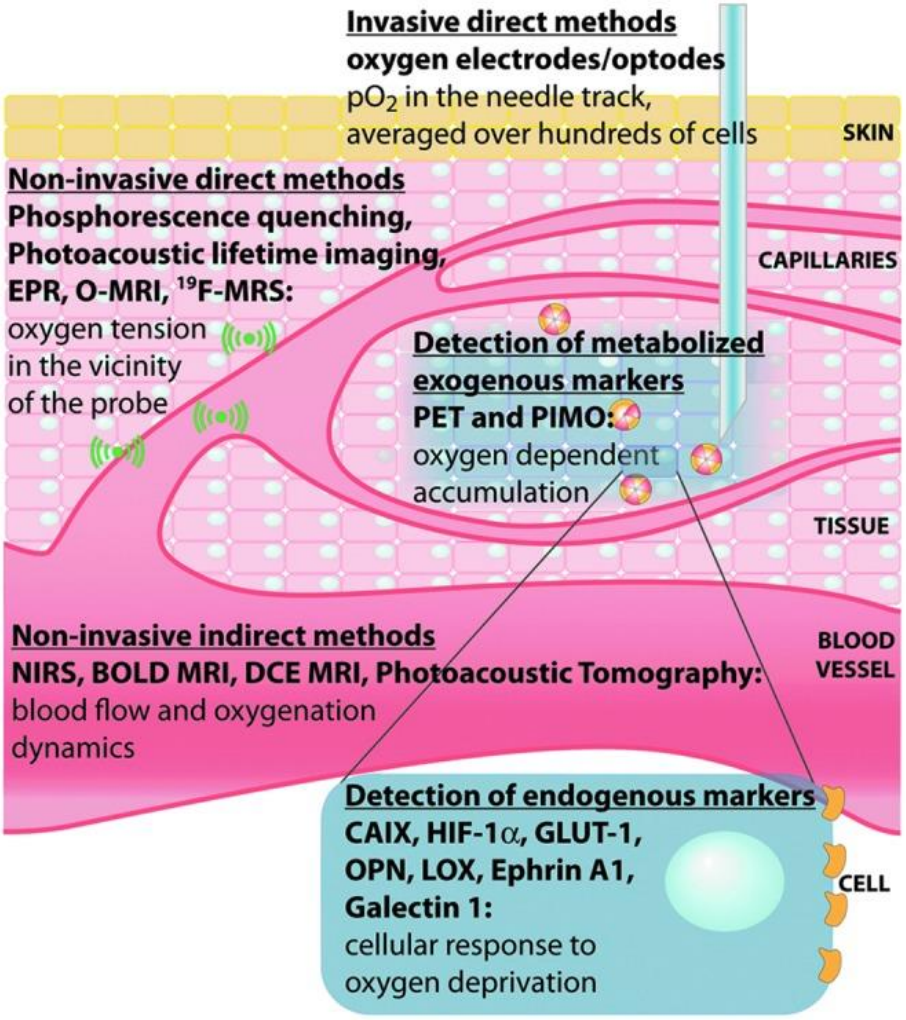

Table 1. Existing techniques for *in vivo* assessment of tumor oxygenation.

Adapted from Walsh, J. C. et al. [65].

Method	Direct	Physiologic	Endogenous	Approved clinical procedure
Polarographic oxygen electrode	x			+
Phosphorescence quenching	x			Europe only
EPR oximetry	x			-
^{19}F-MRI relaxometry	x			-
Overhauser-enhanced MRI	x			-
Immunohistochemical staining				
- CA-IX; HIF; Glut-1; OPN; protein panels			x	

Comet assay			x	-
Near-infrared spectroscopy (multiple modalities)		x		+
Photoacoustic tomography		x		
Photoacoustic lifetime imaging	x			-
Contrast-enhanced color duplex sonography		x		-
MRI/MRS techniques				
-DCE-MRI		x		Not for tumors
-BOLD		x		Not for tumors
-O_2-MRI	x			-
-Lactate MRS			x	-
-Pimonidazole, EF5		x		-
PET				
- ^{18}F tracers: FMISO, EF5, FAZA, HX4, etc.		x		-
- ^{64}Cu-ATSM		x		-
Miscellaneous perfusion measurements				
-PET with [^{15}O]H_2O		x		-
-Contrast-enhanced CT		x		+
-Ultrasound Doppler methods		x		+

BOLD, blood oxygen level dependent; CA-IX, carbonic anhydrase IX; CT, computed tomography; EPR, electron paramagnetic resonance; PET, positron emission tomography; •, method of hypoxia assessment; +, approved clinical procedure; −, not approved clinical procedure.

The polarographic electrode, also known as “Eppendorf electrode”, is an invasive, yet direct method for measuring tissue oxygen concentration that is based on the electrochemical reduction of oxygen molecules [92]. The oxygen measurements involve inserting an electrode into a tumor or metastatic lymph node and measuring oxygen from several points per needle track in sub-millimeter steps [93]. Even when this technique or procedure is often cited as the “gold standard” for hypoxia determination [9, 10, 65, 94, 95], its invasive

nature, the requirement of placing a needle directly into the tumor for measurements, the high cost of the equipment, tumor inaccessibility, high inter-observer variability, failure to distinguish necrosis from hypoxia, and the lack of spatial information make it a non-widely popularized technique [65, 93] impeding its routine use in clinical practice.

3.5 Hypoxia and radiation therapy: oxygen-mimetic radiosensitizers. Mechanism of action

Several strategies have been developed in recent years to improve cancer therapy including surgery, radiotherapy, chemotherapy, immunotherapy, targeted therapy, hormone therapy, stem cell transplant and precision medicine [96]. Since it is widely known that hypoxic tumors are associated with resistance to radiotherapy and chemotherapy resulting in a poorer clinical outcome for patients, it is crucial to develop more effective treatments.

Radiotherapy (RT) is considered as one of the most important and effective modalities to destroy cancer cells and tumor tissue via direct and indirect mechanisms by using high-energy photon radiation such as X-rays and gamma (γ)-rays [10, 97]. In the case of direct effect, ionizing radiation directly damages the DNA, which, if unrepaired, results in cell death or permanent growth arrest. In the case of indirect effect, reactive oxygen species (ROS) and free radicals are formed by the radiolysis of a large amount of water and oxygen, and then these intermediates react with the DNA of tumor cells leading to oxidative stress-induced damage of proteins, lipids, and mitochondria, and eventually death (Figure 11) [28].

Figure 11. Mechanisms of ionizing radiation damage to cells in RT. Taken from Gong, Liuyun et al. [28].

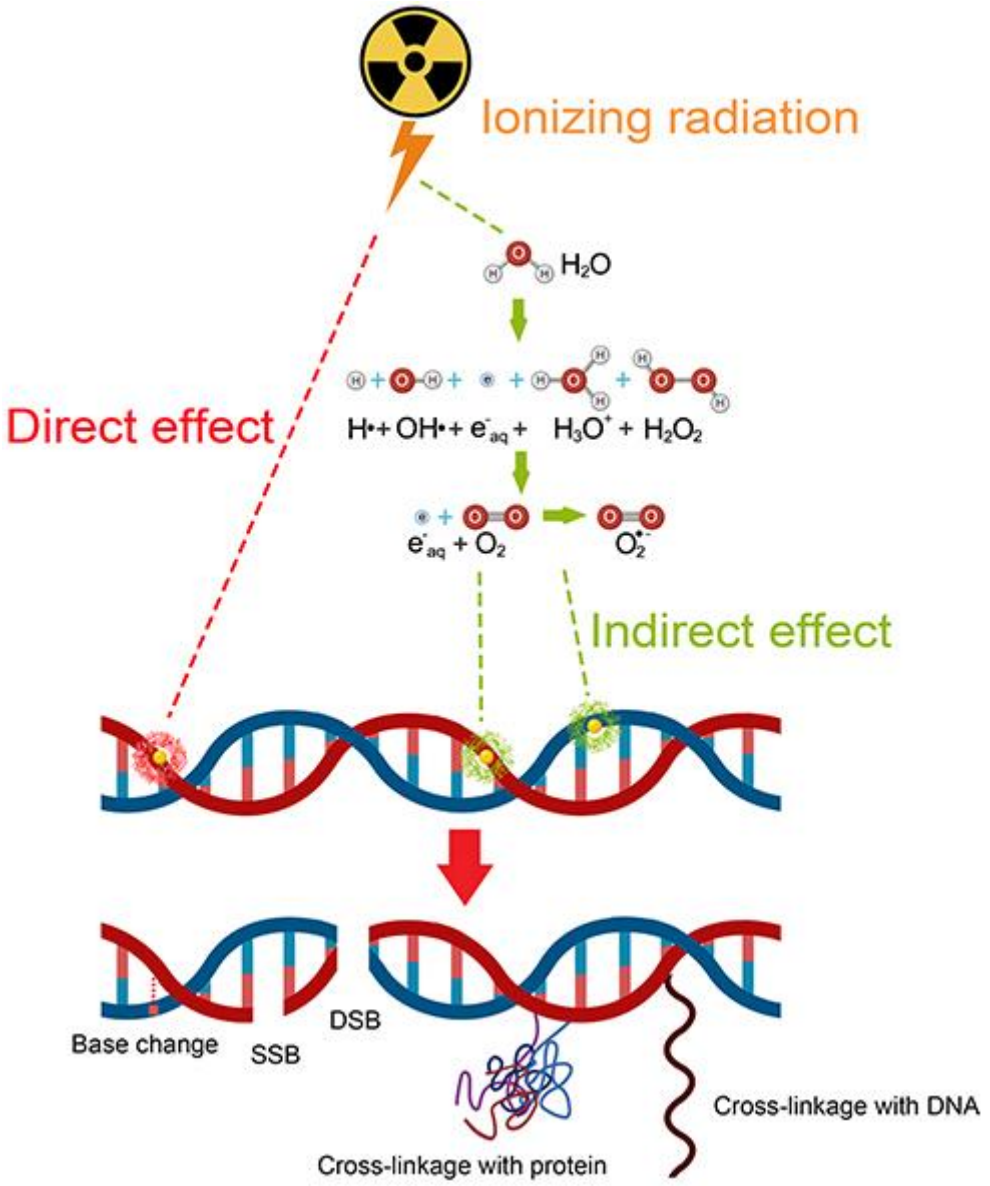

Innovative technologies can provide alternative strategies to improve RT efficiency. For example, image-guided radiation therapy (IGRT) is the use of imaging during radiation therapy to improve the precision and accuracy of treatment delivery. RT machines are equipped with imaging technology to allow physicians to image the tumor before and during treatment. By comparing these images to the reference images taken during simulation, the patient's position and/or the radiation beams may be adjusted to target the radiation dose more precisely to the tumor. To help align and target the radiation equipment, some IGRT procedures may use fiducial markers, ultrasound, MRI, X-ray images of bone structure, CT scan, 3D body surface mapping, electromagnetic transponders or colored ink tattoos on the skin [98]. Intensity-modulated

radiation therapy (IMRT) is an advanced mode of high-precision RT that uses computer-controlled linear accelerators to deliver precise radiation doses to a malignant tumor or specific areas within the tumor [99]. Although the above-mentioned innovative technologies greatly improve the therapeutic effect, there are still obstacles such as cancer stem cells and tumor heterogeneity making it difficult to use RT alone to cure tumors.

Hyperbaric oxygen treatment (HBOT) has been used for more than 50 years to improve or cure disorders involving hypoxia and ischemia, by enhancing the amount of dissolved oxygen in the plasma and thereby increasing O_2 delivery to the tissue [100]. One of the most important papers in radiotherapy was published in the 1950s when Gray et al. proved that the oxygen concentration in tissues influences the effect of radiotherapy [101], and the influence of hypoxic modification in relation to radiotherapy has been extensively studied since then [92]. Despite its benefits, HBOT is associated with several drawbacks such as lung damage, oxygen poisoning, seizures, tiredness and headaches [100].

In the early 1960s the seek for chemical agents that might act like oxygen to restore the sensitivity of hypoxic cells started. Unlike oxygen, they could not be metabolized by the cells through which they pass, and so high concentrations should be attained in hypoxic cells and radiosensitization achieved [35]. In short, what was needed was a “chemical sensitizer” that acted in the same way as oxygen and could reach the hypoxic tumor cells and sensitize them to radiation.

In 1971, 4-nitroacetophenone was recognized as a radiosensitizer [102, 103], and the identification of this compound was a breakthrough leading directly, and quickly, to chemical radiosensitizers selective towards hypoxic cells with potential clinical usefulness. Chapman and colleagues in 1972 [37] reported the first work about mammalian cell sensitization by nitrofurans such as nifurtimox, nitrofurantoin, nitrofurazone, and nifuroxime (Figure 12), proving that these nitroaromatic compounds could be also used as sensitizers. This was particularly significant since these compounds were already in clinical use (and have been for more than 50 years) as antibacterial agents and antibiotics, therefore considerable information on their toxicology, pharmacology and

pharmacokinetics was already available. Unfortunately, subsequent attempts to demonstrate hypoxic cell sensitization by these compounds in systems *in vivo* met with little success due to their rapid metabolism, toxicity, and low-water solubility. Two main pharmacophores are present in their structure, the nitro group (mostly present at the position 5) and a hydrazone moiety, whose carbon has zwitterionic (electrophilic and nucleophilic) properties, and aids in the overall chemical stability of the nitrofuran ring [104]. Moreover, this hydrazone moiety (R_1R_2-C=N-NR_3R_4) possesses anti-inflammatory, antibacterial, anticancer, antitubercular and antitrypanosomal activity [104, 105]. Under physiological conditions this hydrazone bond is rapidly hydrolyzed [106], giving side-chain metabolites that covalently binds to cellular proteins and persists *in vivo* for a certain time period, and is also responsible for toxic properties, such as carcinogenicity and mutagenicity [106, 107].

Figure 12. Some important nitrofuran drugs, their metabolites (highlighted in yellow), and pharmacophores present (colored).

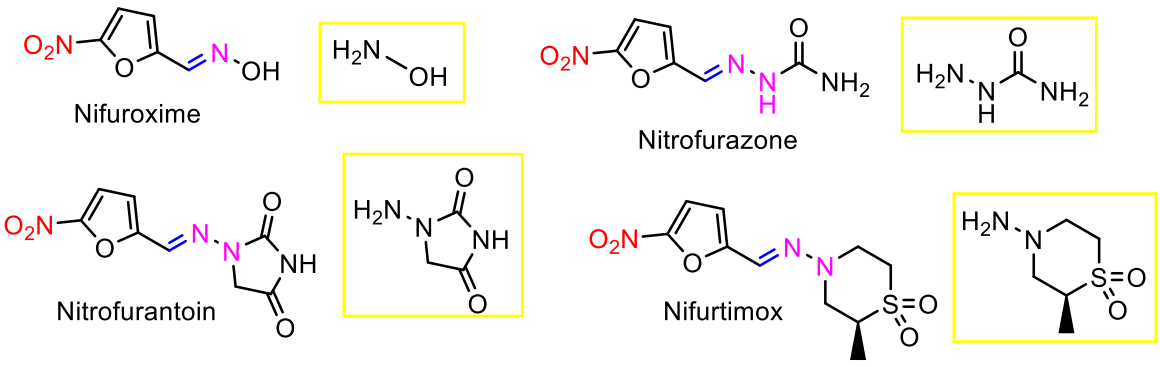

Source: Thesis author

In 1973, Foster and Willson reported the use of metronidazole (commercially known as “Flagyl”, Figure 13), a widely used antibiotic with antibacterial and antiprotozoal activity as radiosensitizer of anoxic cells [108]. This allowed the identification of a new family of nitroaromatic compounds as radiosensitizers, the nitroimidazoles, compounds that were already being used for example as antiprotozoal agents (benznidazole, Figure 13, launched by Roche in 1971 [109]).

Within a year, misonidazole (also known as Ro-07-0582 or MISO, Figure 13), another nitroimidazole derivate, was discovered as a much more effective

radiosensitizer of hypoxic bacteria and mammalian cells in vitro compared to metronidazole [110]. MISO underwent considerable clinical evaluation [111], but it became clear that its neurotoxic properties would seriously limit its application because the maximum clinical doses that could be achieved fell well short of those required for maximum sensitizing effectiveness [111-113].

Figure 13. Structure of the 2-nitroimidazole derivates, benznidazole and Misonidazole, and the 5-nitroimidazole derivate, metronidazole. (2NI-2-nitroimidazole, 4NI-4-nitroimidazole, 5NI-5-nitroimidazole).

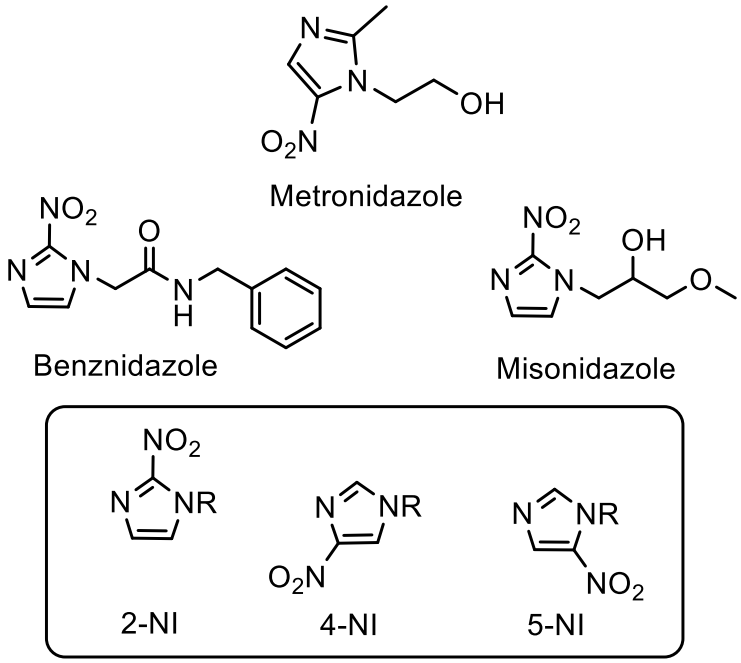

Source: Thesis author

The mechanism of action of these nitroaromatic compounds lies on their susceptibility to metabolic changes involving the nitro group accepting electrons from reducing enzymes (flavoprotein nitroreductases, NTR) [17]. In biological systems, nitro groups can undergo enzymatic reduction, which can proceed by either a one or two electron mechanism [114]. This reduction is catalyzed by NTR enzymes, of which there are two classes: type I (oxygen-insensitive) NTRs performing two-electron reductions, and type II (oxygen-sensitive) NTRs that perform one-electron reductions [115] (Figure 14).

Sequential two-electron reduction of nitro groups produces amines via nitroso and hydroxylamine intermediates. The nitroaromatics and amines are relatively stable. However, the nitroso and hydroxylamine intermediates can

react with biomolecules to exert toxic and mutagenic effects [116, 117]. Moreover, there is evidence to suggest that hydroxylamines are converted to reactive nitrenium ions, which can react with DNA [117].

One-electron reduction of a nitro group produces a nitro radical anion. This anion is not stable, and under aerobic conditions is re-oxidized back to a nitro group by molecular oxygen, which is in turn reduced to form a reactive superoxide anion. In the absence of oxygen, two nitro radical anions can undergo a disproportionation reaction to form one molecule of the parent nitroaromatic and a nitroso compound. It has been proposed that this process may produce nitroso compounds in biological systems [118].

Figure 14. One- and two-electron reduction of nitroaromatics. Adapted from Rice, Allison M et al. [114].

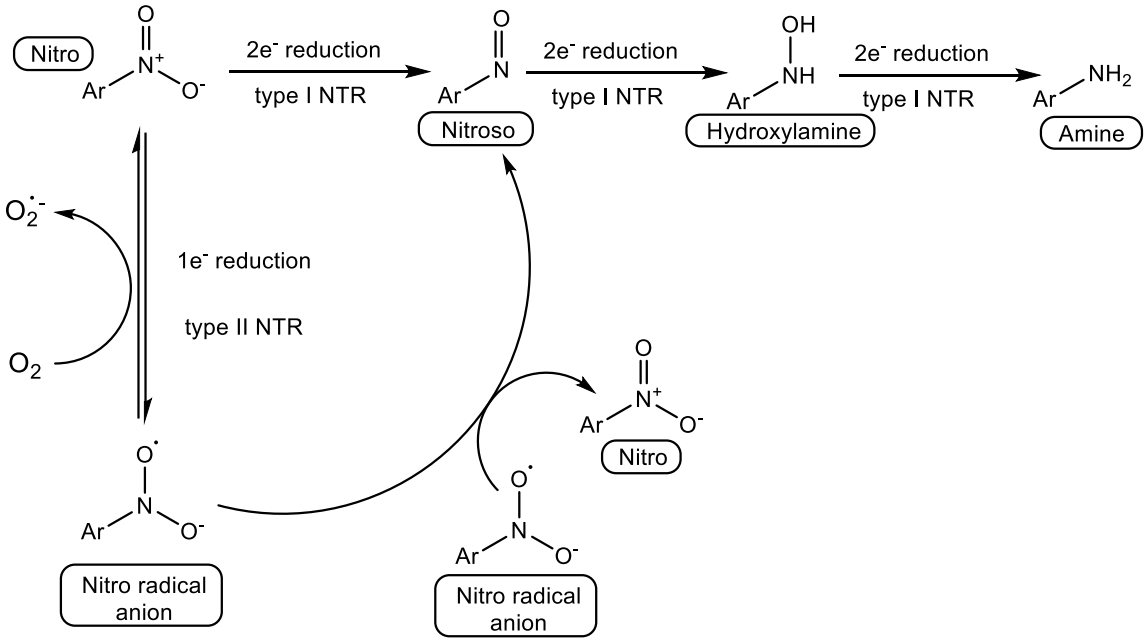

Two of the most important properties of a molecule acting as a radiosensitizer are the electron affinity, as measured by the one-electron reduction potential E_7^1 [119], and the lipophilicity. As discussed by Adams et. al., the extent of radiosensitization is dependent on the electron-affinity of the molecule [120]; the sidechain primarily governs its lipophilicity, indicating the relationship of that compound with its biological, pharmacokinetic, and metabolic properties [121]. More electron affinic compounds are reduced faster and easily under hypoxic conditions, thus being more effective sensitizers.

Electron affinity may be evaluated by using experimental and theoretical approaches. Half-wave reduction potentials by voltammetry and one-electron reduction potentials by pulse radiolysis techniques [35, 122] have been used to determine the electron affinity of some efficient radiosensitizers, and quantum mechanics methods have been employed regarding the theoretical techniques. Comparisons between one-electron reduction potentials and calculated electron affinities of nitroimidazoles, nitrofurans, nitrobenzenes and other nitroaromatic compounds have been made by several authors [38, 123, 124], with an important conclusion: for most important groups of compounds, E_7^1 decreases in the order nitropyridines > nitrofurans ≥ nitrothiophenes > nitrobenzenes > nitroimidazoles (Table 2).

Within the nitroimidazole family, meaning 2-nitroimidazoles, 4-nitroimidazoles and 5-nitroimidazoles, the electron affinic properties vary in the order 2-nitro > 5-nitro >> 4-nitro [17] (meaning 2-nitroimidazoles are more electron affinic than 5-nitroimidazoles, which are much more electron affinic 4-imidazoles). This is why MISO is much more effective radiosensitizer than metronidazole; in other words, a much lower dose of the former is necessary to induce a comparable sensitizing effect compared to metronidazole.

Table 2. Single-electron reduction midpoint potentials of nitroaromatic compounds determined by pulse radiolysis (E^1_7) or calculated according to the data of enzymatic single-electron reduction ($E^1_{7(calc.)}$). Adapted from Table A1 in Čėnas, Narimantas et. al. [38]. and references therein.

No.	Compound	E^1_7 (V)	$E^1_{7(calc.)}$ (V)
	Nitrobenzenes		
1	2,4,6-Trinitrotoluene (TNT)	−0.253	−0.279
2	1,4-Dinitrobenzene	−0.257	−0.240
3	1,2-Dinitrobenzene	−0.287	−0.311
4	3,5-Dinitrobenzamide	-	−0.311

5	4-Nitrobenzaldehyde	−0.325	−0.342
6	3,5-Dinitrobenzoic acid	−0.344	−0.336
7	1,3-Dinitrobenzene	−0.348	−0.332
8	2-Hydroxylamino-4,6-dinitrotoluene	-	−0.351
9	4-Nitroacetophenone	−0.355	−0.356
10	2-((2-Bromoethyl)(2,4-dinitro-6-((2-(phosphonooxy)ethyl)carbamoyl)phenyl)amino)ethyl methanesulfonate (PR-104A)	−0.366	
11	5-(Aziridin-1-yl)-2,4-dinitrobenzamide (CB-1954)	−0.385	−0.352
12	5,5-Dimethyl-3-(4-nitro-3-(trifluoromethyl)phenyl) imidazoline-2,4-dione (nilutamide)	-	−0.399
13	2-Methyl-*N*-(4-nitro-3-(trifluoromethyl)phenyl) propanamide (flutamide)	-	−0.408
14	2-Amino-4,6-dinitrotoluene	−0.417	−0.423
15	4-Nitrobenzoic acid	−0.425	−0.423
16	5-(Bis(2,2′-chloroethyl)amino)-2,4-dinitrobenzamide (SN-23682)	−0.425	−0.398
17	4-Hydroxylamino-2,6-dinitrotoluene	-	−0.429
18	4-Amino-2,6-dinitrotoluene	−0.449	−0.453
19	Nitrobenzene	−0.485	−0.489
20	*D*-(-)-threo-2-dichloroacetamido-1-(4-nitrophenyl)-1,3-propandiol (chloramphenicol)	−0.546	

Nitrofurans and nitrothiophenes			
21	2-(5′-Nitrofurylvinyl)-quinoline-4-carboxydiethylamino-1-methyl-but-1-ylamide (chinifur, quinifuryl)	−0.225	−0.221
22	5-Nitro-2-furaldoxime (nifuroxime)	−0.255	−0.279
23	*N*-(5-nitro-2-furfurylindene)-1-aminohydantoin (nitrofurantoin)	−0.265	−0.263
24	4-(5-Nitrofurfurylidenamino)-3-methyltiomorpholine-1,1-dioxide (nifurtimox)	−0.260	−0.285
25	2-Nitrothiophene-5-aldehyde	−0.260	
26	2-Nitrothiophene-5-aldoxime	−0.280	
27	2-Nitrothiophene-5-carboxymorpholide	−0.305	
28	2-Nitrofuran	−0.330	
29	2-Nitrothiophene	−0.390	
Nitroimidazoles			
30	1-Methyl-2-nitroimidazole-5-carboxamide	−0.321	
31	*N*-Benzyl-2-(2-nitro-1*H*-imidazol-1-yl)acetamide (benznidazole)	−0.380	
32	1-Methoxy-3-(2-nitroimidazol-1-yl)propan-2-ol (misonidazole)	−0.389	
33	1-(Methyl-2-nitro-1*H*-imidazole-5-yl)-methyl-*N,N*'-bis(2-bromoethyl)phosphorodiamidate (TH-302, evofosfamide)	−0.407	

34	2-Nitroimidazole	−0.418	
35	1-Methyl-2-(5-amino-1,3,4-thiadazole)-5-nitroimidazole (megazol)	−0.438	
36	1-Methyl-2-((4-(methylthio)phenoxy)methyl)-5-nitro-1H-imidazole (fexinidazole)		−0.458
37	2-Methyl-5-nitroimidazole-1-ethanol (metronidazole)	−0.486	
38	4-Nitroimidazole	≤−0.527	
	Miscellaneous		
39	4-Nitropyridine	−0.190	
40	4,6-Dinitrobenzofuroxane	-	−0.258
41	5-Nitro-4-(3′-dimethylaminopropylamino)-quinoline (nitraquine)	−0.286	
42	1-Nitro-9-(3′-dimethylaminopropylamino)-acridine (nitracrine)	−0.303	−0.285
43	1-*N*-alkyl-3-nitro-1,2,4-triazines	−0.310–−0.330	
44	2-((5-Nitrothiazol-2-yl)carbamoyl)phenyl acetate (nitazoxanide)		−0.380
45	5-Nitrothiazole	−0.400	
46	5-Amino-3-nitro-1,2,4-triazole (ANTA)	-	−0.466
47	3-Nitro-1,2,4-triazolone (NTO)	-	−0.472

48	1-(Chloromethyl)-3-(5-(2-(dimethylamino)-ethoxy)indol-2-carbonyl)-5-nitro-1,2-dihydro-3*H*-benzo[*e*]-indole (representative of nitroCBIs)	−0.512	
49	2-Nitro-6((4-(trifluoromethoxy)benzyl)oxy)-6,7-dihydro-5*H*-imidazo [2,1-*b*][1,3]oxazine (PA-824)	−0.534	

An important deliberation must be pointed out: if the electron affinity of the compound for the first, single-electron, reduction step (first electron reduction potential at neutral pH, E_7^1) is too great, approaching that of O_2 (-155 mV), then selectivity for hypoxia will be diminished because it will just behave as O_2 itself; if it is not sufficiently electron affinic (E_7^1 < -450 mV), then sensitivity will be lost. This step is critical, since it is reversible by O_2 and is therefore responsible for selective binding to only those tissues that are O_2 deficient. The E_7^1 's of most 2-nitroimidazoles are around -390 mV, an electron affinity considered to be optimal for both selectivity and sensitivity [22].

Unlike common nitrofurans tested as sensitizers, nitroimidazoles have a higher metabolic half-life (approx. 4 hours [110]) and improved pharmacokinetics, and more specifically, 2-nitroimidazoles, within the nitroimidazole isomers, have the best electron affinic properties. Even when nitrofurans (most of them active compounds against bacteria, parasites and fungi including the hydrazone moiety in their structure) have better electron affinic properties than nitroimidazoles as pointed out before, all the cons mentioned above make the formers a non-suitable option to be used as radiosensitizers.

3.6 Molecular imaging and radiopharmaceuticals to measuring hypoxia

Between 1970s-1980s an intense and concerted effort by several researchers and laboratories to produce and clinically evaluate oxygen-mimicking radiosensitizers to overcome the putative radio-resistance associated with solid tumor hypoxia was witnessed. A very important and crucial conclusion was the discovery of 2-nitroimidazole-based drugs and their superior ability to be reduced under hypoxic conditions compared to 4- or 5-nitroimidazole

derivates, or even the superior pharmacokinetic properties of nitroimidazole compounds compared to other nitroaromatic moieties such as antibiotic and antibacterial already-known drugs nitrofurans.

Hypoxic sensitizers bind selectively to the macromolecules of hypoxic mammalian cells as a result of metabolic mechanisms. One could argue that the same properties that allow radiosensitizers to accumulate under hypoxic conditions could be used to determine the location of hypoxic cells and measure tumor hypoxia, turning these sensitizers into “hypoxia markers”. This approach was first carried out with ^{14}C-radiolabelled misonidazole, and then with tritium(H-3)-labeled misonidazole (Figure 15) revealing by means of autoradiography heterogeneous distributions of radioactivity bound within rodent and human tumors [125-127]. In 1991, a clinical study characterizing H-3-misonidazole uptake and binding in 27 patients indicated that the amount of marker retained in tumor specimens relative to that in blood and other normal tissues might be amenable to non-invasive detection by nuclear medicine procedures [128, 129].

Figure 15. Structures of ^{14}C-MISO and ^{3}H-MISO.

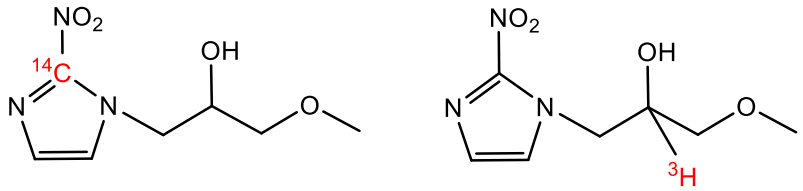

[^{14}C]Misonidazole [^{3}H]Misonidazole

Source: Thesis author

Molecular imaging is an attractive technology widely used in clinical practice that greatly enhances our understanding of the pathophysiology and treatment in a great number of diseases, as for example in cancer. It is a novel multidisciplinary technique that can be defined as real-time visualization, *in vivo* characterization, and qualification of biological processes at the molecular and cellular level involving the imaging modalities and the corresponding imaging agents [130]. Among all of the molecular imaging modalities, positron emission tomography (PET) and single photon emission computed tomography (SPECT) have occupied a particular position that visualize and measure the physiological

processes using high-affinity and high-specificity molecular radioactive tracers as imaging probes in a non-invasive approach [131].

PET enables the visualization and quantification of cellular and molecular processes in a non-invasive way by obtaining images, using radiopharmaceuticals/radiotracers containing positron-emitting radionuclides used in picomolar concentrations, such as ^{18}F, ^{64}Cu, ^{124}I, ^{68}Cu and ^{11}C. In general, these radionuclides, when decaying, emit positron particles (β+), antielectrons, which, after encountering a nearby electron, undergo an annihilation reaction emitting gamma radiation (Figure 16), which in turn is captured and translated into an image, demonstrating the localization of the radiotracer after *in vivo* biodistribution [130].

Figure 16. Positron-electron annihilation reaction. The emitted positron by the decaying radionuclide travels only a minimal distance before undergoing an annihilation reaction with the production of two 0.511 MeV photons that travel in opposite directions to one another. The predictability of $^{18}0°$ gamma photon release is the basis for PET detection. Taken from Chin, B.B., Workman, R.B., Coleman, R.E. [132].

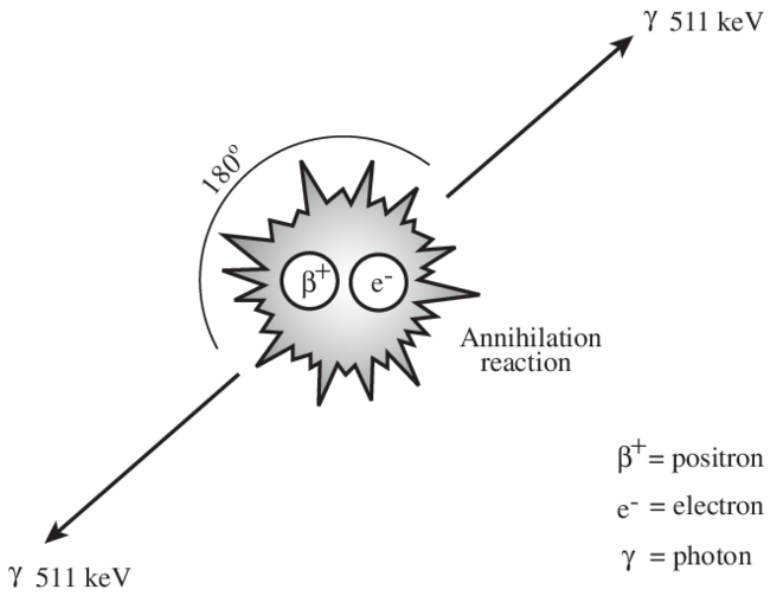

Due to the possibility of tracking the location of the radiolabeled molecule and evaluating its kinetics *in vivo*, PET has demonstrated wide application in clinical practice, research, and development of new drugs [133]. Nowadays, most of the PET scanners are actually PET/CT cameras. Modern PET/CT

scanners combine both PET and Computed Tomography (CT) scans almost simultaneously to provide a greater amount of clinical data to assist in the diagnosis process [134]. The CT portion of the scan produces a 3D image that shows a patient's anatomy in different angles, and the PET scan records how the radiotracer is been metabolized [135].

SPECT relies on the use of gamma-emitting radionuclides (^{99m}Tc, ^{123}I, and to a lesser extent ^{201}Tl) bounded to pharmaceuticals that just like PET provides both anatomical and functional information. SPECT-CT and planar scintigraphy account for almost 80% of all nuclear medicine scans performed worldwide [131]. While PET has the advantage of higher resolution and sensitivity, SPECT is more accessible and cheaper. With the adoption of PET/CT imaging in clinical practice, focus has shifted to developing novel PET radiopharmaceuticals. However, SPECT-CT still plays an important role in nuclear medicine imaging [131, 136].

The history of hypoxia markers, basically radiolabeled nitroimidazole-based-radiosensitizers derivatives, changed when in 1986 Jerabek et al. synthetized [^{18}F]fluoromisonidazole ([^{18}F]FMISO, 1H-1-(3-[^{18}F]fluoro-2-hydroxypropyl)-2-nitroimidazole) [137], a misonidazole derivate, as potential *in vivo* markers of hypoxic cells in tumors, and ischemic areas of the heart and brain (Figure 17). From this point forward, positron emission tomography with [^{18}F]FMISO became the most extensively used imaging modality to study hypoxia [21, 134], displaying several advantages over other techniques (magnetic resonance imaging, intrinsic and extrinsic oxygen electrodes etc.) such as information about the intracellular oxygen levels, good intrinsic resolution, three dimensional tumor representation and most importantly offering the highest specificity for detection of hypoxic tissue [21, 31, 134, 138]. [^{18}F]FMISO is currently the most extensively used radiopharmaceutical for molecular imaging of tumor hypoxia, being characterized by a lipophilic nature which ensures a feasible cell-membrane penetration [21]. Nonetheless, its high lipophilicity causes slow tracer accumulation, slow plasma clearance, and low tumor-to-background contrast [32], so new radiotracers with improved pharmacokinetic properties are necessary for clinical use.

[^{18}F]-fluoroazomycin-arabinofuranoside ([^{18}F]FAZA), ^{18}Ffluoroerythro-nitroimidazole ([^{18}F]FETNIM) and [^{18}F]-3-fluoro-2-(4-((2-nitro-1H-imidazol-1-yl)methyl)-1H-1,2,3-triazol-1-yl)propan-1-ol ([^{18}F]HX4) are three of the alternatives designed to solve the pharmacokinetic issues of [^{18}F]FMISO, with all three being 2-nitroimidazole derivates (Figure 17). [^{18}F]FAZA incorporated a sugar moiety turning it less lipophilic than [^{18}F]FMISO. With a lower octanol/water partition coefficient (log P=1.1) than [^{18}F]FMISO (log P=2.6) [139], [^{18}F]FAZA produced higher tumor to background ratios in biodistribution studies [139] and it was demonstrated that [^{18}F]FAZA-PET imaging could be used for a hypoxia-directed intensity-modulated radiotherapy approach in head and neck cancer. [140]. Despite this, [^{18}F]FMISO is still the reference tracer for defining hypoxic volumes, and there are reports showing its superior capability to [^{18}F]FAZA for specific studies [141].

Figure 17. Structure of different ^{18}F-radiolabeled hypoxic radiotracers.

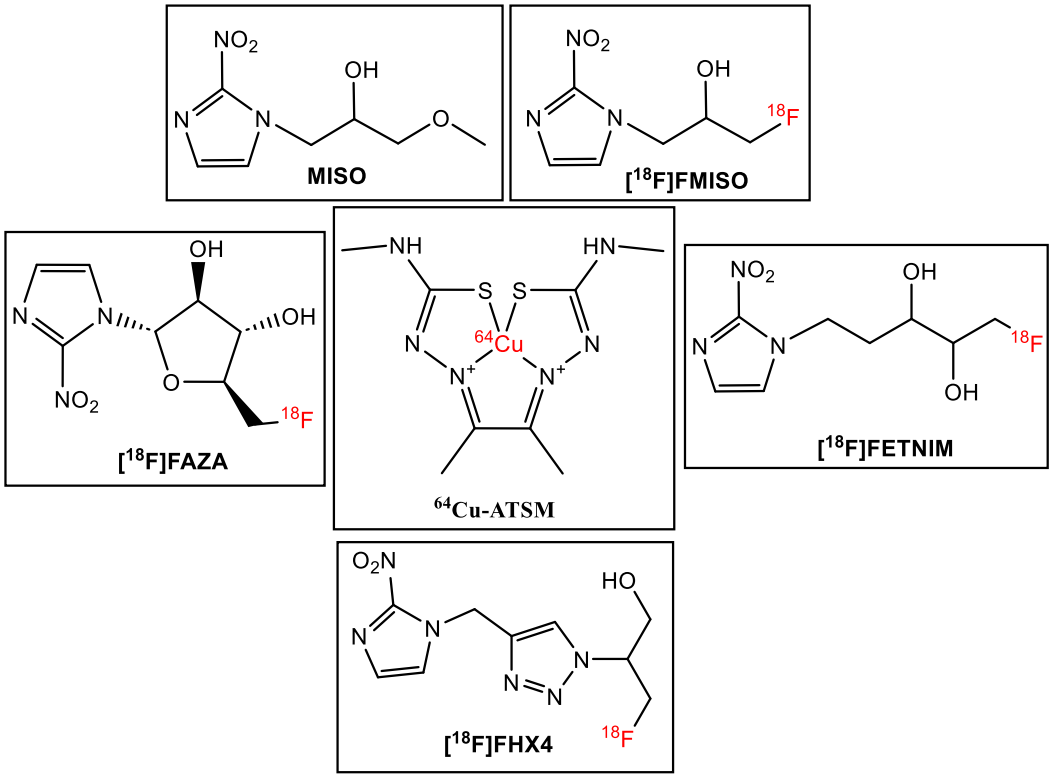

Source: Thesis author

Figure 18**.** Mechanism of action of radiotracers based on the nitroimidazole moiety under hypoxic conditions. Taken from Nguyen, Anh Thu, and Hee-Kwon Kim [142].

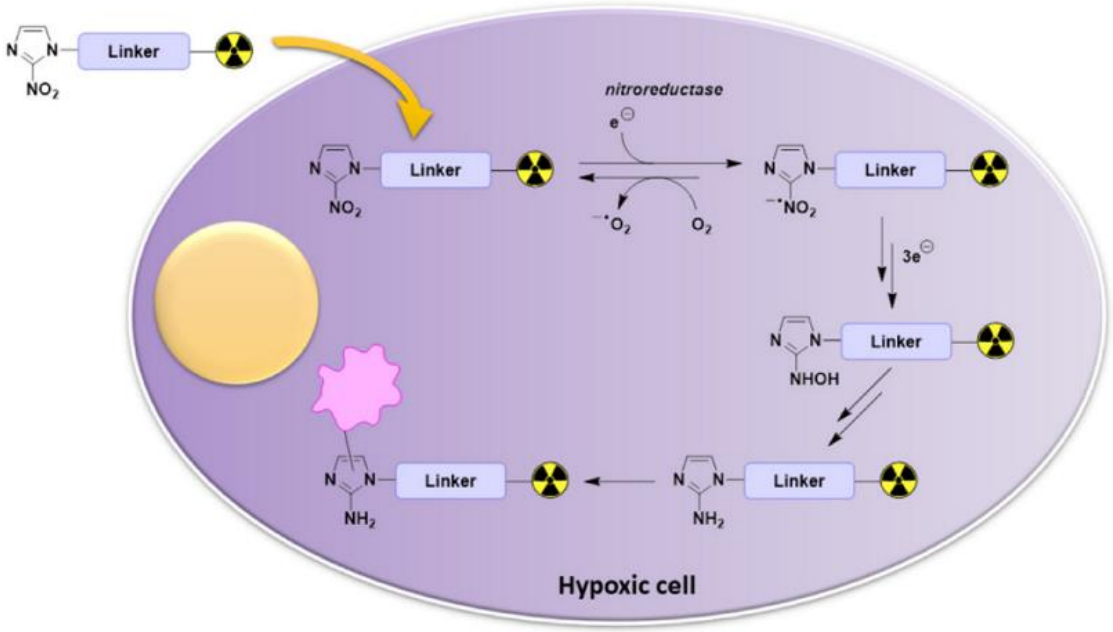

In a comparative study between [^{18}F]FETNIM and [^{18}F]FMISO in patients with lung cancer [143], the latter showed higher uptake in tumor/non-tumor ratio, and the authors concluded that [^{18}F]FMISO could be a better hypoxia tracer in lung cancer. In another study comparing the imaging characteristics and hypoxia selectivity of for PET radiotracers in a single murine xenograft tumor model condition [144], [^{18}F]HX4, [^{18}F]FMISO, [^{18}F]FAZA and [^{64}Cu]-diacetyl-bis(N4-methylsemicarbazone) (^{64}Cu-ATSM, an agent that could be used for both PET imaging and treatment of hypoxic tumors due to the release of therapeutic Auger electrons from copper-64, making it a "theranostic" agent [145]), the results indicated that both [^{18}F]FMISO and [^{18}F]HX4 had similar uptakes, with an improved renal clearance distribution for the latter. [^{18}F]FAZA demonstrated the lowest tumor uptake and lowest background, and finally ^{64}Cu-ATSM demonstrated the highest tumor uptake and image contrast of the hypoxia tracers studied. Compared to the more commonly used fluorine-based PET tracers, radiopharmaceuticals based on copper allow a rapid visualization

of hypoxia (in contrast to [^{18}F]FMISO), or better penetration of the blood-brain barrier and no urinary bladder uptake (in contrast to [^{18}F]FAZA) [30, 146], and longer half-lives (^{64}Cu $t_{1/2}$ = 12.7 hours vs ^{18}F $t_{½}$ =110 min) that contributes to better image quality and more convenient clinical practice [145].

Even when numerous authors have described *in vitro* and *in vivo* biochemical characteristics using PET imaging, precise mechanistic details of the pO_2-dependence of Cu-ATSM cellular uptake, localization and trapping within normoxic and hypoxic tissue remain uncertain. Fujibayashi et al [147] described one of the most recognized mechanisms, by which Cu-ATSM accumulates in hypoxic myocardium via a bioreductive retention mechanism involving nicotinamide adenine dinucleotide (NADH)-dependent enzymes of the electron transport chain, present in mitochondria [147]. These results suggested that upon intracellular reduction, Cu-ATSM becomes trapped irreversibly. Reduction of Cu-ATSM only occurs in hypoxic cells and involves electron transfer from hyper-reduced Complex I (ubiquinone oxidoreductase) using NADH as a two-electron donor. In normoxic cells, Complex I is incapable of reducing Cu-ATSM. In contrast, the non-hypoxia selective complex, Cu-PTSM which has a less negative one-electron reduction potential, may be reduced in all cells by Complex I in its normal state (i.e. not hyper-reduced), leading to irreversible intracellular trapping. In this mechanism, pO_2-dependence of the mitochondria-mediated one-electron reduction is the discriminating factor which controls the reversibility of cellular uptake.

Regarding SPECT radiotracers for imaging hypoxia, ^{99m}Tc and $^{123/125}$I have been the two most used radioisotopes. Preliminary clinical investigations with Iodinated azomycin arabinoside ([^{123}I]-IAZA, Figure 19), i.e. the iodinated counterpart of [^{18}F]FAZA, were reported in the 90s [148-150] in some hospitals where access to ^{18}F and PET systems were limited. The 13-hr half-life of ^{123}I compared to the 110 min of ^{18}F allows for delayed imaging to be performed.

The first clinical study assessing hypoxia with IAZA investigated the uptake of [^{123}I]IAZA in patients with advanced malignancies. Radiotracer avidity was observed in three of ten tumors, and it was concluded that the use of gamma emitter-labelled 2-nitroimidazoles as diagnostic radiopharmaceuticals is

feasible and safe and that metabolic binding of [^{123}I]IAZA is observed in some, but not all tumors [149]. In 22 patients, [^{123}I]IAZA uptake showed a significant inverse correlation with the perfusion marker ^{99m}technetium-hexamethyl-propylenamine oxime, [^{99m}Tc]HMPAO (Figure 19), and severe perfusion deficits were usually associated with an increased uptake of the hypoxic marker [148]. Reduced regional HMPAO uptake was unable to distinguish between necrotic or hypoxic tissue and the authors thought it was likely to underestimate the extent of viable tumor. The patterns of IAZA uptake suggested that this marker can discriminate viable hypoxic tumor, a parameter which could have significant prognostic potential [148].

After observing uptake of radioactivity in the brain after administration of [^{123}I]IAZA, a study was undertaken to investigate the proposed metabolites of IAZA in normal and tumor-bearing murine models. Neither of the proposed metabolites' biodistribution did support its involvement in brain radioactivity uptake in patients [151]. A study investigating the use of [^{123}I]IAZA in 51 human patients with newly diagnosed malignancies demonstrated hypoxia in small cell lung cancer and squamous cell carcinoma of head and neck but not in malignant gliomas. The study did, however, demonstrate the feasibility of [^{123}I]IAZA imaging in a clinical setting [150]. Stypinski et al. reported the clinical pharmacokinetics of IAZA, the radiopharmacokinetics of [^{123}I]IAZA, total radioactivity kinetics and the radiation dosimetry estimates for six healthy volunteers and concluded that all supported its clinical use for imaging tissue hypoxia [152, 153].

^{99m}Tc possesses a favorable half-life of 6 h and low photon energy of 140 keV. In terms of convenience, and compared to ^{18}F,^{99m}Tc can be obtained on-site as a pertechnetate ($^{99m}TcO_4^-$) by using commercial ^{99}Mo/^{99m}Tc generators which are smaller and more affordable than cyclotrons [154].

Figure 19. Early developed SPECT radiotracers for detection of hypoxia. ^{99m}Tc-HMPAO is a well-stablished radiopharmaceutical to assess regional brain perfusion.

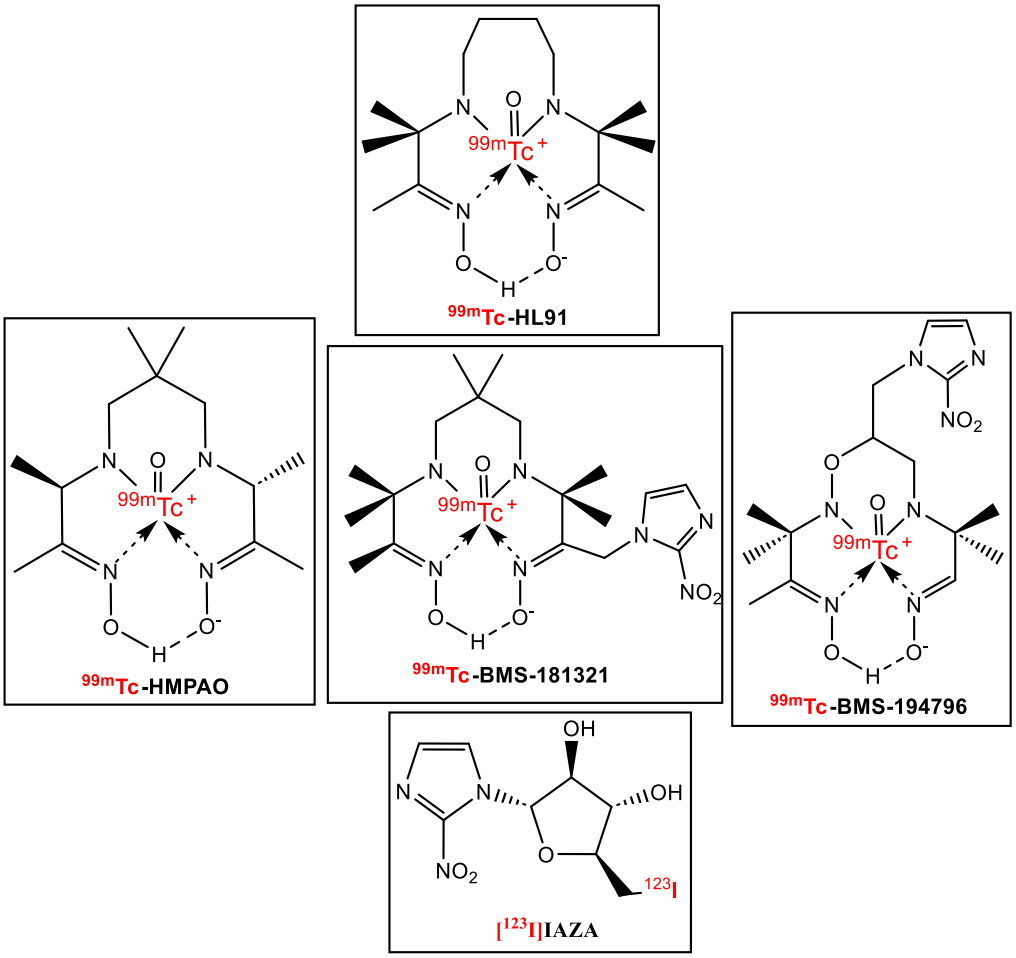

Source: Thesis author

BMS 181321 (Figure 19) was the first ^{99m}Tc-labelled 2-nitroimidazole to be widely studied for imaging [155], and several experimental studies have evaluated the use of BMS 181321 for the detection of ischemic and hypoxic

myocardium [156-159]. Ballinger et al. showed selective accumulation in hypoxic cells *in vitro* and *in vivo* but concluded that BMS ^{18}1321 was not optimal for tumor hypoxia imaging because of *in vitro* and *in vivo* instabilities and a high partition coefficient, resulting in slow clearance from the blood and high background levels in normal tissues [160].

BRU59-21, previously known as BMS 194796 (Figure 19), is a second-generation analogue of BMS 181321 which shows greater stability *in vitro* and more rapid clearance from the circulation *in vivo*, resulting in higher tumor to blood and tumor to muscle ratios. It showed selective localization in tumor cells incubated under hypoxic conditions and following intravenous injection in animal models representative of poorly perfused tumors [161]. In a study by Zhang et al., BRU59-21 and HL91 (Figure 19) were compared directly in the same *in vitro* systems. Both tracers proved suitable for hypoxia imaging [162]. *In vivo* evaluation of tumor hypoxia with ^{99m}Tc-BRU59-21 appeared to be safe and feasible, and uptake and retention of the marker seemed to be indicative of tumor hypoxia [163].

Throughout the years many other nitroimidazole-derivate compounds have been labeled with ^{99m}Tc for detection of hypoxic regions [142], even some of them containing more than one nitroimidazole moiety to improve pharmacokinetic properties.

As reviewed here, the literature shows that each radiotracer for detection of hypoxic regions in tumors has its strengths and weaknesses, and depending on the study and the information required a different one can be put forward. There are specific probes for SPECT and PET, most of them based on 2-nitroimidazole derivates, but there is no a single radiotracer considered as ideal for every study and specific situation.

3.7 Aromatic nucleophilic ^{18}F-fluorination: late-stage [^{18}F]fluorination

The very advantageous nuclear decay properties of fluorine-18 (97% β^+ decay, 109.7 min half-life, 635 keV positron energy), ensuring a high imaging resolution, made this radionuclide became the ‘workhorse’ of positron emission tomography (PET) and has remained so now for more than 30 years. Especially its favorable half-life allows, besides multi-step radiosynthesis, the supply of

PET centers without a cyclotron by industrial production and the logistics of ^{18}F-labelled radiopharmaceuticals [164]. This creates a concomitant desire for even better production of ^{18}F-labelled tracers and ligands. In fact, an impressive variety of new methodologies for radiofluorination has evolved over the last two decades, extending considerably the possibilities of no-carrier-added (n.c.a.) radiosynthesis with fluorine-18 [165].

Fluorine-18 is produced by proton irradiation of enriched [^{18}O]H_2O in a cyclotron via the ^{18}O(p,n)^{18}F nuclear reaction. The radionuclide is obtained as strongly hydrated [^{18}F]fuoride ions typically ranging from 50 to 300 GBq and with high molar activity (up to 1 TBq/µmol). Although fluoride ion is a strong nucleophile, in aqueous solution it forms hydrogen bonds with the surrounding water molecules and becomes unreactive for nucleophilic substitution [166]. To achieve nucleophilic fluorination, the ^{18}F-fluoride must be substantially dehydrated by elimination of the water in which is obtained, which is accomplished by trapping it on an anion-exchange resin, typically a Waters Sep-Pak QMA, allowing the removal and recovery of expensive target [^{18}O]H_2O. The radionuclide in then eluted typically with a 10-20% aqueous acetonitrile solution containing a phase transfer catalyst (PTC), such as the cryptand Kryptofix 2.2.2 (K_{222}) or tetrabutyl-/tetraethyl-ammonium cations, together with basic, non-nucleophilic anions (e.g. CO_3^{2-}or HCO_3^-) to enhance the solubility and nucleophilicity of the fluoride ion in organic solvents. An azeotropic drying process is followed to remove traces of water generally using anhydrous acetonitrile in 3 steps at 90-100 ºC in the presence of the previously mentioned weak base to avoid the loss of [^{18}F] as [^{18}F]hydrogen fluoride. In order to ensure its high nucleophilic reactivity under no-carrier-added conditions, all these steps are necessary to obtain the so-called ‘naked’ fluoride. Subsequent displacement reactions are conducted in anhydrous polar aprotic organic solvents, such as acetonitrile (MeCN), dimethylformamide (DMF) and dimethylacetamide (DMA). At present, this method is well established for the majority of routine ^{18}F-radiotracer productions and is employed in most commercially available synthesis devices [165, 167].

Despite the fact that this conventional azeotropic drying step has been used and remained basically unchained in the past 40 years, several drawbacks

are associated with it: a) a large amount of base (e.g., 1-2 mg potassium carbonate) is generally required to elute [^{18}F]fluoride efficiently from the QMA cartridge, and this amount of base requires a correspondingly large amount of labeling precursor and can result in low yields for base-sensitive precursors/products, limiting the flexibility for altering reaction conditions; (b) the azeotropic drying also requires a complicated setup for an automated synthesis module, and thus is poorly suited for miniaturizing a radiolabeling reaction and adapting it for use in a synthesis module. Manual synthesis also has the disadvantage of manipulating vials, solutions, and reagents with decent to high amounts of radioactivity; (c) impurities can be introduced from the anion exchange resin and in the drying step, and they may be detrimental to radiolabeling reactions; (d) the drying step is time-consuming (15-20 min), resulting in radioactivity loss due to decay; (e) the dried [^{18}F]fluoride may not be storable and thus not ideal for dose-on-demand radiosynthesis. Perhaps most important, (f) if the azeotropic drying is not done properly, it often results in low reproducibility or even failure of radiolabeling reactions, and this poor reliability and reproducibility in the production of PET radiotracers will limit their clinical and research uses. These problems often contribute to making the efficient and convenient preparation of ^{18}F-labeled radiotracers challenging [168].

To address all the cons mentioned, a wide variety of methods to carry out S_N2 ^{18}F fluorinations under less basic conditions have been developed over the last decades [169-174]. The choice of PTC plays a decisive role in the radiofluorination efficiency [175], so some of these methods rely on using different PTCs, rather than the highly basic combination of K_{222}/K_2CO_3. However, none of them appear to be ideal, as they only utilize a fraction of the available radioactivity, need special and nonstandard precursors/equipment, or are difficult to implement [176-178]

The first pathway to introduce non-carried added (n.c.a.) [^{18}F]fluoride into arenes for routine synthesis of radiopharmaceuticals was the classical aromatic nucleophilic substitution (S_NAr) method, requiring sufficient activation of the phenyl ring, which can be achieved by the introduction of electron withdrawing groups (EWG), ($-NO_2$, $-CN$, $-CF_3$, or carbonyl groups of aldehydes, ketones and esters) in the -ortho or -para position to the leaving group (Figure 20) [165].

The most common and efficient leaving groups for n.c.a. S_NAr are trimethylammonium salt and nitro group [179]. Lower temperatures (100−110°C) are normally used for an aromatic fluorination on trimethylammonium group compared with a nitro group (120−180°C), therefore anhydrous acetonitrile is often used as solvent in a closed reactor system for trimethylammonium displacement. Because of the higher temperatures required for substitution of nitro group, anhydrous DMF or DMSO are used as solvent.

Figure 20. Radiofluorination using the nucleophilic aromatic substitution approach (above) with different EWG in -para position to the trimethylammonium triflate leaving group. Below, an example of the synthesis of 4-[^{18}F]fluorobenzylamine reported by Way and Wuest [180].

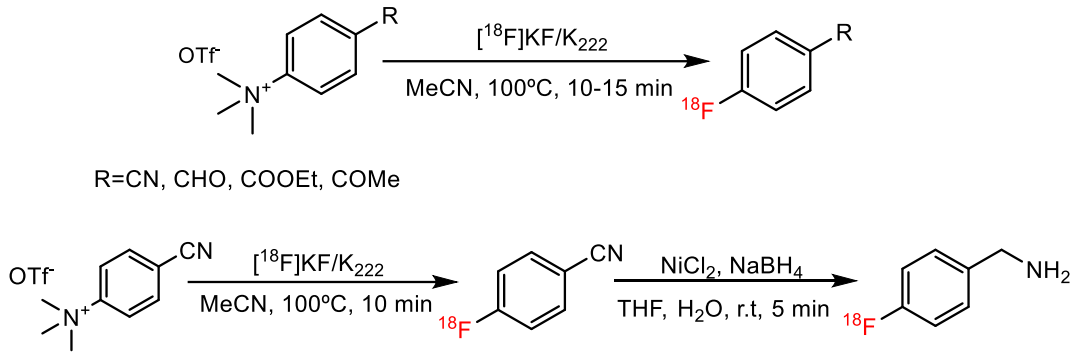

Source: Thesis author

The requirement that the aromatic ring must be electron deficient in order to achieve labeling severely limits the scope of aromatic nucleophilic substitution, which was an approach completely limited to electron deficient arenes [164, 167, 179]. A great deal of effort has been expended to find easier, more general, and more efficient methods to achieve aromatic substitution.

During the last decade, three main strategies were established for ^{18}F-fluorination of non-activated or even electron rich arenes, with the latter being the most challenging compounds for nucleophilic substitution with n.c.a. [^{18}F]fluoride: i) ^{18}F-displacement reaction, removal of an activating group and hydrolysis of protecting groups, and one- or two-step reactions, ii) employing ”onium” compounds as precursors and most recently iii) by transition metal-mediated radiofluorination. In most cases of the latter two methods, the radiofluorination step is again followed by hydrolysis of protecting groups.

Regarding the first method, ^{18}F-labelled building blocks like [^{18}F]fluorobenzaldehyde, 4-[^{18}F]fluorobenzonitrile or ethyl 4-(fluoro-^{18}F)benzoate [178, 181], have been prevalently the pathway of choice. Their disadvantage, however, is the difficulty of automation, since several reaction steps, often including separation and purification of intermediates, are necessary. Nevertheless, an originally five-step nucleophilic build-up synthesis of 6-[^{18}F]fluoro-L-DOPA succeeded for example, starting from [^{18}F]fluorobenzaldehyde derivatives [182] (Figure 21).

Figure 21. Automated radiosynthesis procedure for [^{18}F]F-DOPA using the chiral phase transfer catalyst cPTC as described by Shen, B et al. [182].

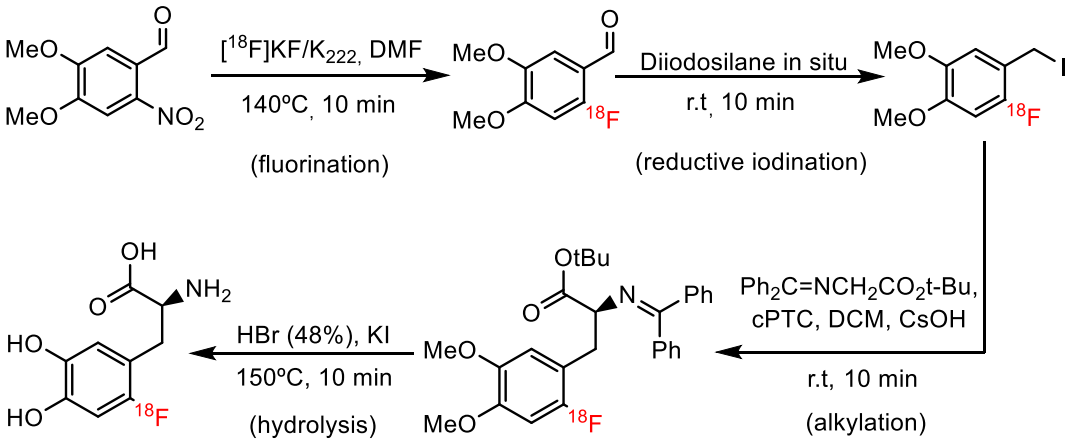

Source: Thesis author

The iodonium strategy (method ii), which was for the first time introduced into ^{18}F radiochemistry in 1995 [183-185], and the use of triarylsulfonium salts [186] were initially limited to the synthesis of small molecules, like 1-bromo-4-[^{18}F]fluorobenzene [187] and 1-[^{18}F]fluoro-4-iodobenzene [188, 189]. The latter served especially as building block in transition metal-mediated reactions for the synthesis of ^{18}F-radiotracers [190]. This type of reaction has been well established in commercially available synthesis devices [191]. For the last decade then, the challenges for ^{18}F-fluorination of complex molecules, using iodonium compounds, have been solved more and more, and a new review extensively discusses in detail their utility for small molecules, including mechanistic as well as application aspects [188].

Figure 22. Methods of nucleophilic ^{18}F-substitution of non-activated arenes via "onium" compounds (method ii). X^- (anion)

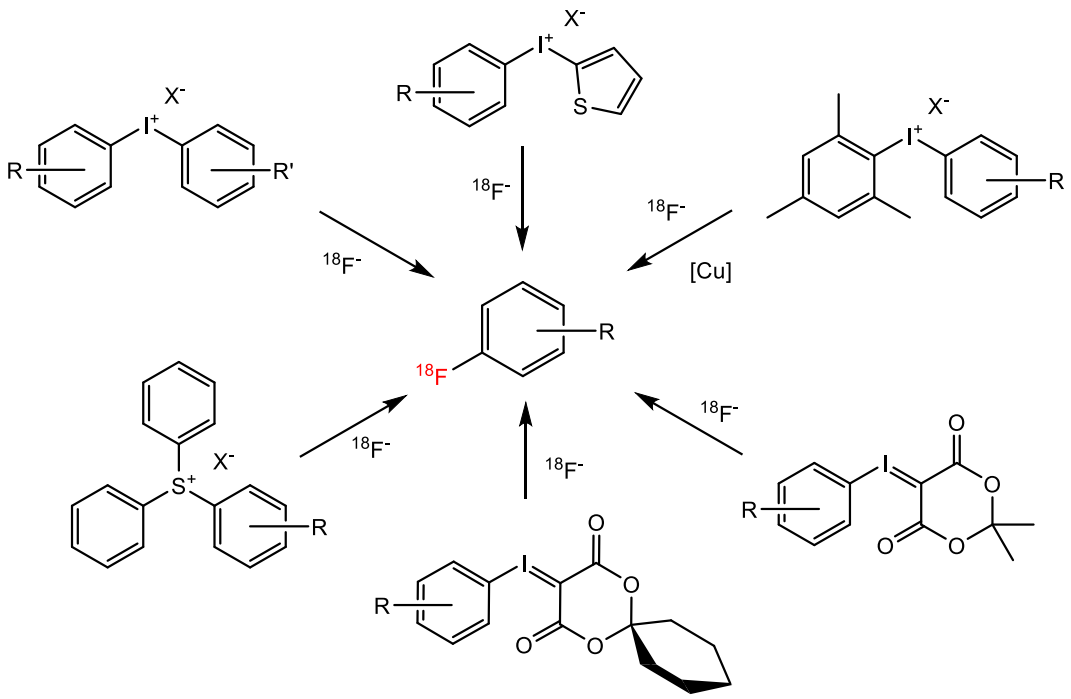

Source: Thesis author

The regioselectivity of this fluorination reaction is guided by the electronic and steric features of the two aryl rings [185, 189] (Figure 23, A). In the case of asymmetrical diaryliodonium salts, the nucleophilic substitution occurs on the more electron deficient aromatic component. In addition, the regioselectivity of the substitution is subject to an observed "ortho" effect, which directs the ^{18}F-fluoride substitution toward the aromatic ring which has substituent ortho to the iodonium moiety. Moreover, the RCYs increase when an additional ortho-substituent is introduced into the ring [185].

The degree of reactivity and the selectivity of radiofluorination of asymmetrical diaryliodonium salts was reported by Chun et al. [192], which had shown that the selectivity for an ortho substituted product depends on the ortho substituents in the following order: 2,6-di-Me > 2,4,6-tri-Me > Br > Me > Et ~ iPr≫ H > OMe.

Figure 23. ^{18}F-S$_n$Ar on diaryliodonium salts. (A) ^{18}F-Labeling on dihomoaryliodonium. (B) ^{18}F-Labeling of aryl(2-thienyl)iodonium salts. (C) ^{18}F-Labeling 3-cyano-5-((2-(fluoromethyl)thiazol-4-yl)ethynyl)phenyl)(4-methoxyphenyl) iodonium salt [193]. The figure was adapted from Jacobson, Orit et al. [194].

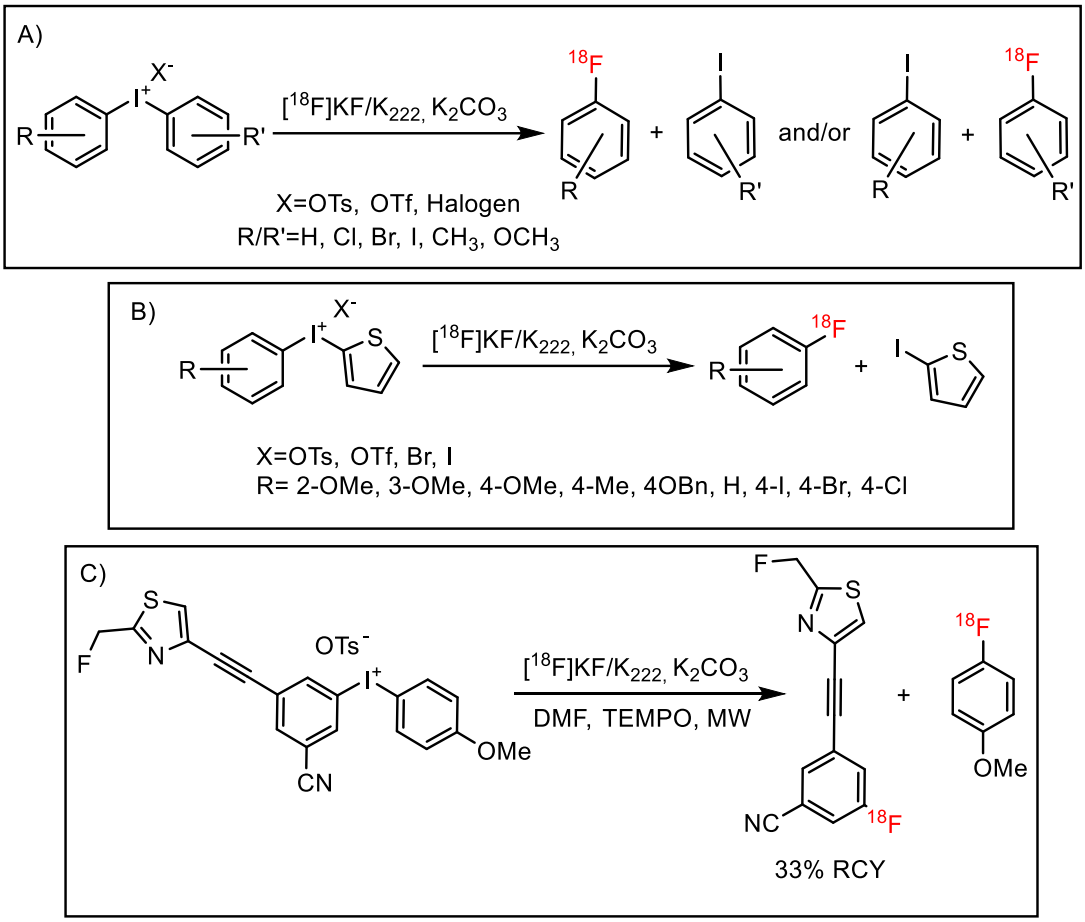

The challenge of applying this methodology in radiochemistry is the design, synthesis, and purification of the required precursor. The entire molecule must be constructed with iodine in the ultimate location of the radioactive fluorine, the molecule must either be substituted ortho to the desired site of fluorination or electron poor in relation to a thiophene or 4-methoxybenzene and this precursor structure must be compatible with the oxidative procedures for preparing the iodonium salt. Attempts to label more complicated small organic molecules with this method have resulted in much lower isolated radiochemical yield [193].

The novel transition metal-mediated ^{18}F-labelling strategies (method iii) have a major potential to revolutionize (if they have not already) ^{18}F-labelling of

even electron rich arenes. Operationally simple under relatively mild reaction conditions, they can be performed at the n.c.a. level, the required precursors are mostly stable at room temperature, and they can be applied to a wide range of compounds [194].

The first attempts were performed by palladium-mediated radiofluorination [195] of Pd(V) complexes as precursors [196], or by nickel-catalyzed ^{18}F-reactions [197, 198] (Figure 24). However, those first attempts did not fulfil the desired, afore mentioned properties.

Figure 24. Novel transition metal catalyzed radiofluorination methods for non-activated and electron-rich arenes (method iii).

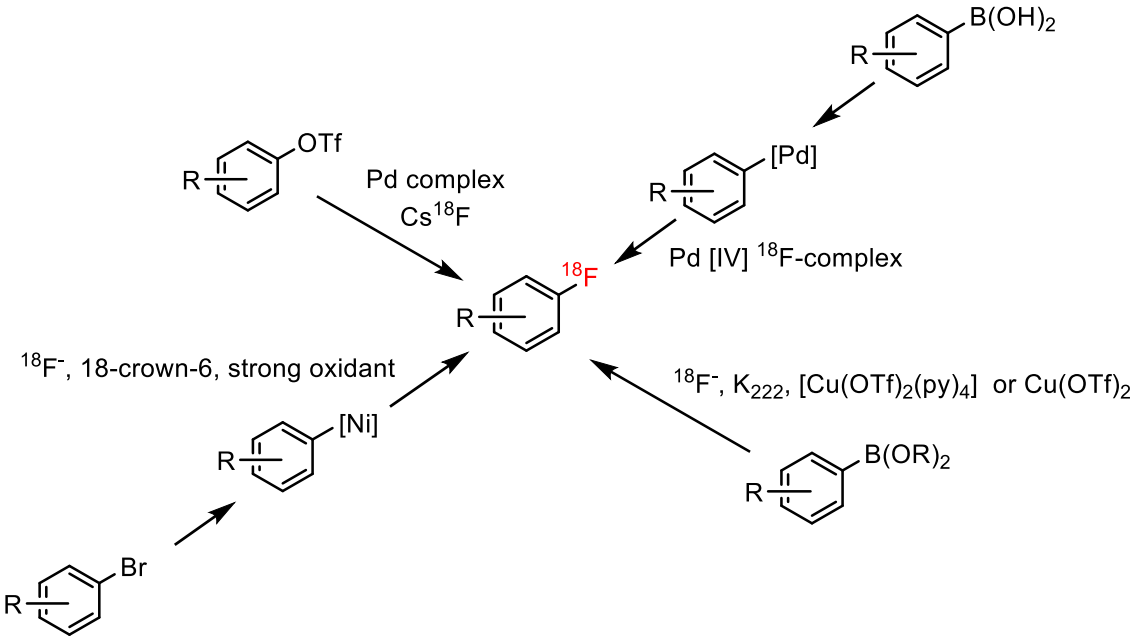

Source: Thesis author

The breakthrough was the introduction of copper-mediated radiofluorination reactions, mainly using arylboron precursors [199, 200]. The method is suitable for a wide variety of substrates, does not require the synthesis of complex labeling precursors, and can be performed in an open-to-air reaction vessel [165] (Figure 25). A few examples are the efficient synthesis of the EP4 receptor antagonist CJ-042794 [201] and different [^{18}F]fluoro-L-tryptophan derivatives (Figure 26) [202, 203].

This method is considered to be revolutionary in the radiochemistry field, allowing late-stage fluorination in many different substrates, meaning to

introduce ^{18}F selectively and reliably at any desired point in the synthetic route, rather than being restricted to the use of simple, commercially available precursors that after being radiofluorinated, are modified into building blocks [204].

Figure 25. Radiofluorination of aryl boronic acid pinacol ester derivates (above) developed by Tredwell, Matthew et al.[199] and radiofluorination of aryl boronic acids reported by Mossine, Andrew V et al. [205].

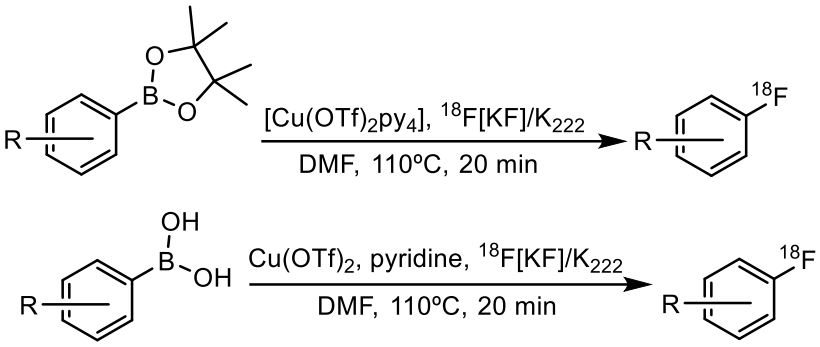

Source: Thesis author

Figure 26. Examples of late stage radiofluorination of aryl boronic acid pinacol ester precursors allowing a one-step synthesis. EP4 receptor antagonist CJ-042794 (above) and 5-[^{18}F]F-AMT (below).

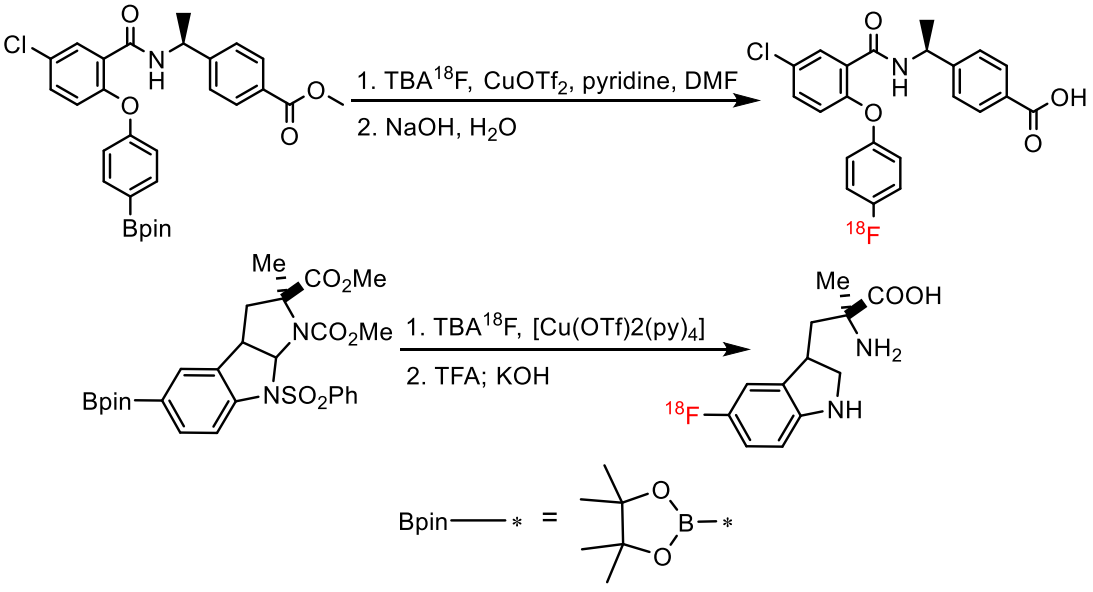

Source: Thesis author

3.8 Final considerations

An ideal hypoxia imaging agent should have high membrane permeability for easy access to intracellular mitochondria and low redox potential to confer stability in normal tissue, but it should be able to be reduced by mitochondria with abnormally high electron concentrations in hypoxic cells. In this context, nitroimidazole residues are not considered to be essential. As essential characteristics for hypoxia imaging agents, a candidate should have small molecular size as well as suitable lipophilicity for easy penetration through the cell membranes, including the blood-brain barrier.

Historically, nitroimidazoles derivates have been used as radiotracers for detection of hypoxia based on their previous introduction as radiosensitizers of hypoxic tumors and their good pharmacokinetic properties, specially 2-nitroimidazole derivates. In this regard, [^{18}F]FMISO is the most widely used radiopharmaceutical for imaging tumor hypoxia using PET, but its high lipophilicity causes slow tracer accumulation, slow plasma clearance and low tumor-to-background contrast. In the previous sections was discussed how several different radiotracers, most of them containing the 2-nitroimidazole moiety, have been synthetized and tested in order to solve these problems.

Nitrofuran derivates were also tested as sensitizers with good radiosensitizing activities but low stability and pharmacokinetic issues associated with their solubility and the presence of the hydrazone moiety, which under physiological conditions is readily hydrolyzed. Most of the nitrofuran-based compounds knew during the 1970s and 1980s were already being used for some time as antibiotic and antibacterial agents, and most included that hydrazone pharmacophore which in turn is responsible for some of the mentioned activity. 5-nitrofurans (-255 mV < E_7^1 < -450 mV) are more electron affinic than 2-nitroimidazoles (-321 mV < E_7^1 < -4^{18} mV), so one can think that more stable and pharmacokinetic-improved nitrofuran derivates, radiolabeled with a proper PET or SPECT radioisotope, could act as radiotracers for detection of hypoxic regions in cancer.

In a study reported by Valdez et al. (2009) [206], where the authors synthetized several 5-nitroimidazole derivates and tested their antimicrobial

activity against *Giardia lamblia*, compounds having olefins with a conjugated bridge connecting the nitroheterocycle and a substituted phenyl or heterocyclic ring showed greatly increased antigiardial activity without toxicity (Figure 27, A). Electrochemical studies carried out by Valdez et al. (determination of the half-wave potential of the initial one-electron transfer by cyclic voltammetry) showed that the electron delocalization in these compounds was associated with an easier redox activation and reduction, therefore correlated with greater antigiardial activity [206].

In another work published by Tawari, Nilesh R. et al. (2010) [207] that was actually in progress when Valdez et al. (2009) [206] published the study described above, the authors synthetized a series of potent nitrofuran-based antitubercular agents coupling electronegative α,β-unsaturated carbonyl bridge to the nitrofuran ring and substituted phenyl or heterocyclic rings (Figure 27, B). Based on density functional theory (DFT) and computational studies, these compounds were selected as strong candidates to become antitubercular agents because all of them possessed localized negative potential regions near the oxygen atom of the carbonyl group and both the oxygen atoms of the nitro group that extend laterally to the furan ring oxygen, due to electron delocalization, an idea that was previously reported by the same authors in an attempt to highlight structural features required for potent antitubercular activity [208]. One more time, the electron delocalization was linked to an improved electron affinity and latter good antitubercular activity and low toxicity [207].

This idea led us to think that a nitrofuran derivate, having that same α,β-unsaturated carbonyl bridge connecting the core nitroaromatic ring and a substituted phenyl ring could be used for detection of hypoxic regions. We would be avoiding the introduction of the physiologic-unstable hydrazone moiety that as previously mentioned was one of the main problems associated with early tested nitrofurans as radiosensitizers.

In a prior research, we synthetized and radiolabeled a new 2-nitroimidazole derivate (N-(4-[^{18}F]-Fluorobenzyl)-2-(2-nitro-1H-imidazol-1-yl)acetamide, [^{18}F]FBNA, Figure 27, C), for PET imaging of hypoxia which accumulates in gastric cancer cell lines AGS and MKN45 under hypoxic

conditions [40], therefore showing great chance of becoming a novel PET radioligand for imaging hypoxia. In this work, we propose the first use of nitrofurans as hypoxia specific PET radiotracers, radiolabeling a 5-nitrofuran derivate with ^{18}F and comparing its radiochemical and biological properties with that of [^{18}F]FBNA. Up to this moment, there are no reports in the literature on the use and radiolabeling of 5-nitrofuran derivates for detection of tumor hypoxia using PET or SPECT, taking advantage of their high electron affinity. These compounds have been studied and used for more than fifty years in different fields, so we propose their first use as imaging agents to target hypoxia.

This nitrofuran derivate, (E)-1-(4-fluorophenyl)-3-(5-nitrofuran-2-yl)prop-2-en-1-one, that was already synthetized as a "cold" molecule and tested as an antitubercular agent by Nilesh R. et al. [207], was here baptized as [^{18}/^{19}F]-FNPF (Figure 27, D). The use of radiolabeled nitrofuran derivates could be the breakthrough leading to a new series of non-nitroimidazole radiolabeled compounds for detection of hypoxia.

Figure 27. A) Compounds synthetized by Valdez et al. [206] B) Compounds obtained by Tawari et al. [207] C) [^{18}F]FBNA and D) [^{18}F]FNFP, proposed in this work.

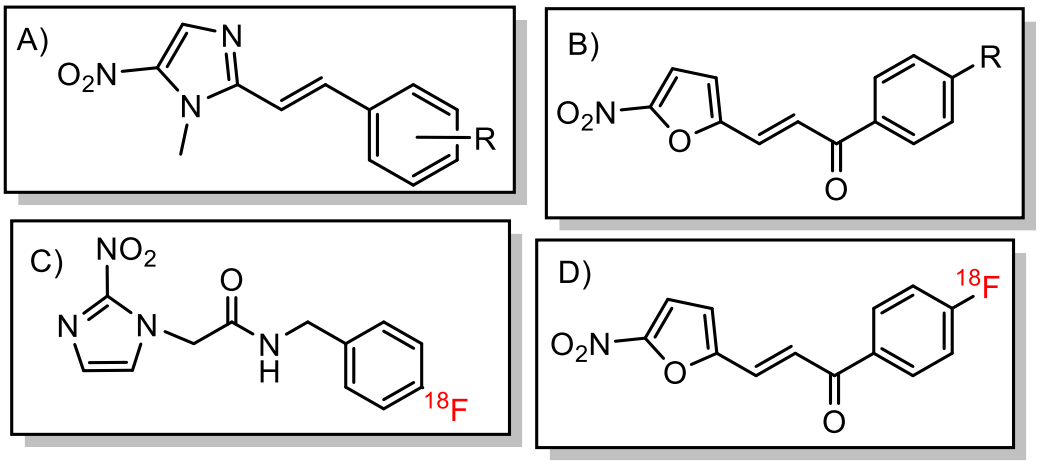

Source: Thesis author

4 EXPERIMENTAL SECTION

4.1 Materials

4.1.1 Analytical apparatus

Reactions were monitored by thin-layer chromatography (TLC) using silica gel 60 UV254 pre-coated silica gel plates from MERCK®. Detection was by means of a UV lamp. Flash column chromatography was performed on 300–400 mesh silica gel.

Commercial solvents and reagents, when necessary, were purified according to standardized methods in the literature [209]. Melting points were determined on a Buchi M-560 melting point apparatus BUCHI Brazil Ltda.

Nuclear Magnetic Resonance (NMR), one-dimensional and two-dimensional analyzes of ^{1}H ^{13}C nuclei were acquired with Bruker Avance spectrometers (USA) model DPX-300 MHz and DRX-600 MHZ and Bruker Ultra-Shield 300 spectrometer FT-NMR. Chemical shifts (δ) are described in parts per million (ppm) in relation to tetramethylsilane (TMS) or residual trace of the solvent used; the multiplicity of signs is represented in parentheses (s = simplet, sl = broad simplet, d = doublet, t = triplet, q = quadruplet, quint = quintuplet, dd = double doublet, ddd = double double doublet, tt = triple triplet, m = multiplet); the coupling constant (J), described in Hertz (Hz); and the number of hydrogens deduced from the relative integral.

Infrared (IR) spectra were obtained on a Fourier Transform Infrared Spectrometer (FTIR) Fourier Transform Infrared Spectrophotometer, IRTracer-100 (Shimadzu), in the spectral region from 4000 to 300 cm^{-1}, in cells or in KBr tablets, at the Faculty of Pharmaceutical Sciences of Ribeirão Preto (USP).

High resolution mass spectroscopy (HRMS) data were obtained on a Bruker Daltonics mass spectrometer, model microOTOF-Q II - ESI-Qq-TOF and 4000 QTRAP AB SCIEX in positive detection mode.

^{18}F-Fluoride $[^{18}F]F^-$ was produced by the $^{18}O(p,n)^{18}F$ nuclear reaction in an 18 MeV cyclotron (IBA, Belgium) using the $H_2{}^{18}O$ target. Sep-Pak Light QMA cartridges (Waters, Brazil) were pre-conditioned using two different methods: 1) 10 mL of 0.5 M K_2CO_3 solution, followed by 20 mL of Milli-Q water and purged with 5 mL of air; 2) 10 mL of 0.5M potassium triflate (KOTf), followed by 20 mL

of Milli-Q water and purged with 5 mL of air. Sep-Pak C18 Plus cartridges (Waters, Brazil) were pre-conditioned with 5 mL of ethanol and 10 mL of Milli-Q water and purged with 5 mL of air. Measurement of ^{18}F radioactivity was performed using a Carpintec dose calibrator (CRC-15R, New Jersey, USA). The Agilent High Performance Liquid Chromatography (HPLC) system (USA) was used for quality control of compounds labeled with ^{18}F. The system is equipped with a model 1260 quaternary pump, a model 1260 UV absorbance detector and a radioactivity detector (Raytest, Germany). Agilent Chem Station software was used to operate Agilent HPLC systems. The HPLC equipment with UV and radioactivity detector, as well as the column used for analysis (ZORBAX Eclipse Plus C18 Analytical 4.6 x 250 mm, 5 µm) are from Agilent Technologies, Brazil.

4.1.2 Laboratory Equipment

a) Rotary evaporators: Büchi RE-121 and Büchi R-215.

b) Scales: Mettler PE 400/Sartorius BP 121S and Mettler Toledo Excellence.

c) High vacuum pump: Precision Model D 150.

d) Ultraviolet light: Spectroline CM-10.

e) CEM® Discover microwave irradiation reactor.

f) Eppendorf Model 5702 centrifuge.

g) IKA RCT Basic and Corning PC-320 magnetic stirrers.

h) FANEM sterilization and drying oven.

i) Multifunction Refrigerator for Büchi Laboratory.

j) ThermoFisher Freezer -25ºC.

k) Braslab modulated exhaust hoods.

4.2 Methods

4.2.1 Chemical synthesis

4.2.1.1 General procedure for CDI-mediated coupling of carboxylic acids and amines

1,1′-Carbonyldiimidazole (CDI) (1.05 equiv) is weighed in a round-bottomed, single-necked flask under air, and the flask sealed with a rubber septum. The flask is filled with nitrogen, and afterwards a solution of the carboxylic acid (1 equiv) in anhydrous DMF is added dropwise with stirring. After 1 hour, a solution of the amine (1 equiv) in 1 mL of anhydrous DMF is added, and the mixture stirred at room temperature overnight. The solvent is removed, and the product is purified according to specific procedures.

4.2.1.2 Synthesis of [^{19}F]FBNA

Scheme 1. Synthesis of tert-butyl 2-(2-nitro-1H-imidazol-1-yl)acetate

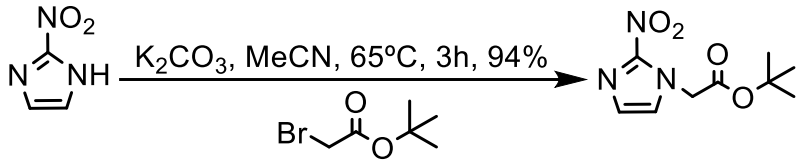

Source: Thesis author

A suspension of 2-nitroimidazole (1.13 g, 10 mmol) and anhydrous K_2CO_3 (1.2 equiv) in 50 mL of acetonitrile was stirred at 50ºC for 30 minutes. Then, tert-Butyl bromoacetate (1.1 equiv) was added dropwise, and the solution was stirred at 65ºC for 3h. The mixture was cooled to room temperature, filtered and the filtrate evaporated under reduced pressure. The residue was dissolved in ethyl acetate/water (1:1, 100 mL), the organic phase separated, and the aqueous layer was extracted twice with ethyl acetate. The combined organic layers were dried over anhydrous $NaSO_4$ and concentrated under reduced pressure to give 2.145 g of the product as a faint yellow solid in 94.4% yield. **^{1}H-NMR** (300 MHz, Chloroform-d) δ 7.17 (d, J=0.96 Hz, 1H); 7.10 (d, J=0.96 Hz, 1H), 5.01 (s, 2H), 1.46 (s, 9H); **m.p.** 109.7-110.3 ºC

Scheme 2. Synthesis of 2-(2-nitro-1H-imidazol-1-yl)acetic acid

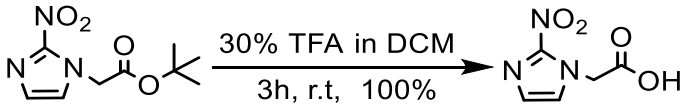

Source: Thesis author

To a 30% solution of trifluoroacetic acid in dichloromethane (15 mL) was added tert-Butyl 2-(2-nitroimidazol-1-yl)acetate (1.36 g, 6 mmol). The mixture was stirred at room temperature for 3 h and then evaporated under reduced pressure several times with methanol to remove traces of TFA. The residue was washed twice with a mixture of hexane/diethyl ether (1:1, v/v), and filtrated to afford 1.020 g of 2-(2-nitro-1H-imidazol-1-yl)acetic acid as a white solid in quantitative yield. **^{1}H-NMR** (300 MHz, Methanol-d4) δ 7.32 (s, 1H), 7.03 (s, 1H), 5.10 (s, 2H); **m.p.** ~138ºC decomposition

Scheme 3. N-(4-fluorobenzyl)-2-(2-nitro-1H-imidazol-1-yl)acetamide

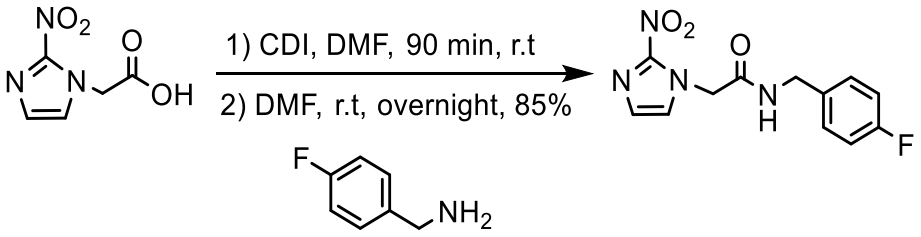

Source: Thesis author

N-(4-fluorobenzyl)-2-(2-nitro-1H-imidazol-1-yl)acetamide, [^{19}F]FBNA, was obtained by coupling 2-(2-nitro-1H-imidazol-1-yl)acetic acid with 4-fluorbenzylamine following general procedure 3.2.1.1.

2-(2-nitro-1H-imidazol-1-yl)acetic acid (171.1 mg, 1 mmol) was reacted with CDI (1.05 mmol) for 90 min. Then 4-fluorobenzylamine (1 mmol) was added. After stirring overnight, the solvent was removed under reduced pressure and a mixture of methanol/acetone/water (9.5/9.5/1.5) (5 mL) was added to the residue and the solution heated until dissolution occurred. Two volumes of acetone/methanol were removed under reduced pressure, and water was added dropwise to the flask over 5 minutes. The resulting slurry was then cooled to 0-5ºC and stirred for 1h. The precipitate was filtered and washed with ice cold methanol and dried under vacuum to give 236.5 mg of the product as a white solid in 85% yield. **^{1}H NMR** (300 MHz, DMSO-*d*6) δ 8.85 (t, *J* = 5.8 Hz, 1H), 7.63 (s, 1H), 7.31 (dd, *J* = 8.3, 5.8 Hz, 2H), 7.23 – 7.10 (m, 3H), 5.16 (s, 2H), 4.31 (d, *J* = 5.7 Hz, 2H). **m.p.** 194.5-195ºC.

4.2.1.3 Synthesis of [^{18}F]FBNA precursor

Scheme 4. Synthesis of 4-(aminomethyl)phenylboronic acid pinacol ester

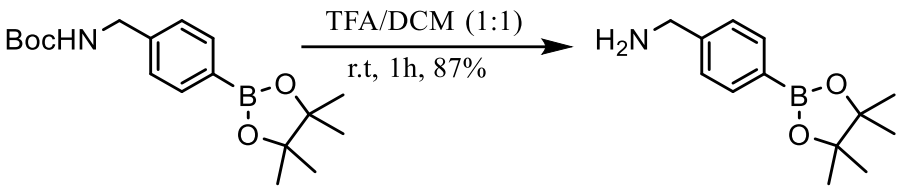

Source: Thesis author

4-(N-Boc-aminomethyl)phenylboronic acid pinacol ester (666.5 mg, 2 mmol) was dissolved in a mixture of dichloromethane/trifluoroacetic acid (1:1) (6 mL) at room temperature and stirred for 1h. The solvent was removed under reduced pressure, and the residue was neutralized with a saturated sodium bicarbonate solution (10 mL). This aqueous phase was extracted several times with ethyl acetate, the combined organic layers were dried over anhydrous Na_2SO_4, filtered, and concentrated in vacuo to give 420 mg of a white solid that was used in the next reaction without further purification.

Scheme 5. Synthesis of (4-((2-(2-nitro-1H-imidazol-1-yl)acetamido)methyl)phenyl)boronic acid pinacol ester

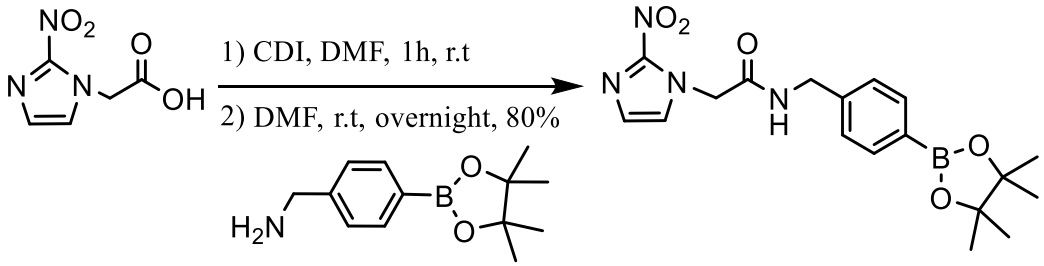

Source: Thesis author

(4-((2-(2-nitro-1H-imidazol-1-yl)acetamido)methyl)phenyl)boronic acid pinacol ester, ^{18}F-FBNA precursor, was obtained after coupling 2-(2-nitro-1H-imidazol-1-yl)acetic acid with 4-(aminomethyl)phenylboronic acid pinacol ester according to general procedure 3.2.1.1

2-(2-nitro-1H-imidazol-1-yl)acetic acid (171 mg, 1 mmol) was reacted with CDI (170.3 mg, 1.05 mmol) for 90 min. Then 4-(aminomethyl)phenylboronic acid pinacol ester (245 mg, 1.05 mmol) was added. After stirring overnight, the

solvent was removed under reduced pressure, and the residue was purified by flash column chromatography eluting with hexane/ethyl acetate (20:80) to 100% ethyl acetate to give 309 mg of the product as a white solid in 80% yield. **^{1}H-NMR** (600 MHz, DMSO-d6) δ 8.87 (t, J = 5.9 Hz, 1H), 7.65 (d, J = 8.0 Hz, 2H), 7.63 (s, 1H), 7.30 (d, J = 8.0 Hz, 2H), 7.20 (s, 1H), 5.18 (s, 2H), 4.35 (d, J = 5.9 Hz, 2H), 1.30 (s, 12H).**^{13}C-NMR DEPTQ** (151 MHz, DMSO-d_6) δ 167.44, 166.22, 145.40, 142.85, 134.93, 129.28, 127.94, 127.13, 84.07, 52.06, 42.80, 25.14. **m.p.** 166-167ºC. **Ion Trap Mass Spectrometry**, $[M+H]^+$=387,2; 2x$[M+H]^+$=774,4. **Infrared spectra:** υ (N–H secondary amide) 3251 cm^{-1}; υ (=C-H, sp_2 aromatic) 3106 cm^{-1}; υ (C-H, sp_3) 2979 cm^{-1}, 2926 cm^{-1}; carbonyl stretching vibration (-C=O) 1638 cm^{-1}; N–O asymmetric stretch 1487 cm^{-1}, N–O symmetric stretch 1357 cm^{-1}. υ (B-O stretching boronic acid ester) 1324 cm^{-1}.

4.2.1.4 Synthesis of [^{19}F]FNFP

Scheme 6. Synthesis of 5-nitro-2-furaldehyde diacetate

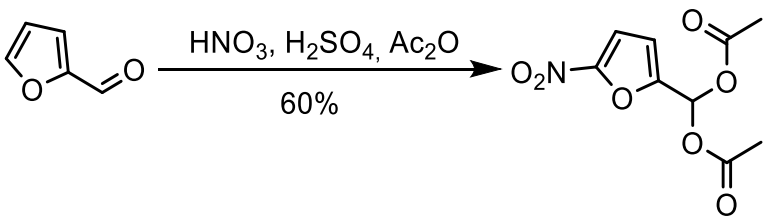

Source: Thesis author

Acetic anhydride (180 mL) was placed in a dried 500-mL three-necked, round-bottomed flask equipped with a mechanical stirrer and a thermometer, and afterwards the mixture was then cooled to -10ºC in a benzyl alcohol/dry ice bath. 17.2 mL of concentrated HNO_3 and 0.15 mL of concentrated H_2SO_4 were mixed in a small beaker, and this solution was slowly and carefully added into the chilled acetic anhydride while stirring between -10ºC and -5ºC. Afterwards, 20.8 mL (0.251 mol) of freshly distilled furfural were added dropwise over 20 minutes into the cold acid mixture with stirring at the same temperature, and the resulting solution was left to stir for 1 h between -10ºC and -5ºC. After this time 160 mL of water were added, and the mixture was left to stir at room temperature for 30 min, over which a white precipitate formed. A 10% NaOH solution was

added to the mixture until the pH rose to 2.5-2.7, and it was warmed on a water bath at 55ºC for 1h. The mixture was poured into crushed ice, stirred for 10 min and the white precipitate formed was filtered, washed with water, recrystallized twice from ethanol, and air-dried to provide 36.63 g of the product as a white crystalline solid in 60% yield. **^{1}H NMR** (300 MHz, Chloroform-d) δ 7.73 (s, 1H), 7.30 (d, J = 3.6 Hz, 1H), 6.75 (d, J = 3.6 Hz, 1H), 2.19 (s, 6H); **m.p.** 90-91 ºC.

Scheme 7. Synthesis of 5-nitro-2-furaldehyde

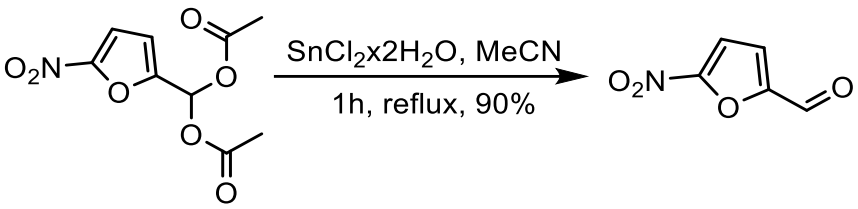

Source: Thesis author

To a solution of 5-Nitro-2-furaldehyde diacetate (4.864 g, 20 mmol) in acetonitrile (100 mL), was added $SnCl_2.2H_20$ (902.52 mg, 4 mmol, 20% mol) and the clear mixture was refluxed for 1h (turned dark after 20 min of reaction) when TLC (100% toluene) indicated completion. The solvent was evaporated, and the residue was purified by flash column chromatography eluting with chloroform to give 2.54 g of 5-nitro-2-furaldehyde as a yellow solid in 90% yield. **^{1}H-NMR** (600 MHz, Chloroform-d) δ 9.85 (s, 1H), 7.44 (dd, J = 3.8, 0.4 Hz, 1H), 7.38 (d, J = 3.8 Hz, 1H). **m.p.** 38-38.7ºC

Scheme 8. Synthesis of (E)-1-(4-fluorophenyl)-3-(5-nitrofuran-2-yl)prop-2-en-1-one

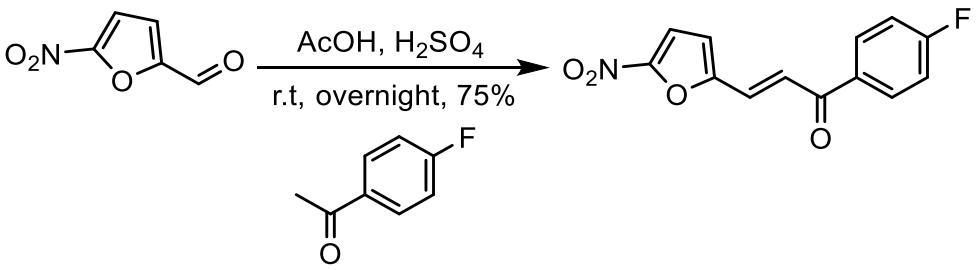

Source: Thesis author

(E)-1-(4-fluorophenyl)-3-(5-nitrofuran-2-yl)prop-2-en-1-one, [^{19}F]-FNFP, was obtained as follows:

5-nitro-2-furaldehyde (988 mg, 7 mmol) was dissolved in 10 mL of glacial acetic acid at room temperature. 400 µL of concentrated sulfuric acid and 4-fluoroacetophenone (7 mmol, 846 µL) were added in sequence, and the mixture was stirred at room temperature overnight. Ice-cold water (50 mL) was added, the solid was recovered by filtration and washed carefully with ice cold ethanol. The product was then recrystallized from ethanol to yield 1.37 g of (E)-1-(4-fluorophenyl)-3-(5-nitrofuran-2-yl)prop-2-en-1-one as yellow needles in 75% yield. **^{1}H-NMR** (600 MHz, DMSO-d_6) δ 8.26 – 8.20 (m, 2H), 7.89 (d, *J* = 15.6 Hz, 1H), 7.83 (d, *J* = 3.9 Hz, 1H), 7.61 (d, *J* = 15.6 Hz, 1H), 7.47 (d, *J* = 3.9 Hz, 1H), 7.45 – 7.41 (m, 2H). **m.p.** 183-184ºC

4.2.1.5 Synthesis of [^{18}F]FNFP precursor

Scheme 9. Synthesis of 4-acetylphenylboronic acid pinacol ester

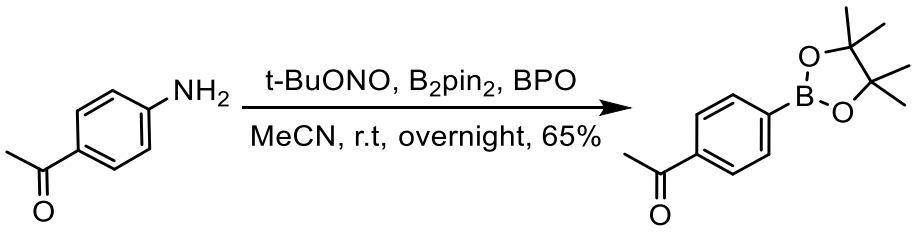

Source: Thesis author

4-aminobenzophenone (1.352 g, 10 mmol), bis(pinacolato)diboron (2.667 g, 10.5 mmol, 1.05 equiv.) and benzoyl peroxide (20.4 mg, 0.08426 mmol, 2% mol) were weighted in a 50 mL round-bottom flask. To this mixture, anhydrous acetonitrile (15 mL) was added, and then tert-butyl nitrite (1.785 mL, 15 mmol, 1.5 equiv.) in 5 mL of anhydrous acetonitrile was added dropwise at room temperature with stirring. The resulting mixture was stirred at room temperature overnight, and the solvent was removed under reduced pressure. The residue was purified by flash column chromatography eluting with hexanes/ethyl acetate 1/50 to 1/20 to give 1.6 g of 4-acetylphenylboronic acid pinacol ester as a white-off crystalline solid in 65% yield. **^{1}H-NMR** (600 MHz, Chloroform-d) δ 7.85 – 7.77 (m, 4H), 2.51 (s, 3H), 1.26 (s, 12H); **m.p.** 59-60ºC.

Scheme 10. Synthesis of (E)-(4-(3-(5-nitrofuran-2-yl)acryloyl)phenyl)boronic acid pinacol ester

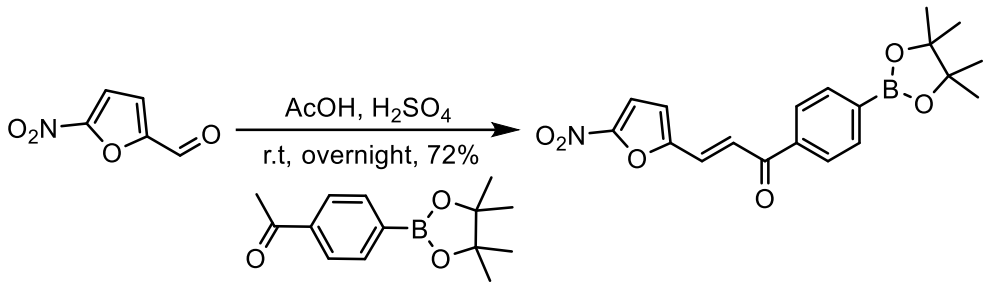

Source: Thesis author

(E)-(4-(3-(5-nitrofuran-2-yl)acryloyl)phenyl)boronic acid pinacol ester, [^{18}F]FNFP precursor, was obtained as follows:

5-nitro-2-furaldehyde (168 mg, 1.2 mmol) was dissolved in 1.5 mL of glacial acetic acid at room temperature. 120 µL of concentrated sulfuric acid and 4-acetylphenylboronic acid pinacol ester (295.3 mg, 1.2 mmol) were added in sequence, and the mixture was stirred at room temperature overnight. Ice-cold water (5 mL) was added, the solid was recovered by filtration and washed carefully with ice cold ethanol. The product was then recrystallized from ethanol to yield 319 mg of (E)-(4-(3-(5-nitrofuran-2-yl)acryloyl)phenyl)boronic acid pinacol as yellow needles in 72% yield**. ^{1}H NMR** (600 MHz, DMSO-d_6) δ 8.12 – 8.10 (m, 2H), 7.89 – 7.84 (m, 3H), 7.83 (d, *J* = 3.9 Hz, 1H), 7.62 (d, *J* = 15.6 Hz, 1H), 7.47 (d, *J* = 3.9 Hz, 1H), 1.33 (s, 12H). **^{13}C-NMR DEPTQ** (151 MHz, DMSO-d6) δ 153.60, 152.50, 139.30, 135.30, 129.41, 128.28, 125.31, 118.52, 115.26, 84.62, 25.15; **m.p**. 170-171ºC. **ESI-mass spectrometry**. $[M+Na]^+$=392,1274 expected MW=369,18 g/mol. **Infrared spectra:** υ (=C-H) aromatic 3118 cm^{-1}; υ (C-H) 2929 cm^{-1}; carbonyl stretching vibration for the enone (=C-C=O) 1661 cm^{-1}; N–O asymmetric stretch 1479 cm^{-1}, N–O symmetric stretch 1365 cm^{-1}; υ (B-O stretching boronic acid ester) 1342 cm^{-1}.

4.2.2 Radiochemistry

4.2.2.1 Radiosynthesis of [^{18}F]FBNA and [^{18}F]FNFP

Two different procedures were evaluated for the radiosynthesis of [^{18}F]FBNA and [^{18}F]FNFP.

Scheme 11. Synthesis of [^{18}F]FBNA following method 1 and according to the procedure reported by Tredwell, Matthew et al.[199].

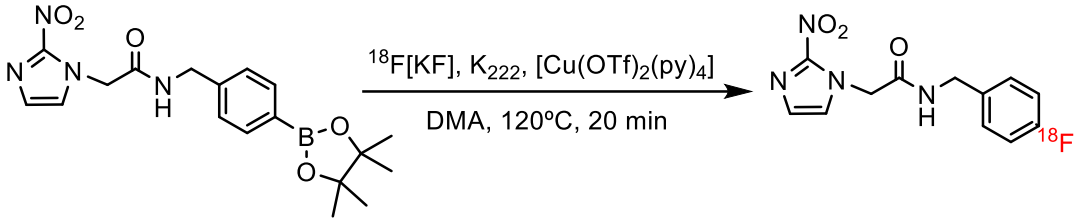

Source: Thesis author

Method 1, [^{18}F]FBNA: [^{18}F]FBNA was obtained following the procedure reported by Tredwell, Matthew et al.[199] (scheme 11). Briefly, the fluoride ion ($^{18}F^-$) solution was trapped in an anionic Sep Pak light QMA cartridge, previously conditioned with K_2CO_3 0.5 M and water, and the $^{18}F^-$ was then eluted into the reaction vial with a mixture of K_2CO_3 (2.8 mg; 20 µmol) and Kryptofix 2.2.2 (15 mg; 40 µmol) in 1 mL of acetonitrile/water (8:2). Then, the solution was subjected to three cycles of azeotropic distillation with anhydrous acetonitrile (1mL) at 100°C under a nitrogen flow. Afterwards, [^{18}F]FBNA precursor (5 mg, 13 µmol) in 150 µL of anhydrous DMA and [Cu(OTf)$_2$(py)$_4$] (8.8 mg, 13 µmol) in 150 µL of DMA were added and the resulting solution was stirred at 120ºC for 20 min under air, quenched with water (300 µL) and an aliquot was removed for analysis by radio-HPLC to calculate the RCY and identify the product, respectively. The mixture was then taken up in water (20 mL) and passed through a pre-conditioned C18 plus cartridge. [^{18}F]FBNA was then eluted from the C18 with 1 mL of ethanol and purified by semipreparative HPLC using MiliQ water (0.1% trifluoroacetic acid), channel A, and acetonitrile, channel B, with an isocratic run using 70% A and 30% B in 20 minutes, with a flux of 3 mL/min.

Scheme 12. Synthesis of [^{18}F]FNFP following method 1 and according to the procedure reported by Tredwell, Matthew et al.[199].

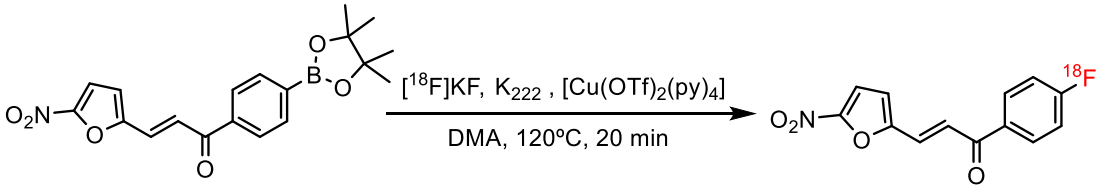

Source: Thesis author

Method 1, [^{18}F]FNFP: [^{18}F]FNFP was obtained following the same protocol as that of [^{18}F]FBNA for radiofluorination of aryl boronic esters reported by Tredwell, Matthew et al.[199]. [^{18}F]FNFP precursor (4.8 mg, 13 µmol) and [Cu(OTf)2(py)4] (8.8 mg, 13 µmol) were used. After HPLC analysis, the mixture was then taken up in water (20 mL) and passed through a pre-conditioned C18 plus cartridge. [^{18}F]FNFP was then eluted from the C18 with 1 mL of ethanol and purified by semipreparative HPLC using MiliQ water (0.1% trifluoroacetic acid), channel A, and acetonitrile, channel B, with a gradient run using 10%-100% of B in 20 minutes, with a flux of 3 mL/min.

Scheme 13. Radiosynthesis of [^{18}F]FBNA described in method 2 following the procedure reported by [210].

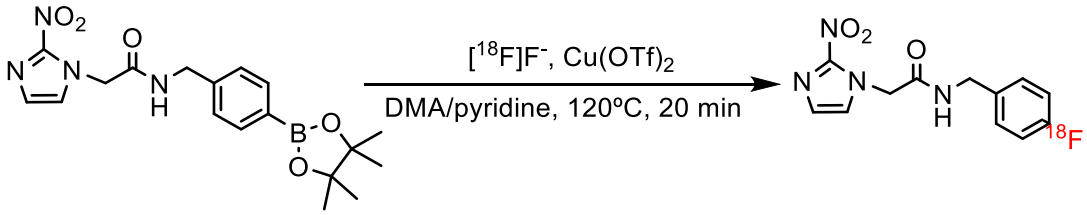

Source: Thesis author

Method 2, [^{18}F]FBNA: [^{18}F]FBNA was obtained according to scheme 13 following the procedure reported by Lahdenpohja, S.O., Rajala, N.A., Rajander, J. et al. [210]. Briefly, the fluoride ion ($^{18}F^-$) solution (80-100 mCi, approximately 1-2 mL) was diluted in 8-10 mL of fresh miliQ water in a flask. This solution was taken up in a 20 mL syringe and passed through a pre-conditioned anionic QMA cartridge, previously conditioned with KOTf and water. The cartridge was slowly washed with 5 mL of anhydrous DMA, and the [^{18}F]$^-$ was then eluted with a solution of $Cu(OTf)_2$ (34.7 mg, 96 µmol) in anhydrous DMA (0.5 mL) into the reaction vial already containing [^{18}F]FBNA precursor (5.8 mg, 15 µmol) diluted in 50 µL of anhydrous DMA and 50 µL of anhydrous pyridine. The QMA cartridge was washed with 0.5 mL of anhydrous DMA into the reaction vial, giving a total volume of 1.1 mL, and the resulting blue solution was stirred at 120ºC for 20 min under air. The reaction was quenched with water (500 µL) and an aliquot was

removed for analysis by radio-HPLC to calculate the RCY and identify the product, respectively. The following purification step was the same as for the other radiosynthesis.

Scheme 14. Radiosynthesis of [^{18}F]FNFP described in method 2 following the procedure reported by [210].

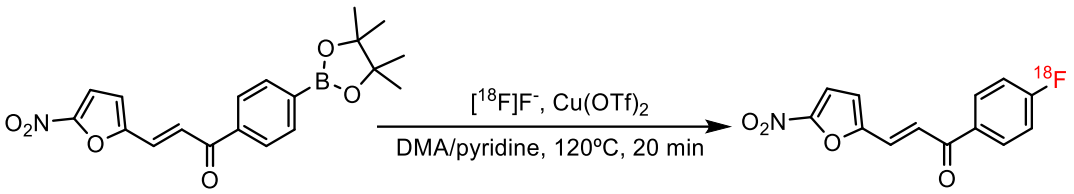

Source: Thesis author

[^{18}F]FNFP was obtained following the same protocol as that of [^{18}F]FBNA for radiofluorination of aryl boronic acid derivates reported by Lahdenpohja, S.O., Rajala, N.A., Rajander, J. et al. [210]. [^{18}F]FNFP precursor (5.5 mg, 15 µmol) and $Cu(OTf)_2$ (34.7 mg, 96 µmol) were used. After stirring at 120ºC for 20 min, the reaction was quenched with water (500 µL) and an aliquot was removed for analysis by radio-HPLC to calculate the RCY and identify the product, respectively. The mixture was then taken up in water (20 mL) and passed through a pre-conditioned C18 plus cartridge. [^{18}F]FNFP was then eluted from the C18 with 1 mL of ethanol and purified by semipreparative HPLC using MiliQ water (0.1% trifluoroacetic acid), channel A, and acetonitrile, channel B, with a gradient run using 10%-100% of B in 20 minutes, with a flux of 3 mL/min.

After HPLC purification, the acetonitrile/water mixture containing [^{18}F]FNFP was diluted with 15 mL of miliQ water and passed through a pre-conditioned Sep-Pak Light C18 cartridge and eluted with 0.3 mL of ethanol in a flask. After heating at 50ºC under a N_2 gas flow for 10 min, the solvent was evaporated, and the product solubilized in a 300 µL PBS solution for further biological studies.

4.2.2.2 Quality control

Aliquots of the final formulation of labeled compounds [^{18}F]FBNA and [^{18}F]FNFP and standard (cold) compounds [^{19}F]FBNA and [^{19}F]FNFP were analyzed by HPLC to determine chemical purity, radiochemical purity, molar

activity and confirm chemical identity. The compounds were analyzed with the following analysis conditions:

- [^{18}F]FBNA and [^{19}F]FBNA

-Stationary phase: ZORBAX Eclipse Plus C18 Analytical column 4.6 x 250 mm (5 µm).

-Mobile phase: Solvent (A) Milli Q water 0.1%TFA, Solvent (B) 100% Acetonitrile

-Running: Isocratic 70(A) : 30% B for 20 min.

-Injection: 20 µCi for [^{18}F]FBNA and 5 µg for [^{19}F]FBNA.

-Flow: 1 mL/min.

-Wavelength: 300 nm.

- [^{18}F]FNFP and [^{19}F]FNFP

-Stationary phase: ZORBAX Eclipse Plus C18 Analytical column 4.6 x 250 mm (5 µm).

-Mobile phase: Solvent (A) Milli Q water 0.1%TFA, Solvent (B) 100% Acetonitrile

-Running: Gradient, 90%(A) : 10% B to 100% B for 20 min.

-Injection: 20 µCi for [^{18}F]FNFP and 5 µg for [^{19}F]-FNFP.

-Flow: 1 mL/min.

-Wavelength: 350 nm.

The pH of the final solution was determined using pH test strips; an aliquot of the sample was deposited in the test region of the indicator strip and, after 1 minute, a colorimetric comparison was made with the standard provided by the manufacturer. The chemical identities of the labeled compounds were determined by co-injection with their standard (cold) compounds, respectively, in analytical HPLC.

4.2.3 Determination of molar activity

Molar activity was determined following a procedure reported by Chen, W. et al. [211]. Briefly, a standard curve of the corresponding fluorinated “cold” standard compound [Y axis = UV area, X axis = mole number (µmol)] was created from the HPLC trace from a standard solution of [^{19}F]FBNA or [^{19}F]FNFP. The radiolabeled product from the labeling reaction was collected and purified via HPLC; the UV area overlapping with the radio peak was then recorded. The standard curve was used to calculate mole number. Dividing the product decay corrected activity by the mole number gives the molar activity in GBq/µmol.

4.2.4 *In vitro* stability of [^{18}F]FNFP PBS and serum

[^{18}F]FNFP stability was assessed at room temperature in 0.1 mol/L PBS at pH=7.2. The samples had an activity of 37 MBq (1 mCi) of [^{18}F]FNFP in a final volume of 1 mL. The stability of the compound was monitored for 6 hours (immediately after the synthesis, 1, 3 and 6 hours after synthesis) and the results analyzed by HPLC as described in the previous section. The stability of the final formulation was also evaluated in Nude serum. In this case, an aliquot of 800 µL (1 mCi) was added to 500 µL of freshly separated serum, and the mixture was incubated at 37°C for up to 6 hours. Aliquots of 100 µL were withdrawn at different times (immediately after the synthesis, 1, 3 and 6 hours after synthesis) and 100 µL of acetonitrile were added to precipitate serum proteins. Then the solution was centrifuged (5000 rpm, for 10 min) and the supernatant was analyzed by HPLC.

4.2.5 [^{18}F]FNFP lipophilicity measurements

The lipophilicity of [^{18}F]FNFP was determined by measuring the octanol-water partition coefficient as described by Barthel, H., Wilson, H., Collingridge, D. *et al.* [212] with some modifications. Briefly, 80 –100 µCi (2.96 – 3.70 MBq) of [^{18}F]FNFP was dissolved in distilled H_2O in a 10 mL falcon tube to a final volume of 0.5 ml and 0.5 ml of octan-1-ol (Sigma-Aldrich Brasil LTDA) was added. The tube was capped and shaken vigorously for 2-3 min and subsequently centrifuged for 30 min (5000 rpm; Rotina 35R, Hettich Zentrifugen, Tuttlingen, Germany). Aliquots (100 µL) of the resulting top layer (representing [^{18}F]FNFP dissolved in octanol), and bottom layer ([^{18}F]FNFP dissolved in H_2O)

were taken and the radioactivity in these samples was measured using a dose calibrator, CRC – 10BC, Carpintec Inc., USA. Eight octanol –H_2O mixtures were analyzed (n=8), and the octanol –water partition coefficient was calculated by dividing the octanol-containing radioactivity by the water-containing radioactivity:

$$P = \frac{A(organic\ phase)}{A(aqueous\ phase)}$$

A (organic phase): activity (CPM) in the organic phase (n-octanol).

A(aqueous phase): activity (CPM) in the aqueous phase (water).

4.2.6 Biological studies

4.2.6.1 Gastric Cancer Model (MKN45)

The gastric cancer cell line MKN45 (American Type Culture Collection (ATCC) was cultivated in 175 cm² plastic bottles, containing 25 mL of RPMI culture medium (Invitrogen) and supplemented with 10% fetal bovine serum (GIBCO) and a solution of antibiotic and antimycotic (Sigma) containing penicillin (100 U/mL), Streptomycin (100 µg/mL) and amphotericin B (0.025 µg/mL) and maintained in a humid oven at 37 ºC and 5% CO_2. The cells were maintained following their growth and expansion time. Subsequently, the cells were washed with 5 mL of PBS solution, detached using 2 mL of ATV solution (association of versene trypsin) and placed in an oven at 37 ºC for 3 minutes. After this period the ATV solution was inactivated using 5 mL of supplemented RPMI medium. The cell suspension was aspirated with the aid of a 10 mL serological pipette and transferred to a 50 mL Falcon-type tube. This tube, properly closed, was taken for centrifugation for 3 minutes at 500 g. After centrifugation, the supernatant was discarded, and the resulting pellet was released by gently tapping the tube and resuspended in RPMI medium. 10 µL of the cell suspension was mixed with 10 µL of 0.4% Trypan Blue solution, and the mixture was transferred to a hemocytometer to count the cells and determine cell viability, with the aid of an optical microscope. Only refringent cells were considered viable, and only samples with viability greater than 90% were used. The counting result was corrected for the total volume of the suspension, and thus calculated for the desired assay.

4.2.6.2 Tumor-bearing mice model

In vivo studies were performed in Balb/c/Nude mice, seven to twelve weeks old and weighing approximately 24-26 grams provided by the IPEN vivarium - CNEN/SP. All experiments were previously approved by the Research Ethics Committee of the Institute for Energy and Nuclear Research (Project N.205/18/CEUA-IPEN/USP) and carried out in accordance with the standards established by the Brazilian Society of Science in Laboratory Animals.

The animals were kept in the vivarium in SPF (Specific Pathogen Free), changed twice a week and maintained under the following experimental conditions: room temperature: 22±2º C; artificial lighting with a 12-hour light/12-hour dark cycle; food and water ad libitum.

All procedures were carried out in accordance with the ethical standards established by the Brazilian College of Animal Experimentation (COBEA) and approved by the Animal Experimentation Ethics Committee of IPEN-CNEN/SP (Project N.154/15/CEUA-IPEN/USP) .

In vivo assays with [^{18}F]FNFP were performed using the gastric cancer tumor model. For this, the animals were inoculated subcutaneously with 1x10^{6} MKN45 cells diluted in PBS on the left flank. When the tumor reached approximately 300 mm^{3} (approximately 15-20 days), animals were separated for μPET imaging and *ex vivo* biodistribution studies.

4.2.6.3 Dynamic μPet/CT Imaging

Mice were anesthetized (2-3% isoflurane in 100% oxygen) and positioned with the tumor in the center of the equipment's field of vision. Image acquisition began after administration of the radiopharmaceutical [^{18}F]FNFP intravenously at a concentration of ~ 20 MBq/100 μL diluted in saline solution (0.9% NaCl). PET images were acquired using the Albira (Bruker) microPET/CT, using a dynamic image up to 180 minutes after injection, and recorded using an 80 mm field of view. The CT was performed using the standard 45Kev 400μA protocol.

The images were reconstructed with an algorithm by Albira Software. PET images were analyzed using pMOD software (PMOD® Technologies, Zurich).

Data were corrected and expressed as maximum standardized uptake values (SUV max).

4.2.6.4 *Ex-vivo* biodistribution studies

8 Balb/c nude mice with xenografts of MKN45 cells (10^6 cells/animal) were intravenously injected with 10 MBq of [^{18}F]FNFP. One hour after injection (group 1, n=4) and three hours after injection (group 2, n=4), the animals were euthanized, and the organs of interest (heart, lungs, liver, kidneys, stomach, intestines, spleen, muscle, bone, pancreas, bladder, brain and tumor) were harvested, rinsed in PBS, weighed, and counted using a Perkin Elmer (Waltham, MA, USA) Wizard2 2480 automatic gamma counter to quantify the percentage of injected dose per gram of tissue (%ID/g).

4.2.7 Statistical analysis

Data was expressed as the mean ± standard deviation (SD). Results of the RCCD were statistically processed by an analysis of variance (multifactor ANOVA) using the software STATGRAPHICS Plus *version 5.0*. The rest of the statistical analysis was performed using GraphPad Prism 7.01 Software. One unpaired t-test (multiple t tests) was used to analyze the ex *vivo* assays. One-way ANOVA (Dunnett´s multiple comparisons test) was used to compare each tissue uptake to blood at the *ex vivo* biodistribution data. The outliers were removed before analyzing the data. A <0.05 p-value was considered statistically significant.

5 RESULTS AND DISCUSSION

5.1…Chemical synthesis

5.1.1 Synthesis of [^{19}F]FBNA

N-(4-fluorobenzyl)-2-(2-nitro-1H-imidazol-1-yl)acetamide [^{19}F]FBNA was obtained in three steps (scheme 16), in a synthesis different from the one reported by our group in [40] showed in scheme 15. First, 2-nitroimidazole was alkylated in the presence of tert-butyl bromoacetate and potassium carbonate to obtain tert-butyl 2-(2-nitro-1H-imidazol-1-yl)acetate, and then this ester was hydrolyzed in the presence of trifluoroacetic acid to the corresponding carboxylic acid as reported in [213]. Finally, [^{19}F]FBNA was obtained after 1,1'-Carbonyldiimidazole-mediated coupling of 2-nitromidazol-1-yl-acetic acid with 4-fluorobenzylamine, following a procedure reported in [214]. Schemes 15 and 16 show the differences between the previous reported method [40] and the one described in this work, with the latter showing a better step-by-step and overall yield.

Scheme 15. Synthesis of [^{19}F]FBNA as reported by Nario, A. P. et al. [40].

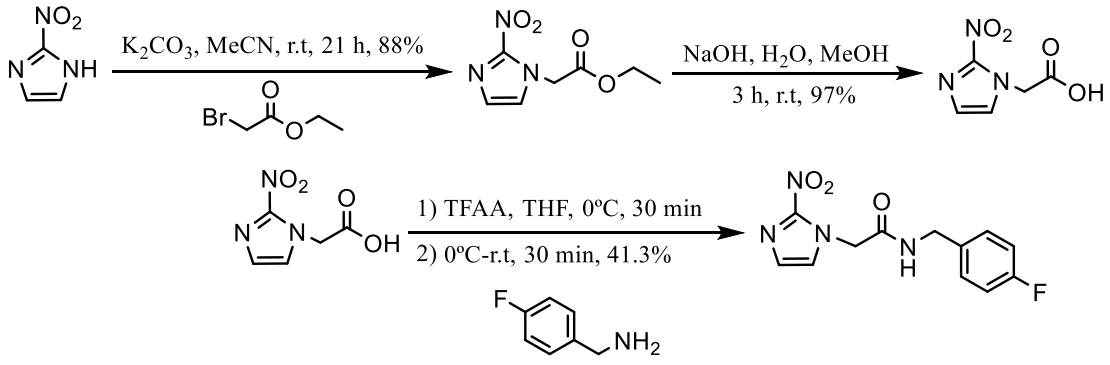

Source: Thesis author

Scheme 16. Synthesis of [^{19}F]FBNA reported in this work.

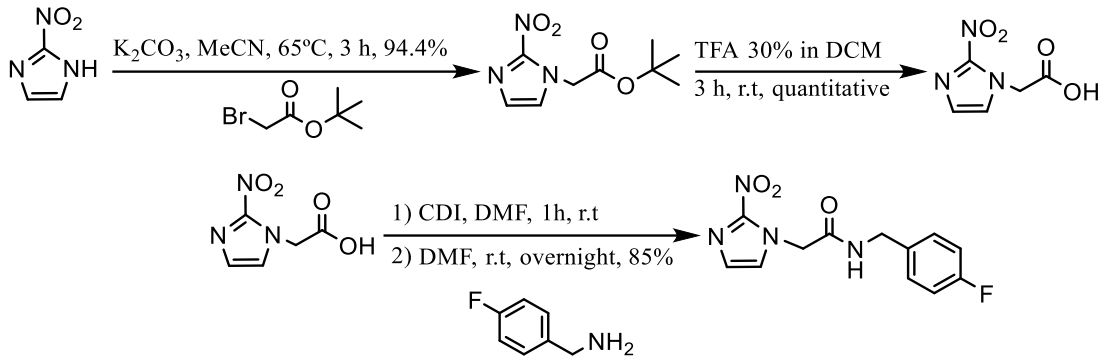

Source: Thesis author

In this work, an optimized method to obtain [^{19}F]FBNA was followed by first synthetizing a tert-butyl ester derivate of 2-nitroimidazol instead of an ethyl ester as reported in [40]. The former requires an acid hydrolysis to obtain the desired carboxylic acid for the next coupling step, that in our case here was achieved in quantitative yield. The purification step corresponding to the hydrolysis of the ester intermediate under basic conditions previously reported [40] required the use of a cation-exchange resin (H + , Bio-Rad, 4 g), which had been conditioned by washing with 1.N H_2SO_4 (10 mL) and distilled water, to acidify the solution after the starting material was consumed as indicated by TLC. Then flash column chromatography was used to purify the carboxylic acid [40]. In this work, the acid hydrolysis of tert-butyl 2-(2-nitro-1H-imidazol-1-yl)acetate yielded the corresponding carboxylic acid in quantitative yield as mentioned before, with no further purification needed.

1,1'-Carbonyldiimidazole is a well-stablished and widely used reagent in organic synthesis for the condensation of carboxylic acids and amines through the acyl imidazole intermediate. The reagent is cheap, readily available in kilogram quantities with innocuous by-products (carbon dioxide and imidazole), so no need for complicated purification steps is required [215, 216]. In the last step for our synthesis, CDI-mediated coupling yielded [^{19}F]FBNA in 85% after a simple recrystallization; in the previously reported method, trifluoroacetic anhydride was used to activate the carboxylic acid through the asymmetrical anhydride method, then obtaining the final product in 41.3% yield after column chromatography [40].

The optimizations carried out in this work let us to achieve better yields and easier purification procedures compared to the already-reported ones [40].

5.1.2 Synthesis of [^{18}F]FBNA precursor

CDI is a widely used condensation agent for the preparation of functional groups, for example amides, anhydrides, amidines, carboxylic acids, sulfonic acids, esters, and are mild oxidizing agents as well [217]. In most cases, coupling carboxylic acids with amines (or amine salts) in the presence of CDI has the advantage of producing easily separable compounds: gaseous carbon dioxide and water-soluble by-products (carboxylic acids, imidazole, and amines, the last two existing either as free bases or as hydrochloride salts) [215, 217, 218]. First, the acid is reacted with CDI to form the acyl imidazole-reactive intermediate, and then the amine is added, and the reaction mixture stirred at room temperature normally overnight.

Those previously mentioned benefits make CDI an excellent reagent for activating amide-coupling reactions at scale; however, CDI is not without its drawbacks. Slow reaction rates between aromatic and secondary amines and the acyl imidazole intermediates, and the need of dry organic solvents under an inert atmosphere have limited the scope of the reaction in the pharmaceutical and the fine chemicals industries [215]. However, some solvent-free protocols [215, 218] and have been reported, reducing the time for CDI mediated amidation from 2–4 h to 5–10 min [215].

(4-((2-(2-nitro-1H-imidazol-1-yl)acetamido)methyl)phenyl)boronic acid, pinacol ester, [^{18}F]FBNA precursor, was obtained in two steps as shown in scheme 17. First, 4-(aminomethyl)phenylboronic acid pinacol ester was obtained after deprotection of 4-(N-Boc-aminomethyl)phenylboronic acid pinacol ester in the presence of trifluoroacetic acid. After removing the solvent, the free amine was isolated following neutralization with saturated $NaHCO_3$ solution and extraction with ethyl acetate.

Scheme 17. Synthesis [^{18}F]FBNA precursor in two steps.

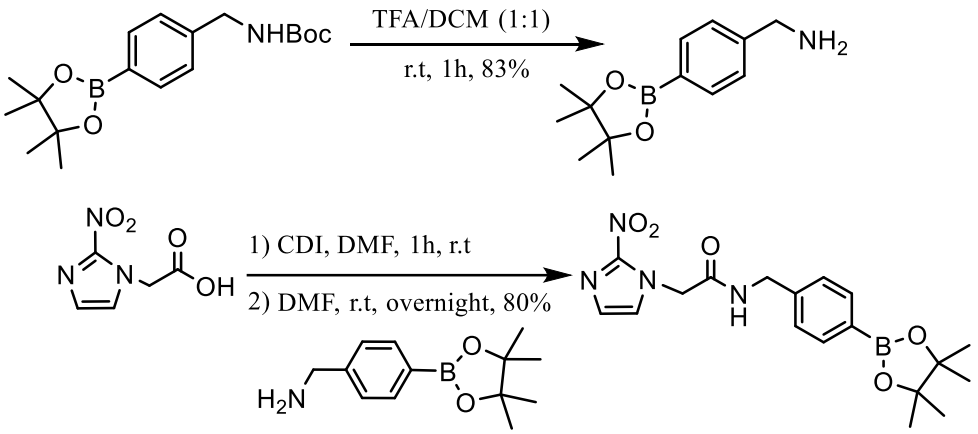

Source: Thesis author

CDI-mediated coupling of the previously obtained amine and 2-nitroimidazol-1-yl acetic acid yielded [^{18}F]FBNA precursor in 80% yield. No other “more classical” coupling methods or protocols (through the acyl chloride, carbodiimides such as DCC or EDC or active NHS esters) were tested since CDI worked out very well.

5.1.3 Synthesis of [^{19}F]FNFP

(E)-1-(4-fluorophenyl)-3-(5-nitrofuran-2-yl)prop-2-en-1-one, [^{19}F]-FNFP, was obtained after 3 steps starting with furfural (2-furaldehyde, scheme 18).

Scheme 18. 3-step-pathway for the synthesis of (E)-1-(4-fluorophenyl)-3-(5-nitrofuran-2-yl)prop-2-en-1-one, [^{19}F]FNFP.

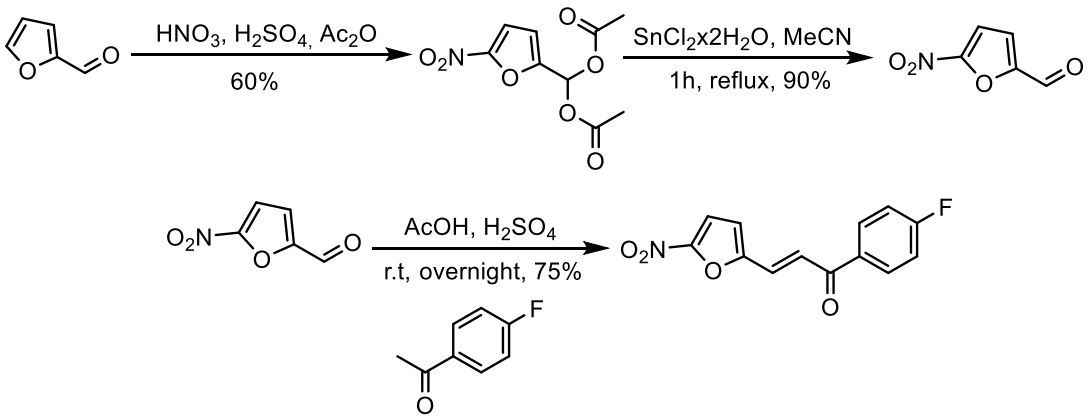

Source: Thesis author

Nitration of furfural in acetic anhydride in the presence of catalytic H_2SO_4 and HNO_3 yielded 5-nitro-2-furaldehyde diacetate in 60% yield after recrystallization from ethanol [219]. The 1,1-diacetate (acylal) protecting group was removed in refluxing acetonitrile in the presence of catalytic $SnCl_2xH_2O$ to yield 5-nitro-2-furaldehyde after column chromatography in silica gel, as reported by Mohammadpoor-Baltork et. al. [220]. This approach is a different perspective compared to the traditional acidic deprotection of acylals carried out with strong protic acids (HCl, H_2SO_4), using the inexpensive $SnCl_2xH_2O$ Lewis acid, that for example selectively cleaves aryl aldehyde diacetates but does not cleave the phenolic acetate function [220].

Scheme 19. Examples of acylals deprotection as reviewed by Mohammadpoor-Baltork et. al. showing selectivity for diacetals in the presence of phenolic acetates [220].

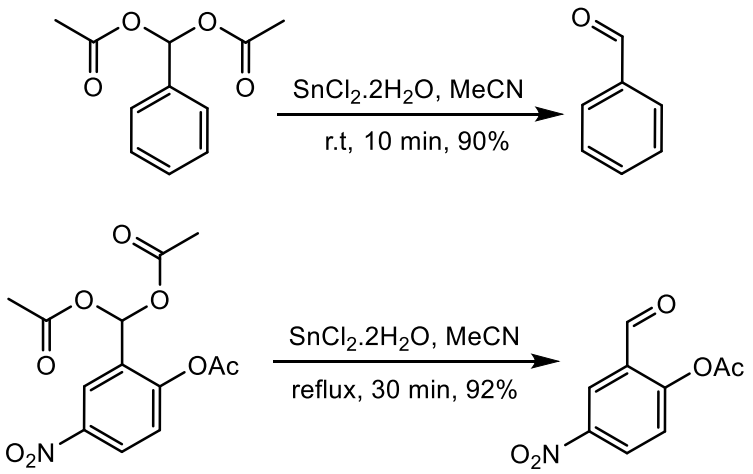

Finally [^{19}F]FNFP was obtained after condensation of 5-nitro-2-furaldehyde with 4-fluoroacetophenone under acidic conditions and recrystallization of the final product in ethanol, as reviewed by Tawari, Nilesh R et al. [207].

5.1.4 Synthesis of [^{18}F]FNFP precursor

(E)-(4-(3-(5-nitrofuran-2-yl)acryloyl)phenyl)boronic acid pinacol ester, [^{18}F]FNFP precursor, was obtained in two steps (scheme 20).

Scheme 20. Synthesis of [^{18}F]FNFP precursor in two steps.

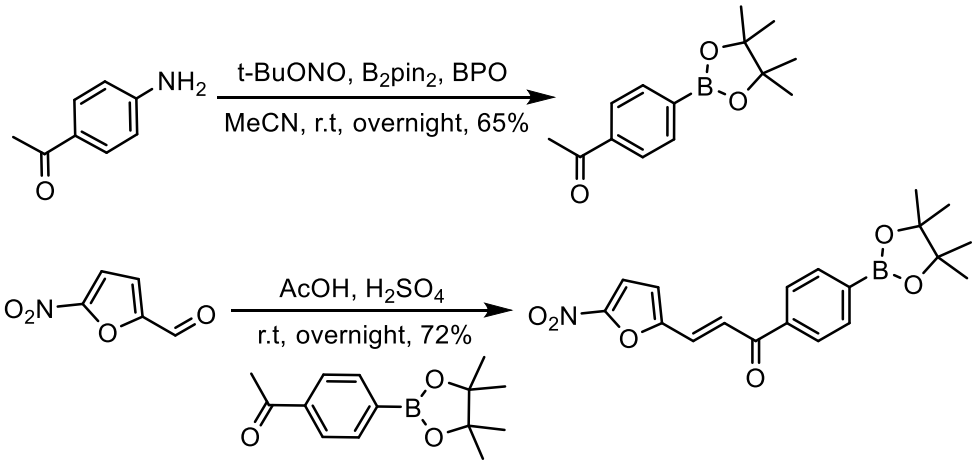

Source: Thesis author

First, a metal-free borylation reaction was carried out to obtain 4-acetylphenylboronic acid pinacol ester directly from 4-aminoacetophenone as described by Fanyang Mo [221]. The reaction between arylamines and tert-butyl nitrite (t-BuONO), an efficient diazotization reagent [222], generates the aryl diazonium salts *in situ*, which further reacts with B_2pin_2 to afford pinacol aryl boronates under open air. This borylation method has the following advantages: (1) the transformation is under metal-free conditions; (2) arylamines are inexpensive and ubiquitous starting materials; (3) the reaction has good tolerance to various functional groups, including electron-donating and electron-withdrawing groups, and also heterocyclic amines; (4) the reaction proceeds under very mild reaction conditions and is easy to operate [221, 223]. These reasons led us to use this specific procedure to obtain the [^{18}F]FNFP precursor.

Then, the Claisen–Schmidt condensation of 5-nitro-2-furaldehyde and 4-acetylphenylboronic acid pinacol ester under acidic conditions yielded (E)-(4-(3-(5-nitrofuran-2-yl)acryloyl)phenyl)boronic acid pinacol ester after flash chromatography in silica gel, following the same procedure described in the previous section for the synthesis of [^{19}F]FNFP.

The most used route to access pinacol aryl boronates is the Pd-catalyzed borylation of aryl halides (Miyaura borylation, scheme 21), or by Ir- or Rh-catalyzed direct borylation via aromatic C-H bond activation, with both methods being a more expensive alternative than the borylation of arylamines due to the high price or palladium catalysts, phosphines and complexes [221].

Scheme 21. Above, typical Pd-catalyzed Miyaura borylation reaction of aryl halides. Below, metal-free borylation process based on Sandmeyer-type transformation using arylamines, tert-butyl nitrite (t-BuONO) as diazotization agent and benzoyl peroxide (BPO) as radical initiator

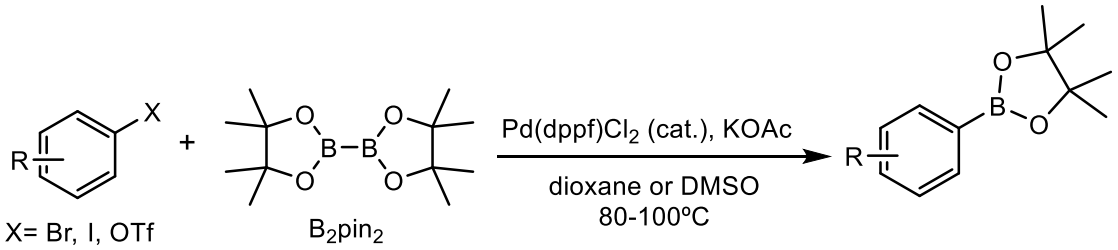

Source: Thesis author

5.2 Radiochemistry

5.2.1 Radiosynthesis of [^{18}F]FBNA and [^{18}F]FNFP

Different approaches were studied to manually synthetize [^{18}F]FBNA in a faster, easier and overall-optimized way than the previously reported one [40]. A precursor that could incorporate the [^{18}F] in just one step leading to the final product would be ideal, avoiding several different steps starting from a simple precursor, loss of activity due to [^{18}F] decay and exposition to radiation. In the [^{18}F]FBNA radiosynthesis reported, only the final step, meaning EDC-mediated

coupling of automated-synthesis product 4-[^{18}F]fluorobenzylamine ([^{18}F]FBA, Way and Wuest [180]) and 2-nitroimidazol-1-yl-acetic acid was performed manually (scheme 22). Due to some difficulties in our radiochemical facilities the automated synthesis of [^{18}F]FBA was impossible to be carried out, so a manual synthesis protocol was stablished in which [^{18}F]FBA was obtained with a radiochemical yield of 69% ± 12% (n = 5), within a total synthesis time of about 120 min.

In the automated procedure reported by Way and Wuest [180] and the one reported by our group describing the synthesis of [^{18}F]FBNA [40], [^{18}F]FBA was prepared with a radiochemical yield greater than 80% (decay-corrected) within 60min.Then the final coupling step with 2-nitroimidazol-1-yl-acetic acid, and HPLC purification took another 30-40 minutes. In our typical manual experiment for the synthesis of [^{18}F]FBNA, 20 GBq of cyclotron-produced [^{18}F] fluoride can be converted to 0.04GBq of [^{18}F]FBNA within a total synthesis time of about 180 min, which is more than one and a half half-lives of [^{18}F]. A solution to this long manual synthesis time had to be found.

Scheme 22. Synthesis of [^{18}F]FBNA reported using automated product [^{18}F]FBA [40].

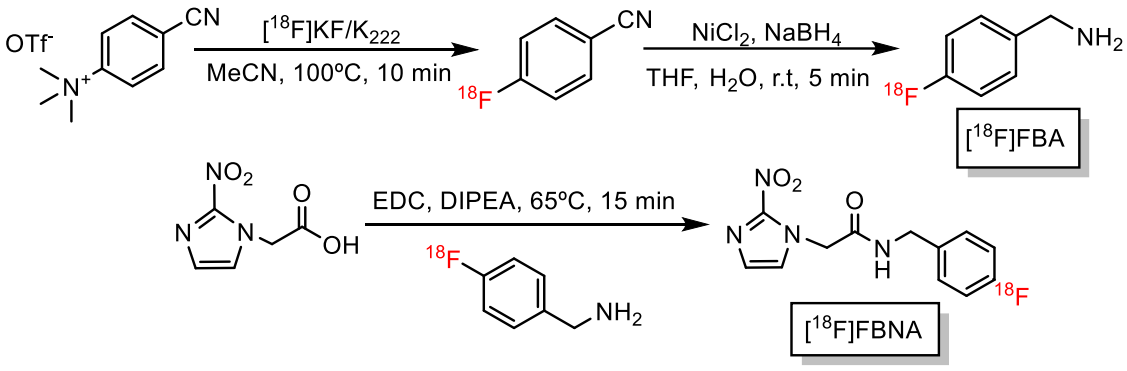

Copper-mediated radiofluorination of pinacol-derived aryl boronic esters was first introduced in Radiochemistry by the group of Gouverneur in 2014 [199] and then extended to aryl boronic acids by the Sanford and Scott group in 2015 [205], allowing the introduction of [^{18}F] in these precursors using Tetrakis(pyridine)copper(II) triflate [$Cu(OTf)_2(py)_4$] or copper triflate, $Cu(OTf)_2$ as catalysts. Late-stage [^{18}F]fluorination, introducing [^{18}F] as the last step in the

preparation of [^{18}F]FBNA would be the solution to our long [^{18}F]FBNA manual synthesis . For this purpose, a pinacol-derived aryl boronic ester precursor was prepared in order to obtain [^{18}F]FBNA in a one-step synthesis. A boronic acid pinacol-ester precursor would avoid going through all the necessary steps to obtain [^{18}F]FBA and then coupling step of this amine with 2-nitroimidazole-1-yl-acetic acid. The same approach was used for the synthesis of [^{18}F]FNFP.

Two different radiofluorination methods were evaluated to obtain both [^{18}F]FNFP and [^{18}F]FBNA, as described in the experimental section 4.2.2.1. Following the conventional radiosynthesis described in method 1 (scheme 23), [^{18}F]FBNA was obtained with a radiochemical yield (RCY) of 56±8% (n=5) after HPLC analysis of the crude reaction mixture using [$Cu(OTf)_2(py)_4$] as copper source. [^{19}F]FBNA “cold” standard was used as a reference for the comparison during quality control of the radioactive peak during the radio-HPLC run (Figure 29):

Figure 28. Free [^{18}F]-fluoride following the same run conditions as for [^{18}F]FNFP and [^{18}F]FBNA, retention time 2.72 min.

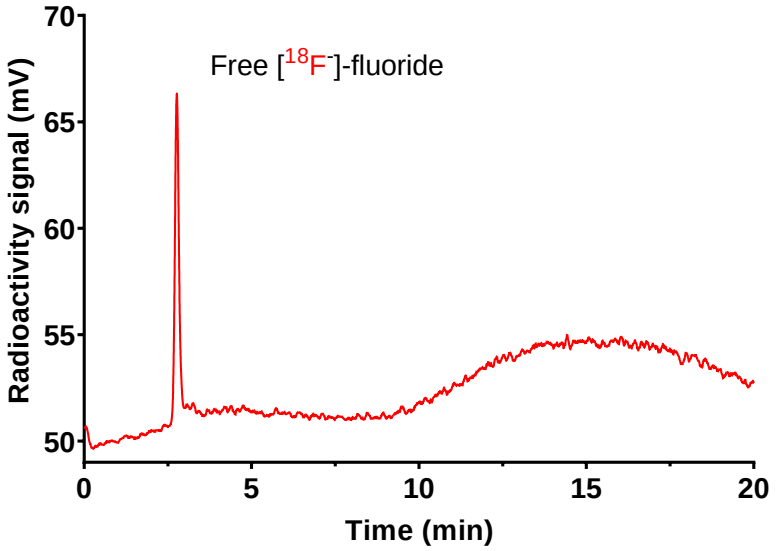

Source: Thesis author

Scheme 23. Radiosynthesis of [^{18}F]FBNA following method 1 as reported by Tredwell, Matthew et al.[199].

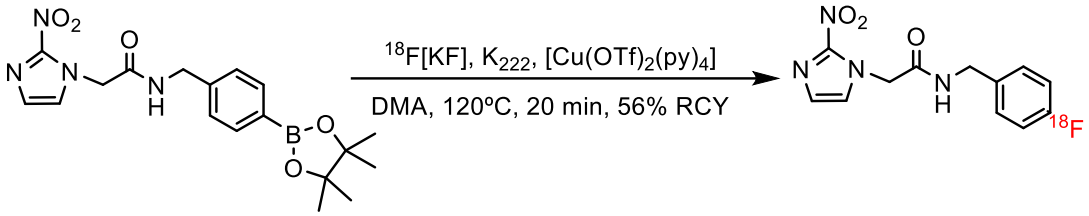

Figure 29. On the left, HPLC chromatogram of "cold" standard [^{19}F]FBNA at retention time 6,825 min, λ=300 nm. On the right, crude reaction mixture chromatogram showing free $^{18}F^-$ fluoride and ^{18}F-FBNA at 6.893 min retention time. Conditions: isocratic gradient, 70% A (0.1% TFA in H_2O), 30% B (MeCN) for 20 minutes, flow 1 mL/min.

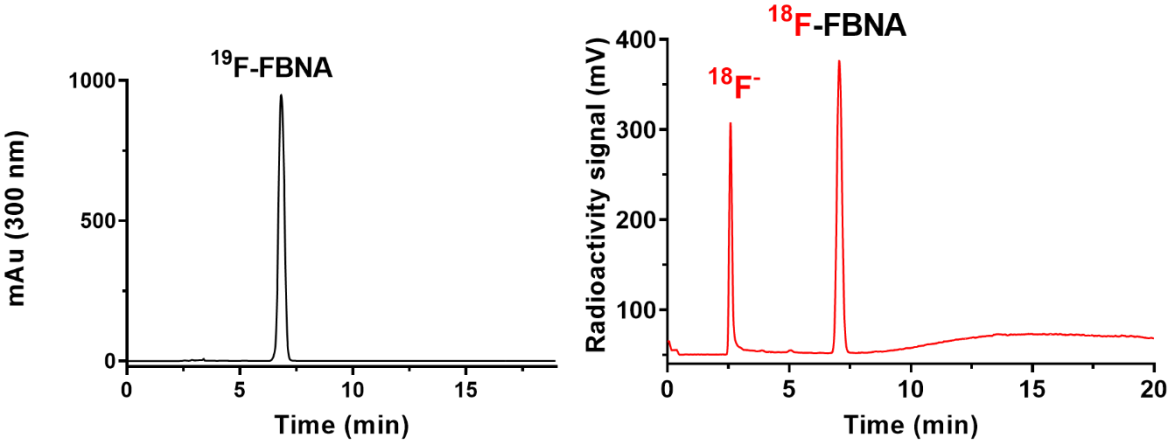

Source: Thesis author

Figure 30 shows the results for the synthesis of [^{18}F]FNFP following method 1:

Scheme 24. Radiosynthesis of [^{18}F]FNFP following method 1 as reported by Tredwell, Matthew et al.[199].

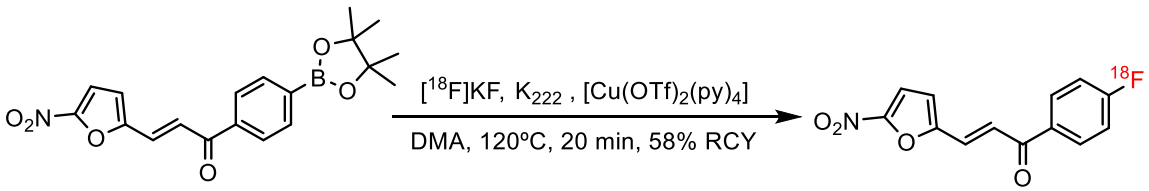

Source: Thesis author

Figure 30. On the left, HPLC chromatogram of "cold" standard [^{19}F]-FNFP at retention time 14,261 min, λ=350 nm. On the right, crude reaction mixture chromatogram showing free [^{18}F]$^-$ fluoride and [^{18}F]FNFP at 14,357 min retention time. Conditions: channel A (0.1% TFA in H_2O), B (MeCN); run 10-100% of B in 20 minutes, flow 1 mL/min.

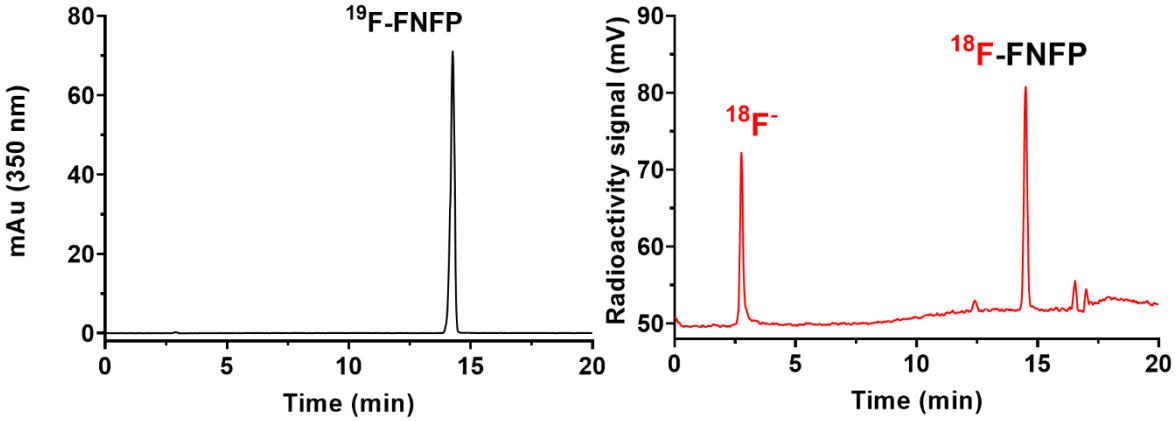

Source: Thesis author

Following the radiosynthesis procedure described in method 1 in the experimental section, [^{18}F]FNFP was obtained with a radiochemical yield of 58±7% (n=5) after HPLC analysis of the crude reaction mixture using [$Cu(OTf)_2(py)_4$] as copper source

The radiochemical yields for [^{18}F]FBNA and [^{18}F]FNFP obtained by radio-HPLC results of the crude reaction mixtures were in accordance with the ones reported in the original radiofluorination method of the Gouverneur group.[199] for pinacol-derived aryl boronic esters.

Some issues associated with the use of high quantities of base (K_2CO_3) in radiofluorination reactions have been reported in the past few years. Low radiochemical yields and the impossibility of using base-sensitive precursors limit the scope of this approach, especially for radiofluorination of aryl boronic esters and derivates because of the high temperatures (110-130ºC) necessary for this copper-mediated ^{18}F-fluorination to be carried out. Methods using other phase transfer catalysts (PTC) and milder bases, rather than the combination of K_{222}/K_2CO_3 are usually preferred.

Traditionally, for more than 40 years radiofluorination using non carried added ^{18}F-fluoride has relied on the use of the combination of K_{222}/K_2CO_3 in water/acetonitrile to elute the radionuclide from the anion exchange resin (QMA in most cases), followed by an azeotropic drying step to remove traces of water. This process is time consuming; some activity is lost due to radioactive decay and results in part of the $^{18}F^-$adhering in the glass vessel walls during the drying process, so a procedure in which the azeotropic drying step could be eliminated would be ideal. In this regard, Lahdenpohja, S.O., Rajala, N.A., Rajander, J. et al in 2019 developed an azeotropic drying-free [^{18}F]-labelling method to improve the copper-mediated radiofluorination of aryl boronic acids and pinacol esters to achieve wide substrate scope with good radiochemical yields and short synthesis time [210]. We tried this approach for the synthesis of both [^{18}F]FBNA and [^{18}F]FNFP, described in the experimental section as method 2.

First, as pointed out by Lahdenpohja, S.O., Rajala, N.A., Rajander, J. et al [210] we evaluated the percentage of [$^{18}F^-$]-fluoride recovered from the QMA after the elution step with $Cu(OTf)_2$ in DMA, obtaining an elution efficiency of 66±4% (n=6), a result that matches the ones reported by the authors.

Regarding the synthesis of the radiotracers, figure 31 shows the results for radio-HPLC of a crude-reaction-mixture sample for the synthesis of [^{18}F]FBNA.

Scheme 25. Radiosynthesis of [^{18}F]FBNA following method 2 as reported by Lahdenpohja, S.O., Rajala, N.A., Rajander, J. et al [210].

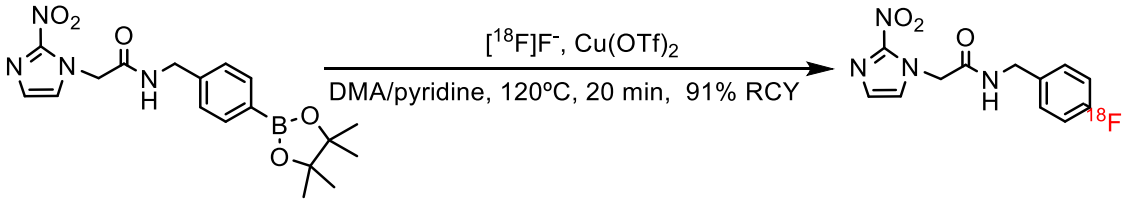

Source: Thesis author

Following the procedure described in method 2 (scheme 25), [^{18}F]FBNA was obtained with a radiochemical yield (RCY) of 91±3% (n=5) after radio-HPLC analysis of the crude reaction mixture, using [^{19}F]FBNA “cold” standard as reference.

Figure 31. On the left, HPLC chromatogram of "cold" standard [^{19}F]FBNA at retention time 6,825 min, λ=300 nm. On the right, crude reaction mixture chromatogram showing free [^{18}F]$^{-}$ fluoride and [^{18}F]FBNA at 6.901 min retention time. Conditions: isocratic gradient, 70% A (0.1% TFA in H_2O), 30% B (MeCN) for 20 minutes, flow 1 mL/min.

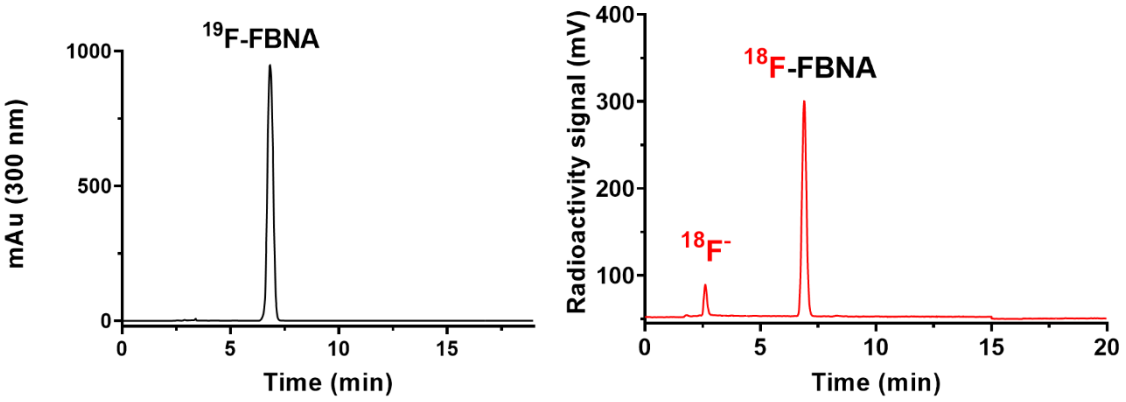

Source: Thesis author

In case of the synthesis of [^{18}F]FNFP following method 2, figure 32 shows the radio-HPLC results of a crude reaction mixture run.

Scheme 26. Synthesis of [^{18}F]FNFP according to the method reported by Lahdenpohja, S.O., Rajala, N.A., Rajander, J. et al. [210].

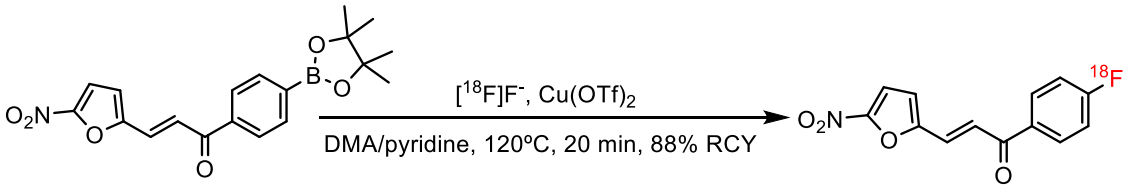

Source: Thesis author

[^{18}F]FNFP was obtained with a radiochemical yield (RCY) of 88±4% (n=5) after radio-HPLC analysis of the crude reaction mixture, using [^{19}F]FNFP "cold" standard as reference (figure 32).

Comparing both methods 1 and 2 previously described here for the synthesis of both radiotracers [^{18}F]FBNA and [^{18}F]FNFP, the results, considering radiochemical yields, were overwhelmingly better for method 2.

Figure 32. On the left, HPLC chromatogram of "cold" standard [^{19}F]FNFP at retention time 14,261 min, λ=350 nm. On the right, crude reaction mixture chromatogram showing free [^{18}F]$^-$ fluoride and [^{18}F]FNFP at 14,388 min retention time. Conditions: channel A (0.1% TFA in H_2O), B (MeCN); run 10-100% of B in 20 minutes, flow 1 mL/min.

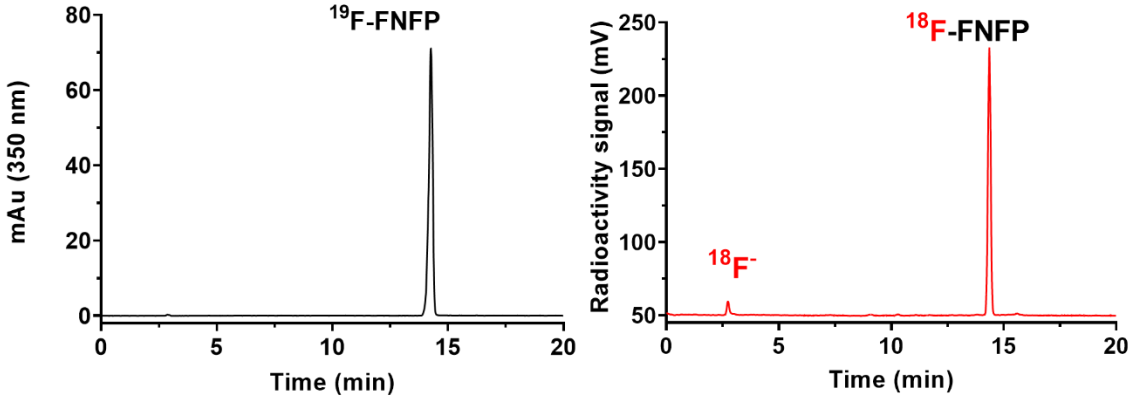

The main reason behind the great difference in radiochemical yields comparing method 1 and method 2 (around 30%) for the synthesis of both radiotracers might be the harsh basic conditions created by the potassium carbonate (20 μmol) used for the elution of the [^{18}F$^-$]-fluoride from the QMA, that alongside the high temperatures during the nucleophilic aromatic substitution might result in side reactions and partial decomposition of the precursors. Besides method 2 being a faster approach to obtain [^{18}F]FBNA and [^{18}F]FNFP because of the elimination of the azeotropic drying step, only copper II triflate in dimethyl acetamide was used to elute the [^{18}F$^-$]-fluoride from the anion exchange resin, turning this approach in a "milder" procedure and of course after the elution step, the [^{18}F$^-$] was ready to use in subsequent labelling reaction without the use of additional reagents or any other manipulations. Method 2 was then used as the standard procedure for obtaining both radiotracers.

After the synthesis following method 2, the respective reaction mixtures containing [^{18}F]FNFP and [^{18}F]FBNA were diluted with water and passed through a pre-conditioned C18 cartridge to remove impurities and unreacted

[$^{18}F^-$]-fluoride. Following elution of the radiotracers from the respective cartridges, semipreparative HPLC purification afforded >99% radiochemically pure [^{18}F]FBNA and [^{18}F]FNFP, with a total synthesis time of 70 and 85 minutes, respectively (Figure 33).

Figure 33. [^{18}F]FNFP (left, retention time 14,261 min) and [^{18}F]FBNA (right, retention time 7.014 min) after semipreparative HPLC purification using the same conditions previously described for each radiotracer.

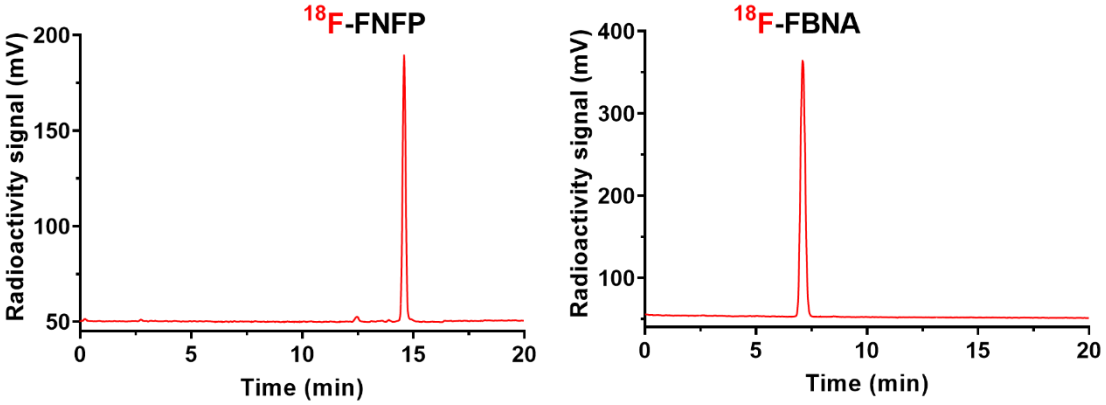

Source: Thesis author

The final radiochemical yields, decay corrected, were 39,1±5% (n=3) for [^{18}F]FBNA and 38,4±3% for [^{18}F]FNFP (n=3). Comparing these results for [^{18}F]FBNA with the ones already reported [40], we obtained here [^{18}F]FBNA in a shorter synthesis time (70 vs 100 min), with a slightly lower overall radiochemical yield (39,1±5% vs 47.4±5.3%).

5.2.2 Determination of molar activity

[^{18}F]FNFP and [^{18}F]FBNA molar activities were assessed by the calibration curves displayed in Table 3 and Figure 34 for the former, and Table 4 and Figure 35 for the latter:

Table 3. Standard curve for assessing [^{18}F]FNFP molar activity using a standard [^{19}F]-FNFP solution.

[^{19}F]FNFP (10^{-4} µmol)	UV area (mAU, 350 nm)
1	55,19128
2	76,4968
4	134,352
8	301,418
16	666,4318
24	1254,27271
30	1587,40125
40	2113,18164

Source: Thesis author

Figure 34. Standard curve data for [^{19}F]FNFP to determine [^{18}F]FNFP molar activity.

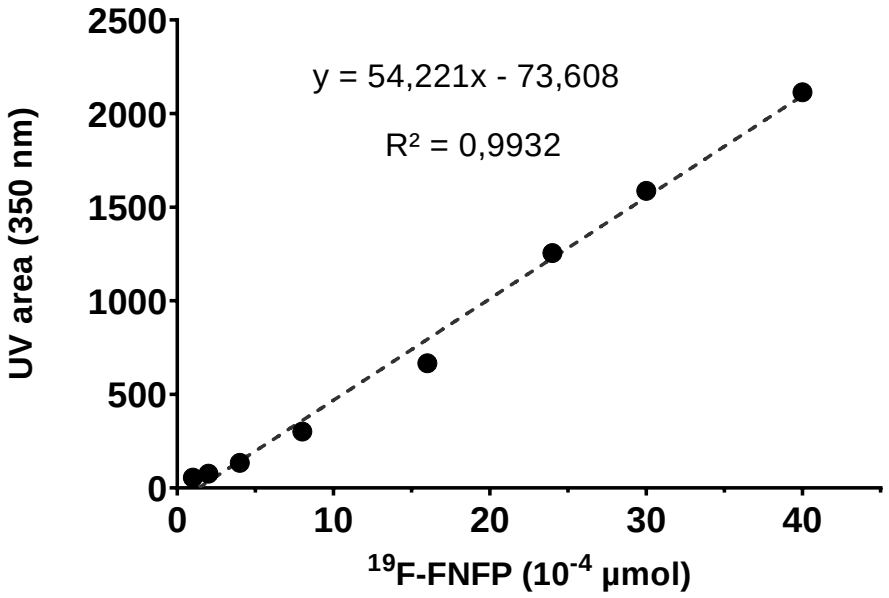

Source: Thesis author

Table 3. Standard curve for assessing [^{18}F]FBNA molar activity using a standard [^{19}F]FBNA solution.

[^{19}F]FBNA (10^{-3} µmol)	UV area (mAU, 300 nm)
0	0
2	76,4968
4,37	73,8691
8,74	139,4975
17,48	263,2771
30	480,8431
43,7	806,2787
50	950,6312

Source: Thesis author

Figure 35. Standard curve data for [^{19}F]FBNA to determine [^{18}F]FBNA molar activity.

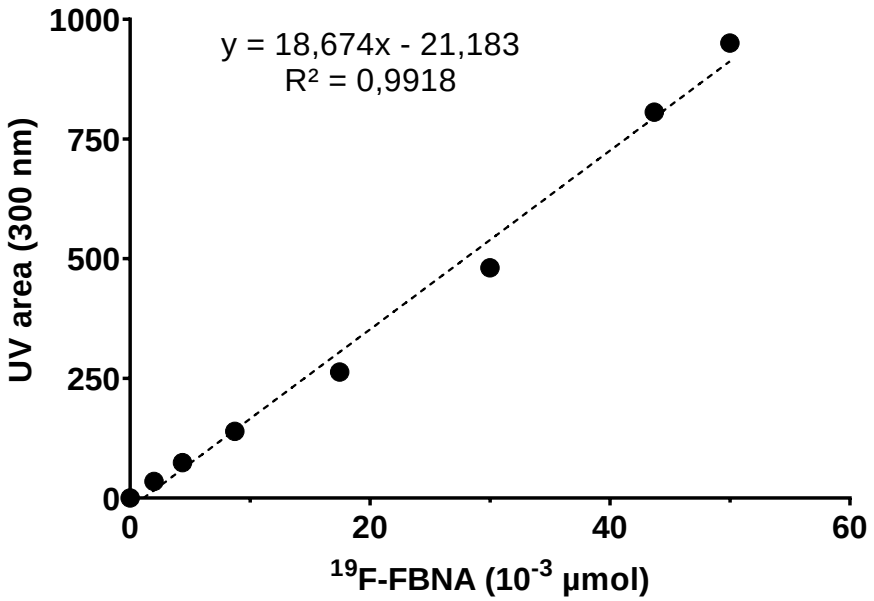

Source: Thesis author

20 µCi (0.74 MBq) of each radiotracer was injected into the HPLC, and the results indicated that [^{18}F]FBNA was obtained with a molar activity of 43,02 GBq/µmol and 41.56 GBq/µmol for [^{18}F]FNFP. In case of the former, this specific activity is well-correlated with the one previously reported by our group [40] (>40 GBq/µmol).

5.2.3 Stability of [^{18}F]FNFP in PBS and serum

The characterization of novel radiotracers toward their metabolic stability is an essential part of their development. Therefore, assessing the stability of these new labeled compounds is one of the most essential parameters to determine whether they have the potential to be used for *in vivo* applications or not. In this work, the stability of the new radiopharmaceutical [^{18}F]FNFP in 0.1 mol/L PBS at pH=7.2 and in serum was evaluated for a period of up to 6 hours. Aliquots were taken immediately after the synthesis, 1, 3 and 6 hours after it, and the radiochemical purity of the compound was assessed by HPLC following the same conditions as described earlier for its quality control.

Figure 36. Radioactivity profile obtained by radio-HPLC of the stability of [^{18}F]FNFP after 6 hours in 0.1 mol/L PBS at pH=7.2 (right bottom) and in serum (left bottom). Above, [^{18}F]FNFP at the beginning of the stability test.

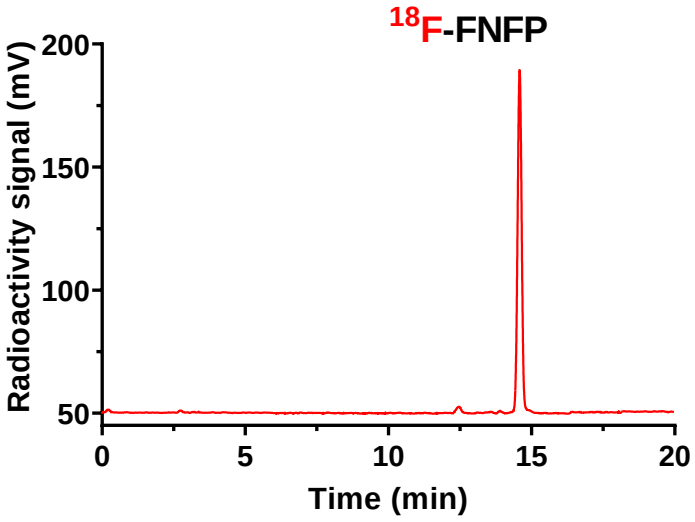

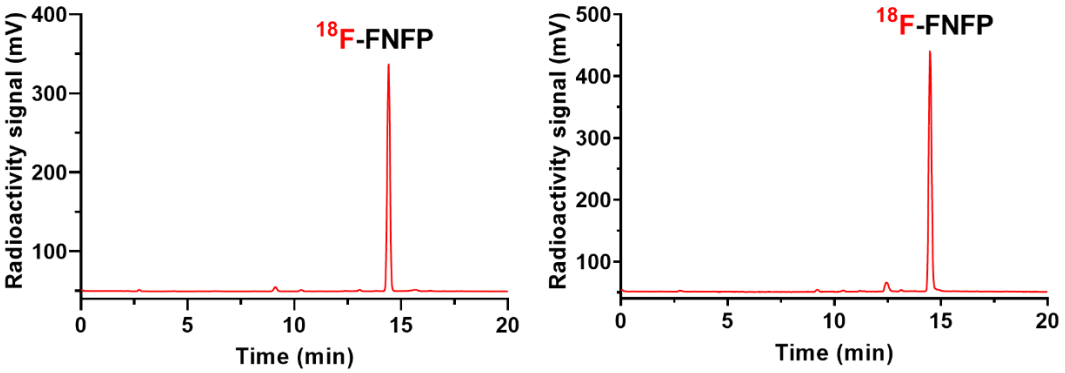

.**Source:** These author

As demonstrated in Figure 36, no significant metabolites derived from [^{18}F]FNFP were observed after 6h of incubation either in PBS or serum.

5.2.4 [^{18}F]FNFP lipophilicity measurements

The logarithm of the partition coefficient P ($log_{10}P$) is a critical measure that not only determines how well a drug will be absorbed, transported, and distributed, but also dictates how a drug should be formulated and dosed. For example, a drug with low aqueous solubility and high lipophilicity (high positive $log_{10}P$) will be compromised in bioavailability, sequestered in fatty tissues and therefore its plasma levels cannot be maintained [224].

$log_{10}P$ is a constant and is a negative value for hydrophilic compounds, a positive value for lipophilic compounds, and zero (0) value for compounds which partition equally between lipid and aqueous phases. For example, if $log_{10}P = 1$ it means that the partitioning of the compound is 10 times more in lipid/organic solvent phase compared to aqueous phase [224]. In short, lipophilicity needs to be high enough to enable diffusion across cellular membranes to the site of metabolism (~ ≥0.1), but low enough (~ ≤2) to assure rapid systemic elimination and, hence, convenient imaging times (within 2 h) [212]. The most important limitation of [^{18}F]FMISO is its high lipophilicity, which causes slow tracer accumulation, slow plasma clearance, and low tumor-to-background contrast [141].

The [^{18}F]FNFP partition coefficient calculated according to the methodology described in the experimental section was $log_{10}P=1.05 \pm 0.06$ (n=7), that is basically the same as that of ^{18}F-FBNA ($log_{10}P=1.05$) [40] and

lower than that of [^{18}F]FMISO ($log_{10}P$=2.6) [225], meaning that [^{18}F]FNFP is less lipophilic (more hydrophilic) than the latter, which theoretically should result in improved pharmacokinetic properties.

6 BIOLOGICAL STUDIES

6.1 Assessment of [^{18}F]FNFP uptake *in vivo* by µPET imaging

By means of the µPET/CT equipment, the specific uptake of the new radiotracer [^{18}F]FNFP under hypoxic conditions was investigated in the gastric cancer line MKN-45 previously inoculated into Balb/c nude mice. Dynamic imaging studies were performed using [^{18}F]FNFP by injecting 20 MBq of the radiotracer intravenously into Balb/c nude mice (n=3) containing the MKN-45 tumor measuring approximately 300 mm^3. The animals were placed in the scanning chamber immediately after injection. PET images were acquired for a total time of 180 min. Figure 37 shows representative PET/CT images of [^{18}F]FNFP taken between 5 minutes and 3 hours after injection in different planes.

No uptake was seen in the tumor up to 3 hours after administration of [^{18}F]FNFP. The radiotracer is rapidly metabolized after being injected; in image 1, [^{18}F]FNFP has a high uptake in the liver, kidneys, lungs, and brain, and after 30 minutes bladder and intestines (image 2), showing that [^{18}F]FNFP has a nimble metabolism and hepato-biliary-intestinal-renal clearance.

After 1 hour (image 3) all the injected radiotracer had already been metabolized, with no signs of tumor uptake. After 3 hours (image 4) the same results were seen.

Figure 37. µPET/CT images of [^{18}F]FNFP uptake using a gastric cancer tumor model up to 3 hours after injection of the tracer. A) transversal plane highlighting the tumor; B) coronal plane; C) sagittal plane; D) sagittal Maximum Intensity Projection (MIP) image. Image 1, (above on the left) 5 minutes after injection. Image 2, (above on the right) 30 minutes after injection. Image 3, (down, on the left) one hour after injection. Image 4 (down on the right) 3 hours after injection. 20 MBq of radiotracer were injected intravenously into Balb/c nude mice previously inoculated with MKN-45 tumor cells. Mice were placed in the µPET/CT equipment where a PET image was

acquired for 180 minutes after administration, followed by CT image acquisition (35 kV, 400 µA). The figure is representative of n=3.

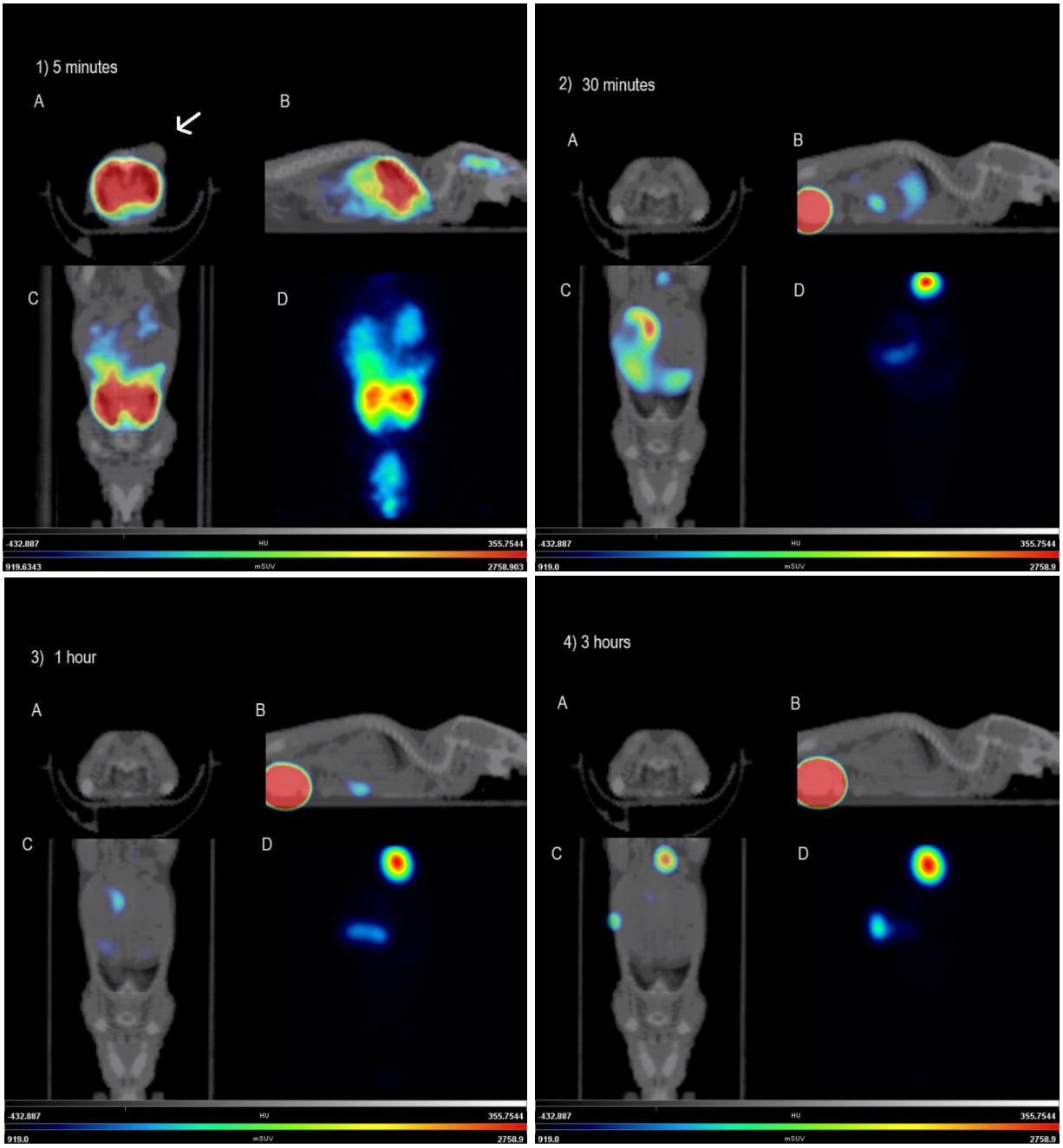

Source: Thesis author

Figure 38 shows how [^{18}F]FNFP distributes during the whole study in tumor and muscle. Comparing maximum SUVs, it can be noted that tumor/muscle relation is always greater than 1, but the radiotracer has its maximum uptake values in the tumor around 10-15 minutes after injection (which is also very low), something that was not expected considering the previously calculated $\log_{10}P$ (1.05, same as [^{18}F]FBNA).

Figure 38. Dynamic representation of [^{18}F]FNFP uptake in tumor (light blue) and muscle (green) vs maximum SUV during 180 min of μPET/CT imaging.

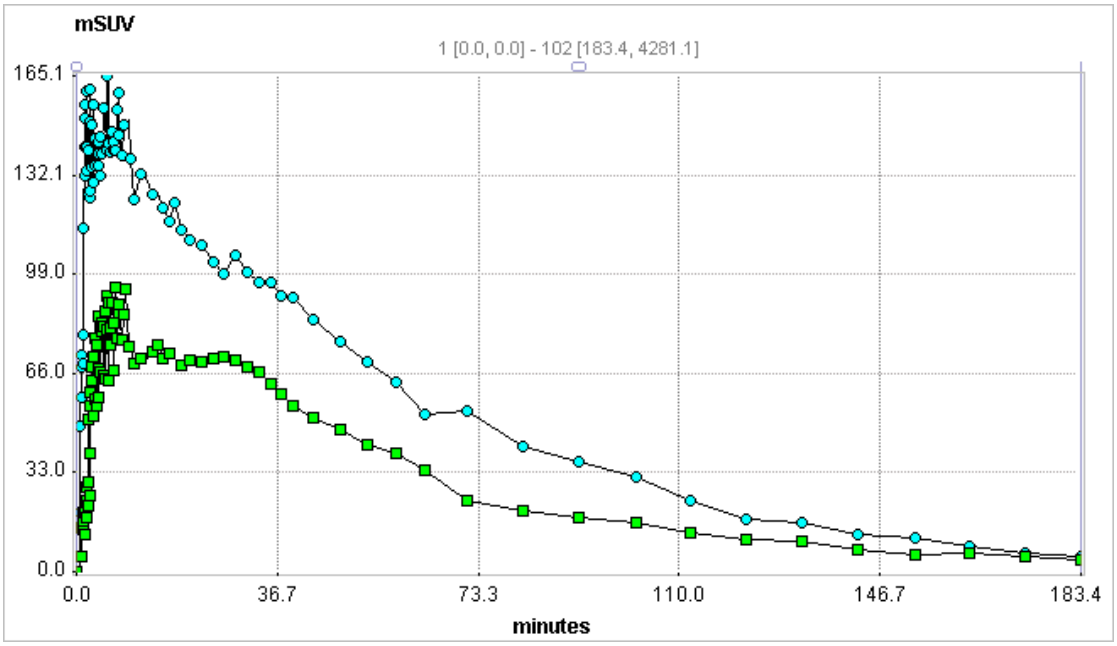

:**Source:** Thesis author

Two similar representations were then plotted, now including the brain (figure 39), since after 5 min and up to 30 minutes of study this organ had a high uptake of the radiotracer, and the bladder (figure 40). Figure 39 shows that between 5-15 minutes the radiotracer's uptake in the brain has its maximum value, and compared to that of tumor is unexpectedly great.

When designing our molecule ([^{18}F]FNFP) for detection of hypoxic regions in the tumor microenvironment, the most important parameter was maintaining the nitroaromatic moiety responsible for the selective tracer's accumulation under hypoxic conditions. Then the side chain was constructed according to other properties such as improvement of electron affinity and pharmacokinetic properties ($\log_{10}$P).

Figure 39. Dynamic representation of [^{18}F]FNFP uptake in tumor (light blue), muscle (green) and brain (dark blue) vs maximum SUV during 180 min of μPET/CT imaging.

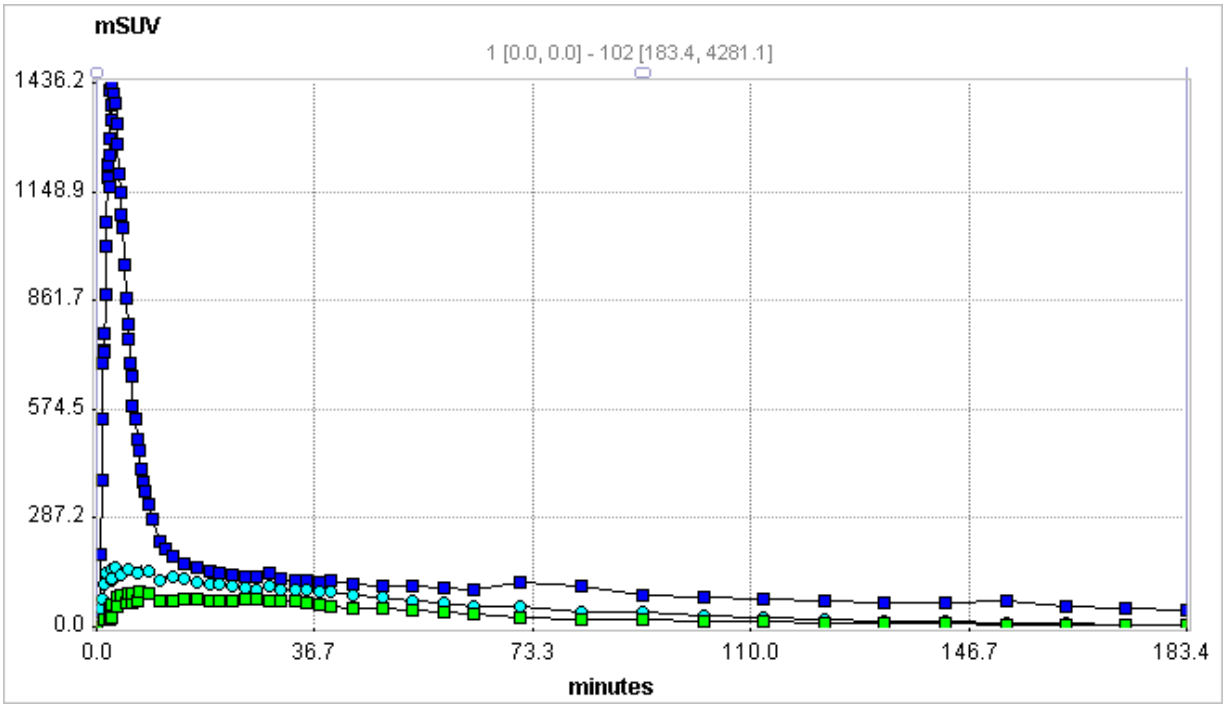

Source: Thesis author

Figure 40. Dynamic representation of [^{18}F]FNFP uptake in muscle (green), brain (dark blue) and bladder (fuchsia) vs maximum SUV during 180 min of μPET/CT.

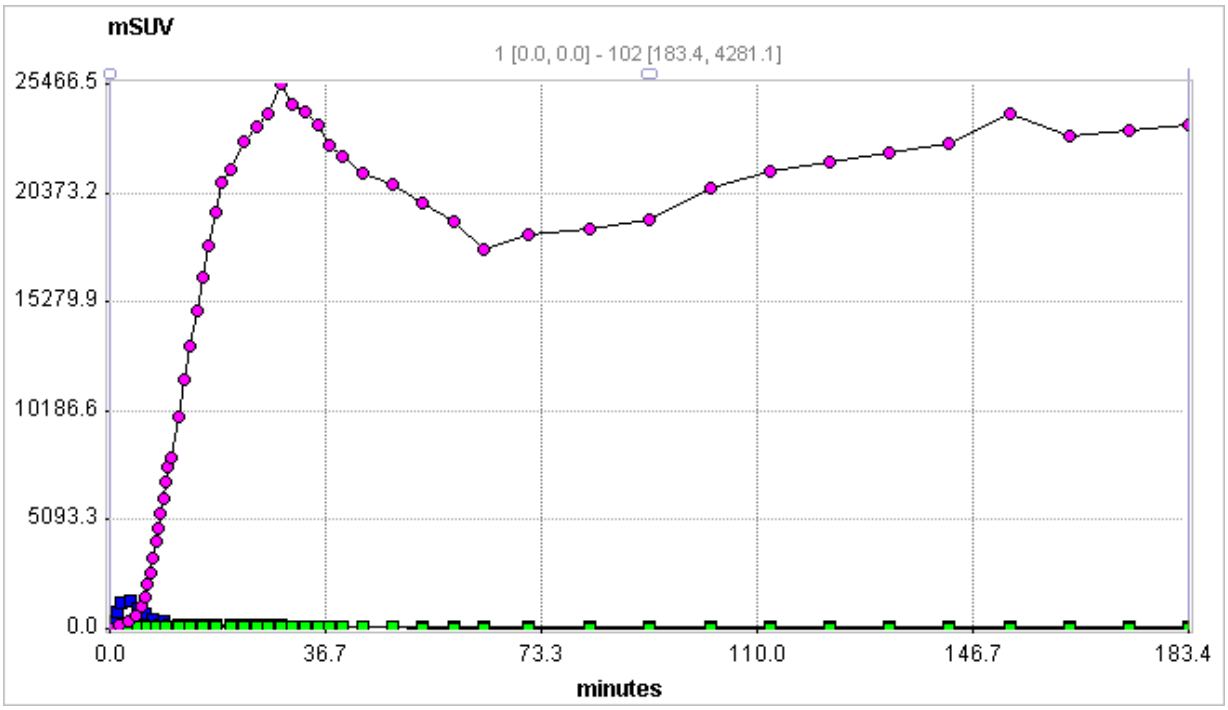

Source: Thesis author

Apparently [^{18}F]FNFP enters the brain via passive diffusion, due to its low molecular weight (261,2 g/mol) and moderate lipophilicity ($log_{10}P$=1.05), according to radiopharmaceuticals characteristics for entering the blood-brain barrier discussed by Uzuegbunam, Bright Chukwunwike et al. [226].

In a previous work developed by our group [40], N-(4-[^{18}F]fluorobenzyl)-2-(2-nitro-1H-imidazol-1-yl)acetamide [^{18}F]FNBA was synthesized and *in vitro* and *in vivo* studies proved that this novel radiopharmaceutical could become a radioligand for imaging hypoxia. Dynamic μPET/CT images in MKN-45-tumor-bearing mice showed that its uptake in the tumor begins to occur 30 min after its injection, reaching its highest uptake point 1 hour after the tracer's administration (Figure 41, taken from [227]). As for [^{18}F]FNFP and [^{18}F]FNBA pharmacokinetic properties, it was expected a similar uptake time in the tumor due to an equal partition coefficient and mechanism of action of both nitroaromatic moieties (5-nitrofuran for [^{18}F]FNFP and 2-nitroimidazole for [^{18}F]FNBA).

Figure 41. Coronal μPET/CT imaging of [^{18}F]FBNA uptake using a gastric cancer tumor model. The radiopharmaceuticals (at a dose of 20 MBq) were injected intravenously into Balb/c nude mice previously inoculated with MKN-45 tumor cells. The animals were placed in the μPET/CT equipment where a PET image was acquired at 10, 30, 60, 120, and 180 minutes after administration of the radiopharmaceuticals, followed by CT image acquisition (35 kV, 400 μA). The figure is representative of n=3. Taken from [227].

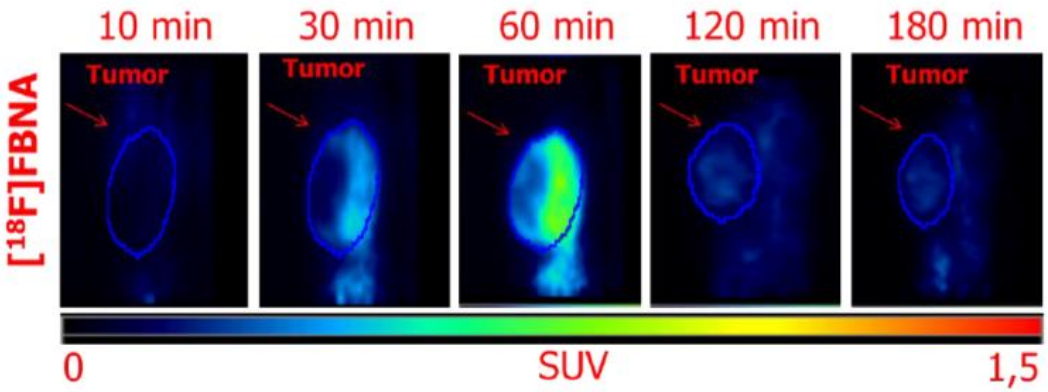

Chalcone and its derivates (Figure 42), α,β-unsaturated precursors of flavonoid and isoflavonoid-based compounds, either natural or synthetic exhibit various biological activities, such as anti-inflammatory, analgesic, antioxidant, antibacterial, antifungal, anti-tuberculosis, antimalarial, antiviral, and antitumor [228]. This conjugated structure is characterized by a high delocalization of the electrons and a low redox potential that provide remarkable chances of undergoing electron transfer reactions [229]. Presence of a α,β-unsaturated carbonyl functional group, which acts as a potential Michael acceptor, allows the chalcone molecule to interact with sulfhydryl of cysteine residue or other thiol groups (Figure 42). This interaction is believed to be important for their biological activities [229, 230].

Figure 42. Above, Chalcone [(E)-1,3-diphenyl-2-propene-1-one] (all R=H) and derivates, and the cis and trans (thermodynamically more stable) forms. Below a typical reaction of chalcone functioning as Michael acceptor with cysteine. Other derivates could be also obtained by replacing the benzene ring with other heterocyclic rings.

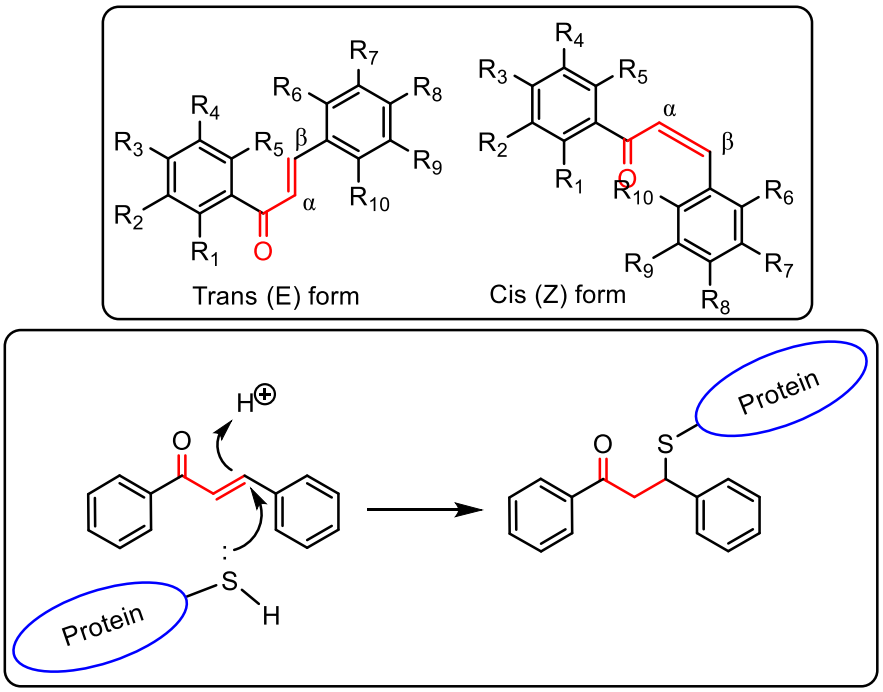

Source: Thesis author

Radiolabeled chalcone derivates have been recently used as β-amyloid plaques imaging agents in Alzheimer's disease (AD) [231, 232]. This is due to the structural similarity of chalcones with curcumin (Figure 43), which has been

reported to have sufficient brain permeability and favorable binding affinity to β-amyloid plaques after iv administration in APPsw transgenic mice [233, 234]. It has been shown that curcumin inhibits the formation and promotes the disaggregation of Aβ-amyloid plaques. Moreover, it attenuates the hyper-phosphorylation of tau protein and enhances its clearance. The applications of radiolabeled curcumin and curcuminoids in medicinal chemistry has been recently reviewed [235, 236] but, despite a manifested affinity for amyloid plaques *in vitro*, none of the radiolabeled probes proved to be a suitable tool for the imaging of AD *in vivo*. The main reason for this failure is likely due to either the little stability of the curcumin backbone in physiological media and to the inability of the radiolabeled probes to cross the blood-brain barrier [232].

Figure 43. Chemical structures of curcumin and chalcone, natural active compounds against several pathogens.

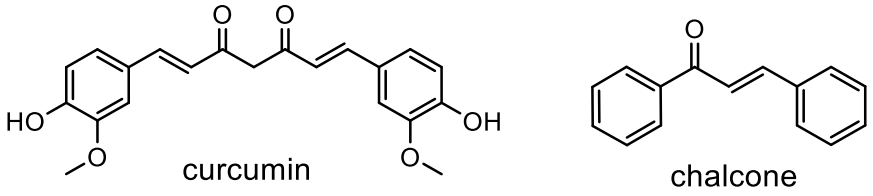

Source: Thesis author

There are several property criteria that should be met for a candidate radioligand to successfully be used as a brain-image radiotracer *in vivo*. Of course, it needs to effectively bind to its target, but also favorable pharmacokinetics with fast washout from normal brain is highly desirable in providing specific PET imaging signals [226, 237], labeled with a proper radioisotope (generally ^{18}F or ^{11}C). For example, as highlighted by Zeng, F., & Goodman, M. M., high initial brain uptake (>5 % dose/g at 2 min post iv injection) followed by a fast washout from the normal brain (< 2% dose/g at 30 min) is a desirable property for amyloid (Aβ) plaques-targeting imaging agents [237].

These crucial characteristics are met by radiolabeled chalcone derivates, which have been radiolabeled with $^{124,125}I$, ^{99m}Tc, ^{68}Ga, ^{11}C and ^{18}F for detection of Aβ-amyloid plaques [232]. For example, recently Allott et al. [238] reported the synthesis of a fluorine [^{18}F]-labeled chalcone derivative based as a dual modality imaging agent (PET and fluorescence) for detecting glycogen in cancer

tissues (Figure 44). PET imaging in normal mice and metabolite analysis suggested favorable hepatobiliary intestinal elimination and fast metabolism of the radiolabeled chalcone [238].

Figure 44. ^{18}F[5], dual modality fluorescence/PET tracer obtained by Allott et al. [238].

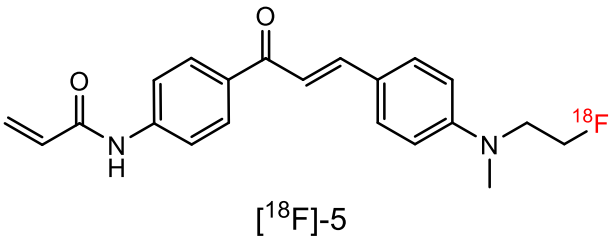

Source: Thesis author

Zeng, F., & Goodman, M. M [237] came up with the conclusion that the mutual structural elements of most potent and selective β-amyloid plaques imaging agents are conjugated heterocyclic rings (such as the ones present in chalcones) and a secondary amine [237]. For example, a few of these compounds present a conjugated bridge joining two heterocycles, and some of them have undergone clinical trials. [^{18}F]AV-45, commercially known as Amyvid^{TM}, became the first radioactive diagnostic agent recently approved by FDA for PET imaging of β-amyloid neuritic plaques in the brain [237] (Figure 45).

Figure 45. Chemical structures of some of the PET imaging agents for β-amyloid plaques tested in humans and [^{18}F]FNFP. In blue the conjugated bridges are highlighted. Adapted from Zeng, F., & Goodman, M. M. [237].

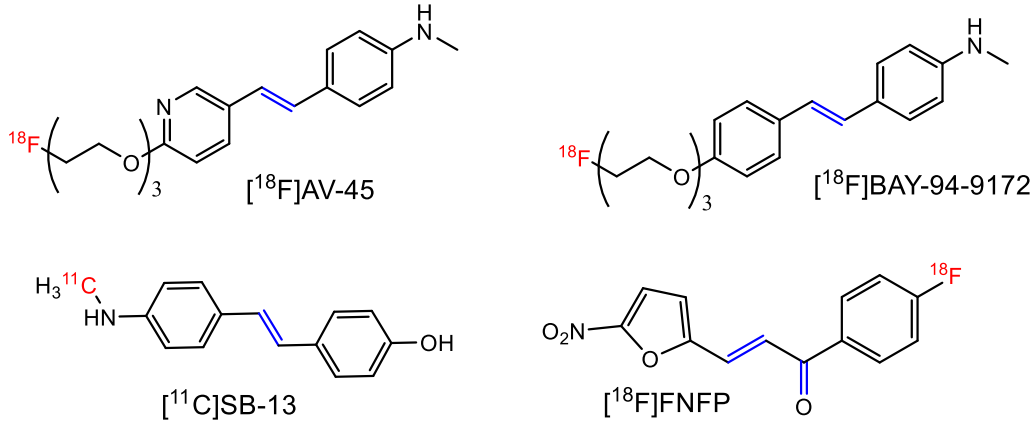

Source: Thesis author

[^{18}F]FNFP, as it can be noted from the structures presented above, is a chalcone derivate in which a phenyl ring was substituted by the nitrofuran moiety. It possesses a conjugated bridge joining two heterocycles, and just like other chalcone-based radiotracers, it has a rapid metabolism and washout in the brain. The results obtained here are in the dynamic PET imaging are not different from the ones reported for similar-structure compounds, but at least we expected different results regarding the [^{18}F]FNFP uptake under hypoxic conditions.

6.2 *Ex vivo* biodistribution studies in tumor-bearing mice

E*x vivo* biodistribution studies were then performed in MKN45 tumor-bearing mice to quantify tissue uptake of [^{18}F]FNFP 1 and 3 hours after injection of the radiotracer (Figure 46).

Figure 46 – *Ex vivo* biodistribution of [^{18}F]FNFP in MKN45 gastric tumor-bearing mice 1 (green) and 3 hours (blue) of intravenous injection. 20 MBq of the radiotracer were injected intravenously into MKN-45-gastric-tumor-bearing Balb/c nude mice, and 1 and 3 hours after injection the animals were euthanized, and the organs of interest were collected for weighing and activity counting in a gamma well counter. The graph shows the mean value ±SD of %DI/g of n = 4. Data were analyzed following one-way ANOVA Sidak's multiple comparisons test * p<0.05; ** p<0.01; *** p<0.001; ***** p<0.0001.

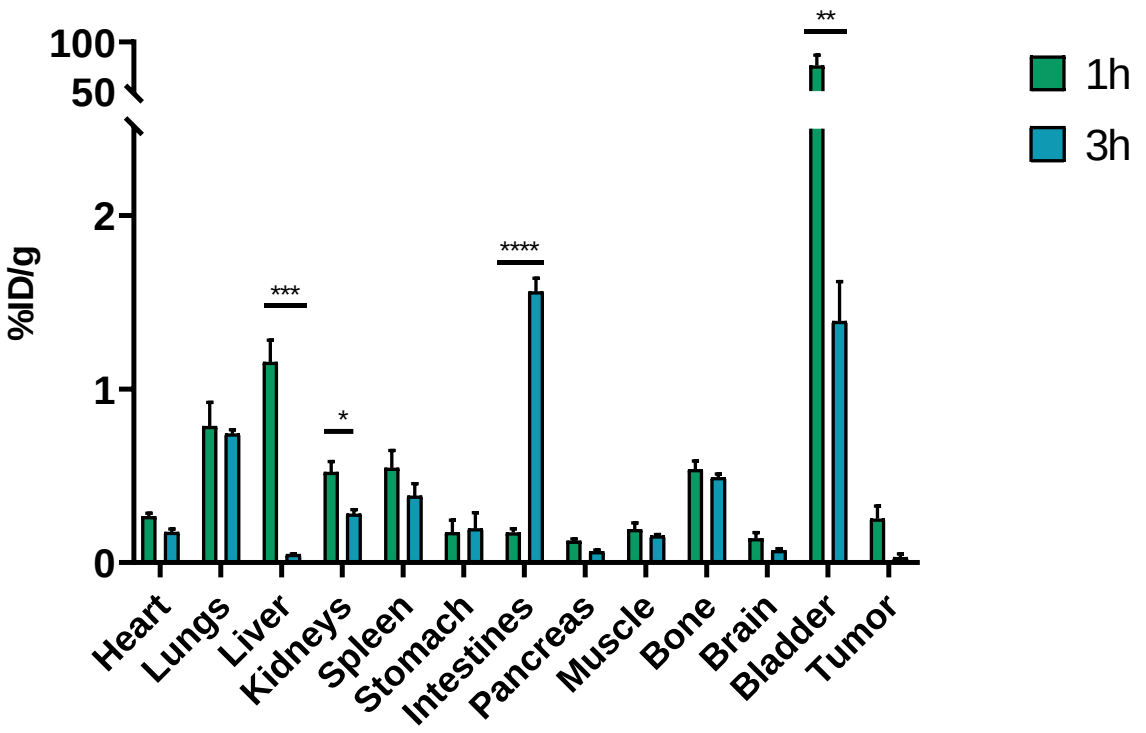

Source: Thesis author

Similar results to the ones from the PET/CT images were expected, and effectively no uptake was found in the tumor of the studied groups. As concluded in the images study, [^{18}F]FNFP has a hepato-biliary-intestinal clearance, which was confirmed in the *ex-vivo* study considering how the uptake in the liver diminishes from 1 to 3h, and it increases within the times studied in the intestines. Moreover, bladder uptake presents the biggest difference in uptake from 1 to 3 hours confirming the results from the PET/CT dynamic study.

Table 4. %DI/g values of organs collected in the *ex-vivo* biodistribution of mice bearing MKN-45 gastric tumor after intravenous injection of [^{18}F]FNFP. Data represent the mean value ±SD of %DI/g of n = 4.

	[^{18}F]FNFP (% ID/g)	
Organ	1h	3h
Heart	0,27±0,03	0,18±0,04
Lungs	0,79±0,24	0,74±0,05
Liver	1,16±0,22	0,05±0,02

Kidneys	0,52±0,12	0,28±0,05
Spleen	0,55±0,20	0,38±0,22
Stomach	0,18±0,14	0,2±0,08
Intestines	0,17±0,04	1,56±0,7
Pancreas	0,13±0,02	0,06±0,01
Muscle	0,2±0,08	0,15±0,08
Bone	0,54±0,1	0,49±0,1
Brain	0,14±0,07	0,07±0,011
Bladder	75,99 ±1,8	1,39±0,82
Tumor	0,25±0,15	0,03±0,024

It should be considered that the dynamic PET/CT image study was performed during the same day as the *ex-vivo* studies, so no previous information of the tracer's distribution in mice was known. Shorter times could have been selected as ideals for ex-vivo quantification of [^{18}F]FNFP had the information from its rapid metabolism (and apparently no tumor uptake) been known (for example, 15 and 30 minutes after tracer's administration).

[^{18}F]FNFP has a very similar, almost equal $\log_{10}$P as that of [^{18}F]FBNA (approximately 1,05) and a slightly lower molecular weight (261,21 vs 278,24 FBNA). The mechanism through which [^{18}F]FBNA, being a 2-nitroimidazole derivate, accumulates under hypoxic conditions is the same as that of nitroaromatic compounds in general: these compounds are taken up by cells via diffusion and chemically reduced by various cellular nitroreductases, generating nitro-radical anions.

When cells are well-oxygenated, those anions react with intra-cellular O_2 and revert to the parent molecule, which thereafter freely diffuses out of the cell. Under hypoxic conditions, the reduced nitroaromatic compound undergoes further reduction to generate reactive hydroxylamine that binds to cellular macromolecules (such as DNA, proteins, and glutathione), thereby trapping the drug inside hypoxic cells. It was expected some accumulation of [^{18}F]FNFP in

the tumors, but the result showed that perhaps due to its rapid metabolism the tracer did not have a chance to actually get through tumor tissue.

We did not use another radiotracer, such as [^{18}F]FBNA, for example, as a prove that at least those animals used for dynamic imaging studies were carrying tumors with hypoxic conditions, but none of them actually showed any sign of [^{18}F]FNFP uptake even in the *ex-vivo* study. Tumors were, after the ex-vivo study, thoroughly examined noticing that all presented areas of necrosis perhaps due to hypoxia. Although apoptosis and necrosis are conceptually distinct pathways of cell death, recent advances have revealed that hypoxic cell damage can induce both necrosis and apoptosis simultaneously [239].

There is a possibility of testing [^{18}F]FNFP, maybe chemically modified to also include a secondary amine in its structure, to see if it shows some binding to β-amyloid specific proteins and therefore as a β-amyloid plaques imaging agent, leading to a different idea than the proposed in this work.

Regarding its use as a hypoxic imaging agent, *in vitro* studies are first necessary to actually see if the radiotracer is able to accumulate in different cell lines under hypoxic conditions, a study that could not be carried out in this work. Once achieved this, other chemical modifications might be necessary in order to increase [^{18}F]FNFP's circulation time and therefore a chance to get into the tumor, so we got a lot of work to do on this matter. We believe that the use of radiopharmaceuticals for imaging hypoxia is not only restricted to nitroimidazole-based probes and specifically to [^{18}F]FMISO, since the mechanism of action of these compounds depends on the presence of the nitroaromatic moiety and the irreversible reduction steps they undergo under hypoxic conditions.

7 CONCLUSIONS

1. (E)-1-(4-fluorophenyl)-3-(5-nitrofuran-2-yl)prop-2-en-1-one, [^{19}F]FNFP, and N-(4-fluorobenzyl)-2-(2-nitro-1H-imidazol-1-yl)-acetamide, [^{19}F]FBNA, were successfully synthesized, and chemically and structurally characterized (including its synthetic intermediates) by Nuclear Magnetic Resonance (NMR), Melting point, Mass Spectrometry (MS) and Infrared Spectroscopy techniques.

2. [^{18}F]FNFP and [^{19}F]FBNA were efficiently radiolabeled with ^{18}F in a one-step/late-stage radiofluorination synthesis within short times, high radiochemical overall yields, molar activities, and radiochemical purity.

3. [^{18}F]FNFP was found to be stable in PBS and serum for up to 6 hours and more hydrophilic than [^{18}F]FMISO, with the same partition coefficient as [^{18}F]FBNA.

4. PET/CT images using a gastric cancer tumor model in mice showed that [^{18}F]FNFP, a chalcone derivate, is rapidly excreted by a hepato-biliary-intestinal-renal clearance with no tumor uptake. Similar to its counterparts chalcone-based radiotracers, has a rapid washout from the brain with a high uptake in this organ in the first 15 minutes after injection.

5. *Ex vivo* biodistribution studies likewise showed no interesting tumor uptake for [^{18}F]FNFP. Different from the 2-nitroimidazole-based radiotracer [^{18}F]FBNA, the 5-nitrofuran derivate [^{18}F]FNFP was not nearly as effective as the former in identifying hypoxic regions in the tumor microenvironment.

8 REFERENCES

1. Krieghoff-Henning, E., Folkerts, J., Penzkofer, A., & Weg-Remers, S., *Cancer – an overview.* Krebs – ein Überblick. Medizinische Monatsschrift fur Pharmazeuten, 2017. **40**(2): p. 48–54.

2. Nagai, H., & Kim, Y. H., *Cancer prevention from the perspective of global cancer burden patterns.* Journal of Thoracic Disease, 2017. **9**(3): p. 448–451.

3. Santos, M.d.O., Lima, F. C. da S. de, Martins, L. F. L., Oliveira, J. F. P., Almeida , L. M. de, & Cancela, M. de C. , *Estimativa de Incidência de Câncer no Brasil, 2023-2025.* Revista Brasileira De Cancerologia, 2023. **69**(1).

4. Hanahan, D., & Weinberg, R. A., *Hallmarks of cancer: the next generation.* Cell, 2011. **144**(5): p. 646–674.

5. Tímár, J., Sebestyén A., Kopper L., Dankó T., *Hypoxia Signaling in Cancer: From Basics to Clinical Practice* Pathology and Oncology Research 2021. **27**.

6. Shi, R., Liao, C., & Zhang, Q., *Hypoxia-Driven Effects in Cancer: Characterization, Mechanisms, and Therapeutic Implications.* Cells, 2021. **10**(3): p. 678.

7. Abou Khouzam, R., Brodaczewska, K., Filipiak, A., Zeinelabdin, N. A., Buart, S., Szczylik, C., Kieda, C., & Chouaib, S., *Tumor Hypoxia Regulates Immune Escape/Invasion: Influence on Angiogenesis and Potential Impact of Hypoxic Biomarkers on Cancer Therapies.* Frontiers in Immunology 2021. **11**.

8. Ruan, K., Song, G., & Ouyang, G., *Role of hypoxia in the hallmarks of human cancer.* Journal of cellular biochemistry, 2009. **107**(6): p. 1053–1062.

9. Mees, G., Dierckx, R., Vangestel, C., & Van de Wiele, C., *Molecular imaging of hypoxia with radiolabelled agents.* European Journal of Nuclear Medicine and Molecular Imaging, 2009. **36**(10): p. 1674–1686.

10. Hughes, V.S., Wiggins, J. M., & Siemann, D. W., *Tumor oxygenation and cancer therapy-then and now.* The British journal of radiology, 2019. **92**.

11. EK., R., *Novel radiation sensitizers targeting tissue hypoxia.* Oncology (Williston Park), 1999. **13**(10 Suppl 5): p. 61-70.

12. Yasui, H., Kubota, N., Nishizumi, J., Sakai, Y., Yamamori, T., & Inanami, O., *Preclinical study on hypoxic radiosensitizing effects of glycididazole in comparison with those of doranidazole in vitro and in vivo.* Oncology letters, 20[18]. **15**(2): p. 1993–1998.

13. Fowler, J.F., Adams, G. E., & Denekamp, J., *Radiosensitizers of hypoxic cells in solid tumors.* Cancer treatment reviews, 1976. **3**(4): p. 227–256.

14. E., A.G., *Chemical radiosensitization of hypoxic cells.* British medical bulletin, 1973. **29**(1): p. 48–53.

15. Wang, H., Mu, X., He, H., & Zhang, X. D., *Cancer Radiosensitizers.* Trends in pharmacological sciences, 20[18]. **39**(1): p. 24–48.

16. J., S.I., *Mechanisms of hypoxic cell radiosensitization and the development of new sensitizers.* International Journal of Radiation Oncology, Biology, Physics, 1982. **8**(3-4): p. 391–398.

17. P., W., *Nitroimidazoles as hypoxic cell radiosensitizers and hypoxia probes: misonidazole, myths and mistakes.* The British journal of radiology, 2019. **92**.

18. Priyanka D., K.R., *Nitroaromatics as hypoxic cell radiosensitizers: A 2D-QSAR approach to explore structural features contributing to radiosensitization effectiveness.* European Journal of Medicinal Chemistry Reports, 2022. **4**.

19. Naylor, M.A., Stephens, M. A., Cole, S., Threadgill, M. D., Stratford, I. J., O'Neill, P., Fielden, E. M., & Adams, G. E., *Synthesis and evaluation of novel electrophilic nitrofuran carboxamides and carboxylates as radiosensitizers and bioreductively activated cytotoxins.* Journal of Medicinal Chemistry, 1990. **33**(9): p. 2508–2513.

20. Patterson, S., & Wyllie, S., *Nitro drugs for the treatment of trypanosomatid diseases: past, present, and future prospects.* Trends in parasitology, 2014. **30**(6): p. 289–298.

21. Fleming, I.N., Manavaki, R., Blower, P. J., West, C., Williams, K. J., Harris, A. L., Domarkas, J., Lord, S., Baldry, C., & Gilbert, F. J., *Imaging tumour hypoxia with positron emission tomography.* British journal of cancer, 2015. **112**(2): p. 238–250.

22. Adams, G.E., Flockhart, I. R., Smithen, C. E., Stratford, I. J., Wardman, P., & Watts, M. E., *Electron-affinic sensitization. VII. A correlation between structures, one-electron reduction potentials, and efficiencies of nitroimidazoles as hypoxic cell radiosensitizers.* Radiation research, 1976. **67**(1): p. 9–20.

23. M., B.J., *Selective radiosensitization of the hypoxic cells of mouse tumors with the nitroimidazoles metronidazole and Ro 7-0582.* Radiation research, 1975. **64**(3): p. 633–647.

24. Dische, S., Saunders, M. I., Lee, M. E., Adams, G. E., & Flockhart, I. R., *Clinical testing of the radiosensitizer Ro 07-0582: experience with multiple doses.* British journal of cancer, 1977. **35**(5): p. 567–579.

25. M., B.J., *Clinical trials of radiosensitizers: what should we expect?* International journal of radiation oncology, biology, physics, 1984. **10**(3): p. 425–429.

26. Kaanders, J.H., Bussink, J., & van der Kogel, A. J., *Clinical studies of hypoxia modification in radiotherapy.* Seminars in radiation oncology, 2004. **14**(3): p. 233–240.

27. E., W.M., *Radiosensitization of hypoxic cells by a nitrofuran; dose-modifying and shoulder effects. .* International journal of radiation biology and related studies in physics, chemistry, and medicine., 1977. **31**(3): p. 237–250.

28. Gong, L., Zhang, Y., Liu, C., Zhang, M., & Han, S., *Application of Radiosensitizers in Cancer Radiotherapy.* International Journal of Nanomedicine, 2021. **16**: p. 1083–1102.

29. Bonnet, M., Hong, C. R., Wong, W. W., Liew, L. P., Shome, A., Wang, J., Gu, Y., Stevenson, R. J., Qi, W., Anderson, R. F., Pruijn, F. B., Wilson, W. R., Jamieson, S. M. F., Hicks, K. O., & Hay, M. P., *Next-Generation Hypoxic Cell*

Radiosensitizers: Nitroimidazole Alkylsulfonamides. Journal of Medicinal Chemistry, 2018. **61**(3): p. 1241–1254.

30. Krohn, K.A., Link, J. M., & Mason, R. P., *Molecular imaging of hypoxia.* Journal of nuclear edicine : official publication, Society of Nuclear Medicine, 2008.

31. Busk, M., Munk, O. L., Jakobsen, S. S., & Horsman, M. R., *Hypoxia positron emission tomography imaging: combining information on perfusion and tracer retention to improve hypoxia specificity.* Acta oncologica (Stockholm, Sweden), 2017. **56**(11): p. 1583–1590.

32. Koh, W.J., Rasey, J. S., Evans, M. L., Grierson, J. R., Lewellen, T. K., Graham, M. M., Krohn, K. A., & Griffin, T. W., *Imaging of hypoxia in human tumors with [F-^{18}]fluoromisonidazole.* International Journal of radiation Oncology, Biology, Physics, 1992. **22**(1): p. 199–212.

33. Grönroos, T. and H. Minn, *Imaging of tumour hypoxia using PET and ^{18}F-labelled tracers: Biology meets technology.* European journal of nuclear medicine and molecular imaging, 2007. **34**: p. 1563-5.

34. Salim F. Farah, R.A.M., Michael R. Peterson, and Imre G. Csizmadia, *Molecular structure and relative proton and electron affinities of isomeric nitroimidazoles.* Canadian Journal of Chemistry, 2011. **67**(10): p. 1666-1671.

35. Meisel, D.C., & Neta, P., *One-electron redox potentials of nitro compounds and radiosensitizers. Correlation with spin densities of their radical anions.* Journal of the American Chemical Society, 1975. **97**: p. 5198-5203.

36. Fielden, E.M., Adams, G. E., Cole, S., Naylor, M. A., O'Neill, P., Stephens, M. A., & Stratford, I. J., *Assessment of a range of novel nitro-aromatic radiosensitizers and bioreductive drugs.* International journal of radiation oncology, biology, physics, 1992. **22**(4): p. 707–711.

37. Chapman, J.D., Reuvers, A. P., Borsa, J., Petkau, A., & McCalla, D. R., *Nitrofurans as radiosensitizers of hypoxic mammalian cells.* Cancer research, 1972. **32**(12): p. 2616–2624.

38. Čėnas, N., Nemeikaitė-Čėnienė, A., & Kosychova, L., *Single- and Two-Electron Reduction of Nitroaromatic Compounds by Flavoenzymes: Mechanisms and Implications for Cytotoxicity. .* International journal of molecular sciences, 2021. **22**(16).

39. Olender, D., Żwawiak, J., & Zaprutko, L., *Multidirectional Efficacy of Biologically Active Nitro Compounds Included in Medicines.* Pharmaceuticals (Basel, Switzerland), 2018. **11**(2).

40. Nario, A.P., Woodfield, J., Dos Santos, S. N., Bergman, C., Wuest, M., Araújo, Y. B., Lapolli, A. L., West, F. G., Wuest, F., & Bernardes, E. S., *Synthesis of a 2-nitroimidazole derivative N-(4-[^{18}F]fluorobenzyl)-2-(2-nitro-1H-imidazol-1-yl)-acetamide ([^{18} F]FBNA) as PET radiotracer for imaging tumor hypoxia.* EJNMMI radiopharmacy and chemistry, 2022. **7**(1).

41. Flavahan, W.A., Gaskell, E., & Bernstein, B. E., *Epigenetic plasticity and the hallmarks of cancer.* Science (New York, N.Y.), 2017. **357**(6348).

42. Chakravarthi, B.V., Nepal, S., & Varambally, S., *Genomic and Epigenomic Alterations in Cancer.* The American journal of pathology, 2016. **186**(7): p. 1724–1735.

43. Śmiech, M., Leszczyński, P., Kono, H., Wardell, C., & Taniguchi, H., *Emerging BRAF Mutations in Cancer Progression and Their Possible Effects on Transcriptional Networks.* Genes, 2020. **11**(11).

44. Tseng, L.J., Matsuyama, A., & MacDonald-Dickinson, V., *Histology: The gold standard for diagnosis?* The Canadian veterinary journal = La revue veterinaire canadienne, 2023. **64**(4): p. 389–391.

45. L., F., *Imaging and cancer: a review. .* Molecular oncology, 2008. **2**(2): p. 115–152.

46. Badowski, C., He, B., & Garmire, L. X., *Blood-derived lncRNAs as biomarkers for cancer diagnosis: the Good, the Bad and the Beauty.* NPJ precision oncology, 2022. **6**(1).

47. Beylerli, O., Gareev, I., Sufianov, A., Ilyasova, T., & Guang, Y., *Long noncoding RNAs as promising biomarkers in cancer.* Non-coding RNA research, 2022. **7**(2): p. 66-70.

48. Yuan, S., Xiang, Y., Guo, X., Zhang, Y., Li, C., Xie, W., Wu, N., Wu, L., Cai, T., Ma, X., Yu, Z., Bai, L., & Li, Y., *Circulating Long Noncoding RNAs Act as Diagnostic Biomarkers in Non-Small Cell Lung Cancer.* Frontiers in oncology, 2020. **10**.

49. Weber, J., Haberkorn, U., & Mier, W., *Cancer stratification by molecular imaging.* International journal of molecular sciences, 2015. **16**(3): p. 4918–4946.

50. Sun, Z., Ng, K. H., & Ramli, N. (2011). , *Biomedical imaging research: a fast-emerging area for interdisciplinary collaboration.* Biomedical imaging and intervention journal, 2011. **7**(3).

51. García-Figueiras, R., Baleato-González, S., Padhani, A. R., Luna-Alcalá, A., Vallejo-Casas, J. A., Sala, E., Vilanova, J. C., Koh, D. M., Herranz-Carnero, M., & Vargas, H. A. , *How clinical imaging can assess cancer biology.* Insights into imaging, 2019. **10**(1).

52. Winfield, J.M., Payne, G. S., & deSouza, N. M. (2015). , *Functional MRI and CT biomarkers in oncology.* European journal of nuclear medicine and molecular imaging, 2015. **42**(2): p. 562–578.

53. Muz, B., de la Puente, P., Azab, F., & Azab, A. K., *The role of hypoxia in cancer progression, angiogenesis, metastasis, and resistance to therapy.* Hypoxia (Auckland, N.Z.), 2015. **3**: p. 83–92.

54. Emami Nejad, A., Najafgholian, S., Rostami, A., Sistani, A., Shojaeifar, S., Esparvarinha, M., Nedaeinia, R., Haghjooy Javanmard, S., Taherian, M., Ahmadlou, M., Salehi, R., Sadeghi, B., & Manian, M., *The role of hypoxia in the tumor microenvironment and development of cancer stem cell: a novel approach to developing treatment.* Cancer cell international, 2021. **21**(1).

55. Erler, J.T., Cawthorne, C. J., Williams, K. J., Koritzinsky, M., Wouters, B. G., Wilson, C., Miller, C., Demonacos, C., Stratford, I. J., & Dive, C., *Hypoxia-*

mediated down-regulation of Bid and Bax in tumors occurs via hypoxia-inducible factor 1-dependent and -independent mechanisms and contributes to drug resistance. . Molecular and cellular biology, 2004. **24**(7): p. 2875–2889.

56. Rouschop, K.M., van den Beucken, T., Dubois, L., Niessen, H., Bussink, J., Savelkouls, K., Keulers, T., Mujcic, H., Landuyt, W., Voncken, J. W., Lambin, P., van der Kogel, A. J., Koritzinsky, M., & Wouters, B. G., *The unfolded protein response protects human tumor cells during hypoxia through regulation of the autophagy genes MAP1LC3B and ATG5. .* The Journal of clinical investigation, 2010. **120**(1): p. 127–141.

57. Cairns, R.A., Harris, I. S., & Mak, T. W., *Regulation of cancer cell metabolism.* Nature reviews. Cancer, 2011. **11**(2): p. 85–95.

58. Liberti, M.V., & Locasale, J. W., *The Warburg Effect: How Does it Benefit Cancer Cells?* Trends in biochemical sciences, 2016. **41**(3): p. 211–218.

59. Liu, C., Jin, Y., & Fan, Z., *The Mechanism of Warburg Effect-Induced Chemoresistance in Cancer.* Frontiers in oncology, 2021. **11**.

60. Benjamin, D., Robay, D., Hindupur, S. K., Pohlmann, J., Colombi, M., El-Shemerly, M. Y., Maira, S. M., Moroni, C., Lane, H. A., & Hall, M. N., *Dual Inhibition of the Lactate Transporters MCT1 and MCT4 Is Synthetic Lethal with Metformin due to NAD+ Depletion in Cancer Cells. .* Cell reports, 2018. **25**(11): p. 3047–3058.

61. da Silva, V.P., Mesquita, C. B., Nunes, J. S., de Bem Prunes, B., Rados, P. V., & Visioli, F., *Effects of extracellular acidity on resistance to chemotherapy treatment: a systematic review. .* Medical oncology (Northwood, London, England), 2018. **35**(12).

62. Brown, T.P., & Ganapathy, V., *Lactate/GPR81 signaling and proton motive force in cancer: Role in angiogenesis, immune escape, nutrition, and Warburg phenomenon. .* Pharmacology & therapeutics, 2020. **206**.

63. Mahoney, B.P., Raghunand, N., Baggett, B., & Gillies, R. J., *Tumor acidity, ion trapping and chemotherapeutics. Acid pH affects the distribution of*

chemotherapeutic agents in vitro. . Biochemical pharmacology, 2003. **66**(7): p. 1207–1218.

64. Raghunand, N., Martínez-Zaguilán, R., Wright, S. H., & Gillies, R. J., *pH and drug resistance. II. Turnover of acidic vesicles and resistance to weakly basic chemotherapeutic drugs.* Biochemical pharmacology, 1999. **57**(9): p. 1047–1058.

65. Walsh, J.C., Lebedev, A., Aten, E., Madsen, K., Marciano, L., & Kolb, H. C., *The clinical importance of assessing tumor hypoxia: relationship of tumor hypoxia to prognosis and therapeutic opportunities.* Antioxidants & redox signaling, 2014. **21**(10): p. 1516–1554.

66. Yu, T., Tang, B., & Sun, X., *Development of Inhibitors Targeting Hypoxia-Inducible Factor 1 and 2 for Cancer Therapy.* Yonsei medical journal, 2017. **58**(3): p. 489–496.

67. Wu, D., Potluri, N., Lu, J., Kim, Y., & Rastinejad, F., *Structural integration in hypoxia-inducible factors.* Nature reviews. Cancer, 2015: p. 303–308.

68. Barben, M., Ail, D., Storti, F., Klee, K., Schori, C., Samardzija, M., Michalakis, S., Biel, M., Meneau, I., Blaser, F., Barthelmes, D., & Grimm, C., *Hif1a inactivation rescues photoreceptor degeneration induced by a chronic hypoxia-like stress.* Cell death and differentiation, 20[18]. **25**(12): p. 2071–2085.

69. L., S.G., *Regulation of metabolism by hypoxia-inducible factor 1.* Cold Spring Harbor symposia on quantitative biology, 2011. **76**: p. 347–353.

70. Li, H., Jia, Y., & Wang, Y., *Targeting HIF-1α signaling pathway for gastric cancer treatment.* Die Pharmazie, 2019. **74**(1): p. 3–7.

71. Qi, Y., Liu, J., Saadat, S., Tian, X., Han, Y., Fong, G. H., Pandolfi, P. P., Lee, L. Y., & Li, S., *PTEN induces apoptosis and cavitation via HIF-2-dependent Bnip3 upregulation during epithelial lumen formation.* Cell death and differentiation, 2015. **22**(5): p. 875–884.

72. Bao, X., Zhang, J., Huang, G., Yan, J., Xu, C., Dou, Z., Sun, C., & Zhang, H., *The crosstalk between HIFs and mitochondrial dysfunctions in cancer development.* Cell death & disease, 2021. **12**(2).

73. Vaupel, P., & Harrison, L., *Tumor hypoxia: causative factors, compensatory mechanisms, and cellular response.* The oncologist, 2004. **9**(5): p. 4–9.

74. Wallace, E.M., Rizzi, J. P., Han, G., Wehn, P. M., Cao, Z., Du, X., Cheng, T., Czerwinski, R. M., Dixon, D. D., Goggin, B. S., Grina, J. A., Halfmann, M. M., Maddie, M. A., Olive, S. R., Schlachter, S. T., Tan, H., Wang, B., Wang, K., Xie, S., Xu, R., … Josey, J. A., *A Small-Molecule Antagonist of HIF2α Is Efficacious in Preclinical Models of Renal Cell Carcinoma. Cancer research.* Cancer research, 2016. **76**(18): p. 5491–5500.

75. Weber, H., Valbuena, J. R., Barbhuiya, M. A., Stein, S., Kunkel, H., García, P., Bizama, C., Riquelme, I., Espinoza, J. A., Kurtz, S. E., Tyner, J. W., Calderon, J. F., Corvalán, A. H., Grez, M., Pandey, A., Leal-Rojas, P., & Roa, J. C., *Small molecule inhibitor screening identifified HSP90 inhibitor 17-AAG as potential therapeutic agent for gallbladder cancer.* Oncotarget, 2017. **8**(16): p. 26169-26184.

76. Kim, Y.S., Alarcon, S. V., Lee, S., Lee, M. J., Giaccone, G., Neckers, L., & Trepel, J. B., *Update on Hsp90 inhibitors in clinical trial.* Current topics in medicinal chemistry, 2009. **9**(15): p. 1479–1492.

77. Liu, Y.V., Baek, J. H., Zhang, H., Diez, R., Cole, R. N., & Semenza, G. L., *RACK1 competes with HSP90 for binding to HIF-1alpha and is required for O(2)-independent and HSP90 inhibitor-induced degradation of HIF-1alpha. .* Molecular cell, 2007. **25**(2): p. 207–217.

78. Solit, D.B., Ivy, S. P., Kopil, C., Sikorski, R., Morris, M. J., Slovin, S. F., Kelly, W. K., DeLaCruz, A., Curley, T., Heller, G., Larson, S., Schwartz, L., Egorin, M. J., Rosen, N., & Scher, H. I., *Phase I trial of 17-allylamino-17-demethoxygeldanamycin in patients with advanced cancer.* Clinical cancer research : an official journal of the American Association for Cancer

ResearchClinical cancer research : an official journal of the American Association for Cancer Research, 2007. **13**(6): p. 1775–1782.

79. Kummar, S., Gutierrez, M. E., Gardner, E. R., Chen, X., Figg, W. D., Zajac-Kaye, M., Chen, M., Steinberg, S. M., Muir, C. A., Yancey, M. A., Horneffer, Y. R., Juwara, L., Melillo, G., Ivy, S. P., Merino, M., Neckers, L., Steeg, P. S., Conley, B. A., Giaccone, G., Doroshow, J. H., … Murgo, A. J., *Phase I trial of 17-dimethylaminoethylamino-17-demethoxygeldanamycin (17-DMAG), a heat shock protein inhibitor, administered twice weekly in patients with advanced malignancies.* European journal of cancer (Oxford, England), 1990. **46**(2): p. 340–347.

80. Pacey, S., Wilson, R. H., Walton, M., Eatock, M. M., Hardcastle, A., Zetterlund, A., Arkenau, H. T., Moreno-Farre, J., Banerji, U., Roels, B., Peachey, H., Aherne, W., de Bono, J. S., Raynaud, F., Workman, P., & Judson, I., *A phase I study of the heat shock protein 90 inhibitor alvespimycin (17-DMAG) given intravenously to patients with advanced solid tumors.* Clinical cancer research : an official journal of the American Association for Cancer Research, 2011. **17**(6): p. 1561–1570.

81. Zhe, N., Chen, S., Zhou, Z., Liu, P., Lin, X., Yu, M., Cheng, B., Zhang, Y., & Wang, J., *HIF-1α inhibition by 2-methoxyestradiol induces cell death via activation of the mitochondrial apoptotic pathway in acute myeloid leukemia. .* Cancer biology & therapy, 2016. **17**(6): p. 625–634.

82. Wouters, B.G., & Koritzinsky, M., *Hypoxia signalling through mTOR and the unfolded protein response in cancer.* Nature reviews. Cancer, 2008. **8**(11): p. 851–864.

83. Rathmell, W.K., & Chen, S., *VHL inactivation in renal cell carcinoma: implications for diagnosis, prognosis and treatment. .* Expert review of anticancer therapy, 2008. **8**(1): p. 63–73.

84. Kroeger, H., Grimsey, N., Paxman, R., Chiang, W. C., Plate, L., Jones, Y., Shaw, P. X., Trejo, J., Tsang, S. H., Powers, E., Kelly, J. W., Wiseman, R. L., &

Lin, J. H., *The unfolded protein response regulator ATF6 promotes mesodermal differentiation.* 20[18]. **11**(517).

85. Walter, P., & Ron, D., *The unfolded protein response: from stress pathway to homeostatic regulation.* Science (New York, N.Y.), 2011: p. 1081–1086.

86. Fels, D.R., Ye, J., Segan, A. T., Kridel, S. J., Spiotto, M., Olson, M., Koong, A. C., & Koumenis, C., *Preferential cytotoxicity of bortezomib toward hypoxic tumor cells via overactivation of endoplasmic reticulum stress pathways.* Cancer research, 2008. **68**(22): p. 9323–9330.

87. Yang, Y., & Cao, Y., *The impact of VEGF on cancer metastasis and systemic disease.* Seminars in cancer biology, 2022. **86**: p. 251–261.

88. V., B.M., *Cancer prevention with rapamycin.* Oncotarget, 2023. **14**: p. 342–350.

89. Yu, K., Shi, C., Toral-Barza, L., Lucas, J., Shor, B., Kim, J. E., Zhang, W. G., Mahoney, R., Gaydos, C., Tardio, L., Kim, S. K., Conant, R., Curran, K., Kaplan, J., Verheijen, J., Ayral-Kaloustian, S., Mansour, T. S., Abraham, R. T., Zask, A., & Gibbons, J. J. , *Beyond rapalog therapy: preclinical pharmacology and antitumor activity of WYE-125132, an ATP-competitive and specific inhibitor of mTORC1 and mTORC2. .* Cancer research, 2010. **70**(2): p. 621–631.

90. Bredell, M.G., Ernst, J., El-Kochairi, I., Dahlem, Y., Ikenberg, K., & Schumann, D. M., *Current relevance of hypoxia in head and neck cancer.* Oncotarget, 2016. **7**(31): p. 50781–50804.

91. Godet, I., Doctorman, S., Wu, F., & Gilkes, D. M., *Detection of Hypoxia in Cancer Models: Significance, Challenges, and Advances.* Cells, 2022. **11**(4): p. 686.

92. Brown, J.M., & Le, Q. T., *Tumor hypoxia is important in radiotherapy, but how should we measure it?* International journal of radiation oncology, biology, physics., 2002. **54**(5): p. 1299–1301.

93. T., L.Q., *Identifying and targeting hypoxia in head and neck cancer: a brief overview of current approaches.* International journal of radiation oncology, biology, physics, 2007. **69**((2 Suppl)): p. S56–S58.

94. Gaertner, F.C., Souvatzoglou, M., Brix, G., & Beer, A. J., *Imaging of hypoxia using PET and MRI.* Current pharmaceutical biotechnology, 2012. **13**(4): p. 552–570.

95. Stone, H.B., Brown, J. M., Phillips, T. L., & Sutherland, R. M., *Oxygen in human tumors: correlations between methods of measurement and response to therapy. Summary of a workshop held November 19-20, 1992, at the National Cancer Institute, Bethesda, Maryland.* Radiation research,, 1993. **136**(3): p. 422–434.

96. Krzyszczyk, P., Acevedo, A., Davidoff, E. J., Timmins, L. M., Marrero-Berrios, I., Patel, M., White, C., Lowe, C., Sherba, J. J., Hartmanshenn, C., O'Neill, K. M., Balter, M. L., Fritz, Z. R., Androulakis, I. P., Schloss, R. S., & Yarmush, M. L., *The growing role of precision and personalized medicine for cancer treatment.* Technology, 2018. **6**(3-4): p. 79–100.

97. Wilson, W.R., & Hay, M. P., *Targeting hypoxia in cancer therapy. .* Nature reviews. Cancer, 2011. **11**(6): p. 393–410.

98. Franzone, P., Fiorentino, A., Barra, S., Cante, D., Masini, L., Cazzulo, E., Todisco, L., Gabriele, P., Garibaldi, E., Merlotti, A., Redda, M. G., Alongi, F., & Corvò, R., *Image-guided radiation therapy (IGRT): practical recommendations of Italian Association of Radiation Oncology (AIRO).* La Radiologia medica, 2016. **121**(12): p. 958–965.

99. Ge, Y., & Wu, Q. J., *Knowledge-based planning for intensity-modulated radiation therapy: A review of data-driven approaches. .* Medical physics, 2019. **46**(6): p. 2760–2775.

100. Moen, I., & Stuhr, L. E., *Hyperbaric oxygen therapy and cancer--a review.* Targeted oncology, 2012. **7**(4): p. 233–242.

101. GRAY, L.H., CONGER, A. D., EBERT, M., HORNSEY, S., & SCOTT, O. C., *The concentration of oxygen dissolved in tissues at the time of irradiation as a factor in radiotherapy.* The British journal of radiology, 1953. **26**(312): p. 638–648.

102. Adams, G.E., Asquith, J. C., Dewey, D. L., Foster, J. L., Michael, B. D., & Willson, R. L., *Electron affinic sensitization. II. Para-nitroacetophenone: a radiosensitizer for anoxic bacterial and mammalian cells.* International journal of radiation biology and related studies in physics, chemistry, and medicine., 1971. **19**(6): p. 575–585.

103. Chapman, J.D., Webb, R. G., & Borsa, J., *Radiosensitization of mammalian cells by p-nitroacetophenone. I. Characterization in asynchronous and synchronous populations.* International journal of radiation biology and related studies in physics, chemistry, and medicine, 1971. **19**(6): p. 561–573.

104. Zuma, N.H., Aucamp, J., & N'Da, D. D., *An update on derivatisation and repurposing of clinical nitrofuran drugs.* European journal of pharmaceutical sciences : official journal of the European Federation for Pharmaceutical Sciences, 2019. **140**.

105. Saayman, M., Kannigadu, C., Aucamp, J., Janse van Rensburg, H. D., Joseph, C., Swarts, A. J., & N'Da, D. D., *Design, synthesis, electrochemistry and anti-trypanosomatid hit/lead identification of nitrofuranylazines.* RSC medicinal chemistry, 2023. **14**(10): p. 2012–2029.

106. Leitner, A., Zöllner, P., & Lindner, W., *Determination of the metabolites of nitrofuran antibiotics in animal tissue by high-performance liquid chromatography-tandem mass spectrometry.* Journal of chromatography, 2001. **939**(1-2): p. 49-58.

107. Wang, K., Kou, Y., Wang, M., Ma, X., & Wang, J., *Determination of Nitrofuran Metabolites in Fish by Ultraperformance Liquid Chromatography-Photodiode Array Detection with Thermostatic Ultrasound-Assisted Derivatization.* ACS omega, 2020. **5**(30): p. 18887–18893.

108. Foster, J.L., & Willson, R. L., *Radiosensitization of anoxic cells by metronidazole.* The British journal of radiology, 1973. **46**: p. 234–235.

109. Bern, C., Montgomery, S. P., Herwaldt, B. L., Rassi, A., Jr, Marin-Neto, J. A., Dantas, R. O., Maguire, J. H., Acquatella, H., Morillo, C., Kirchhoff, L. V., Gilman, R. H., Reyes, P. A., Salvatella, R., & Moore, A. C., *Evaluation and treatment of chagas disease in the United States: a systematic review.* JAMA, 2007. **298**(18): p. 2171–2181.

110. Asquith, J.C., Watts, M. E., Patel, K., Smithen, C. E., & Adams, G. E., *Electron affinic sensitization. V. Radiosensitization of hypoxic bacteria and mammalian cells in vitro by some nitroimidazoles and nitropyrazoles.* Radiation research 1974. **60**(1): p. 108–118.

111. Asakawa, H., Watarai, J., & Hoshino, T., *[Clinical evaluation of hypoxic cell sensitizer (Misonidazole)].* Gan to kagaku ryoho. Cancer & chemotherapy, 1984. **11**(6): p. 1225–1230.

112. M., B.J., *Clinical perspectives for the use of new hypoxic cell sensitizers.* International journal of radiation oncology, biology, physics, 1982. **8**(9): p. 1491–1497.

113. S., D., *Chemical sensitizers for hypoxic cells: a decade of experience in clinical radiotherapy.* Radiotherapy and oncology : journal of the European Society for Therapeutic Radiology and Oncology, 1985. **3**(2): p. 97–115.

114. Rice, A.M., Long, Y., & King, S. B., *Nitroaromatic Antibiotics as Nitrogen Oxide Sources.* Biomolecules, 2021. **11**(2).

115. de Oliveira, I.M., Bonatto, D., & Henriques, J. A. P., *Nitroreductases: enzymes with environmental, biotechnological and clinical importance.* Current research, technology and education topics in applied microbiology and microbial biotechnology, 2010. **2**(1): p. 1008-1019.

116. Whitmore, G.F., & Varghese, A. J., *The biological properties of reduced nitroheterocyclics and possible underlying biochemical mechanisms.* Biochemical pharmacology, 1986. **35**(1): p. 97–103.

117. Streeter, A.J., & Hoener, B. A., *Evidence for the involvement of a nitrenium ion in the covalent binding of nitrofurazone to DNA.* Pharmaceutical research, 1988. **5**(7): p. 434–436.

118. Peterson, F.J., Mason, R. P., Hovsepian, J., & Holtzman, J. L., *Oxygen-sensitive and -insensitive nitroreduction by Escherichia coli and rat hepatic microsomes.* The Journal of biological chemistry, 1979. **254**(10): p. 4009–4014.

119. Adams, G.E., Ahmed, I., Sheldon, P. W., & Stratford, I. J., *Radiation sensitization and chemopotentiation: RSU 1069, a compound more efficient than misonidazole in vitro and in vivo.* British journal of cancer, 1984. **49**(5): p. 571–577.

120. Adams, G.E., Clarke, E. D., Flockhart, I. R., Jacobs, R. S., Sehmi, D. S., Stratford, I. J., Wardman, P., Watts, M. E., Parrick, J., Wallace, R. G., & Smithen, C. E. (1979). *Structure-activity relationships in the development of hypoxic cell radiosensitizers.* International journal of radiation biology and related studies in physics, chemistry, and medicine, 1979. **35**(2): p. 133–150.

121. J., W.M., *Lipophilicity in drug discovery.* Expert opinion on drug discovery, 2010. **5**(3): p. 235–248.

122. Wardman, P. and E.D. Clarke, *One-electron reduction potentials of substituted nitroimidazoles measured by pulse radiolysis.* Journal of the Chemical Society, Faraday Transactions 1: Physical Chemistry in Condensed Phases, 1976. **72**(0): p. 1377-1390.

123. Sjöuberg, L. and T.E. Eriksen, *Nitrobenzenes: a comparison of pulse radiolytically determined one-electron reduction potentials and calculated electron affinities.* Journal of the Chemical Society, Faraday Transactions 1: Physical Chemistry in Condensed Phases, 1980. **76**(0): p. 1402-1408.

124. Smeyers, Y.G., De Bueren, A., Alcala, R., & Alvarez, M. V., *Theoretical approach for radiosensitizers. Correlation between calculated electroaffinity and sensitization factors of nitro-compounds.* International journal

of radiation biology and related studies in physics, chemistry, and medicine, 1981. **39**(6): p. 649–653.

125. Chapman, J., Franko, A. & Sharplin, J. . Br J Cancer, *A marker for hypoxic cells in tumours with potential clinical applicability.* British Journal of Cancer, 1981. **43**: p. 546–550.

126. Garrecht, B.M., & Chapman, J. D., *The labelling of EMT-6 tumours in BALB/C mice with 14C-misonidazole.* The British journal of radiology, 1983. **56**(670): p. 745–753.

127. Urtasun, R.C., Koch, C. J., Franko, A. J., Raleigh, J. A., & Chapman, J. D., *A novel technique for measuring human tissue pO2 at the cellular level.* British journal of cancer, 1986. **54**(3): p. 453–457.

128. D., C.J., *Measurement of tumor hypoxia by invasive and non-invasive procedures: a review of recent clinical studies.* Radiotherapy and oncology : journal of the European Society for Therapeutic Radiology and Oncology, 1991. **20**: p. 13–19.

129. Hughes, V.S., Wiggins, J. M., & Siemann, D. W. (2019). , 92(1093), 20170955. , *Tumor oxygenation and cancer therapy-then and now.* The British journal of radiology, 2019. **92**.

130. Weissleder, R., & Pittet, M. J., *Imaging in the era of molecular oncology.* Nature reviews. Cancer, 2008. **452**: p. 580–589.

131. Israel, O., Pellet, O., Biassoni, L., De Palma, D., Estrada-Lobato, E., Gnanasegaran, G., Kuwert, T., la Fougère, C., Mariani, G., Massalha, S., Paez, D., & Giammarile, F. , *Two decades of SPECT/CT - the coming of age of a technology: An updated review of literature evidence.* European journal of nuclear medicine and molecular imaging, 2019. **46**(10): p. 1990–2012. .

132. Chin, B.B., R.B. Workman, and R.E. Coleman, *Fluorodeoxyglucose-PET in Breast Cancer*, in *PET/CT: Essentials for Clinical Practice*, R.B. Workman and R.E. Coleman, Editors. 2006, Springer New York: New York, NY. p. 89-103.

133. Slobbe, P., Poot, A. J., Windhorst, A. D., & van Dongen, G. A., *PET imaging with small-molecule tyrosine kinase inhibitors: TKI-PET.* Drug discovery today, 2012. **17**(21-22): p. 1175–1187.

134. Lopci, E., Grassi, I., Chiti, A., Nanni, C., Cicoria, G., Toschi, L., Fonti, C., Lodi, F., Mattioli, S., & Fanti, S., *PET radiopharmaceuticals for imaging of tumor hypoxia: a review of the evidence. .* American journal of nuclear medicine and molecular imaging, 2014. **4**(4): p. 365–384.

135. A., L., *A systematic review of PET and PET/CT in oncology: a way to personalize cancer treatment in a cost-effective manner?* BMC health services research, 2010. **10**(283).

136. A., D., *Review on 99mTc radiopharmaceuticals with emphasis on new advancements.* Nuclear medicine and biology, 2021. **92**: p. 202–216.

137. Jerabek, P.A., Patrick, T. B., Kilbourn, M. R., Dischino, D. D., & Welch, M. J., *Synthesis and biodistribution of ^{18}F-labeled fluoronitroimidazoles: potential in vivo markers of hypoxic tissue.* International journal of radiation applications and instrumentation. Part A, Applied radiation and isotopes, 1986. **37**(7): p. 599–605.

138. Carlin, S., & Humm, J. L., *PET of hypoxia: current and future perspectives.* Journal of nuclear medicine : official publication, Society of Nuclear Medicine, 2012. **53**(8): p. 1171–1174.

139. Piert, M., Machulla, H. J., Picchio, M., Reischl, G., Ziegler, S., Kumar, P., Wester, H. J., Beck, R., McEwan, A. J., Wiebe, L. I., & Schwaiger, M., *Hypoxia-specific tumor imaging with ^{18}F-fluoroazomycin arabinoside.* Journal of Nuclear Medicine, 2005. **46**(1): p. 106–113.

140. Grosu, A.L., Souvatzoglou, M., Röper, B., Dobritz, M., Wiedenmann, N., Jacob, V., Wester, H. J., Reischl, G., Machulla, H. J., Schwaiger, M., Molls, M., & Piert, M. , *Hypoxia imaging with FAZA-PET and theoretical considerations with regard to dose painting for individualization of radiotherapy in patients with*

head and neck cancer. . International journal of radiation oncology, biology, physics., 2007. **69**(2): p. 541–551.

141. Thureau, S., Piton, N., Gouel, P., Modzelewski, R., Dujon, A., Baste, J. M., Melki, J., Rinieri, P., Peillon, C., Rastelli, O., Lequesne, J., Hapdey, S., Sabourin, J. C., Bohn, P., & Vera, P., *First Comparison between [^{18}F]-FMISO and [^{18}F]-FAZA for Preoperative Pet Imaging of Hypoxia in Lung Cancer.* Cancers, 2021. **13**(16).

142. Nguyen, A.T., & Kim, H. K., *Recent Developments in PET and SPECT Radiotracers as Radiopharmaceuticals for Hypoxia Tumors.* Pharmaceutics, 2023. **15**(7).

143. Wei, Y., Zhao, W., Huang, Y., Yu, Q., Zhu, S., Wang, S., Zhao, S., Hu, X., Yu, J., & Yuan, S., *A Comparative Study of Noninvasive Hypoxia Imaging with ^{18}F-Fluoroerythronitroimidazole and ^{18}F-Fluoromisonidazole PET/CT in Patients with Lung Cancer.* PloS one, 2016. **11**(6).

144. Carlin, S., Zhang, H., Reese, M., Ramos, N. N., Chen, Q., & Ricketts, S. A. , *A comparison of the imaging characteristics and microregional distribution of 4 hypoxia PET tracers.* Journal of nuclear medicine : official publication, Society of Nuclear Medicine, 2014. **55**(3): p. 515–521. .

145. Liu, T., Karlsen, M., Karlberg, A. M., & Redalen, K. R. , *Hypoxia imaging and theranostic potential of [64Cu][Cu(ATSM)] and ionic Cu(II) salts: a review of current evidence and discussion of the retention mechanisms.* EJNMMI research, 2020. **10**(1).

146. Savi, A., Incerti, E., Fallanca, F., Bettinardi, V., Rossetti, F., Monterisi, C., Compierchio, A., Negri, G., Zannini, P., Gianolli, L., & Picchio, M., *First Evaluation of PET-Based Human Biodistribution and Dosimetry of [^{18}F]FAZA, a Tracer for Imaging Tumor Hypoxia. .* Journal of nuclear medicine : official publication, Society of Nuclear Medicine, 2017. **58**(8): p. 1224–1229.

147. Fujibayashi, Y., Taniuchi, H., Yonekura, Y., Ohtani, H., Konishi, J., & Yokoyama, A., *Copper-62-ATSM: a new hypoxia imaging agent with high*

membrane permeability and low redox potential. Journal of nuclear medicine : official publication, Society of Nuclear Medicine, 1997. **38**(7): p. 1155–1160.

148. Groshar, D., McEwan, A. J., Parliament, M. B., Urtasun, R. C., Golberg, L. E., Hoskinson, M., Mercer, J. R., Mannan, R. H., Wiebe, L. I., & Chapman, J. D., *Imaging tumor hypoxia and tumor perfusion.* Journal of nuclear medicine : official publication, Society of Nuclear Medicine, 1993. **34**(6): p. 885–888.

149. Parliament, M.B., Chapman, J. D., Urtasun, R. C., McEwan, A. J., Golberg, L., Mercer, J. R., Mannan, R. H., & Wiebe, L. I., *Non-invasive assessment of human tumour hypoxia with 123I-iodoazomycin arabinoside: preliminary report of a clinical study.* British journal of cancer, 1992. **65**(1): p. 90–95.

150. Urtasun, R.C., Parliament, M. B., McEwan, A. J., Mercer, J. R., Mannan, R. H., Wiebe, L. I., Morin, C., & Chapman, J. D., *Measurement of hypoxia in human tumours by non-invasive spect imaging of iodoazomycin arabinoside.* The British journal of cancer, 1996. **27**: p. S209–S212.

151. Lee, H.C., Kumar, P., McEwan, A. J., Wiebe, L. I., & Mercer, J. R., *Synthesis, radiolabeling, and biodistribution of putative metabolites of iodoazomycin arabinoside.* Nuclear medicine and biology, 2000. **27**(1): p. 61–68.

152. Stypinski, D., Wiebe, L. I., McEwan, A. J., Schmidt, R. P., Tam, Y. K., & Mercer, J. R., *Clinical pharmacokinetics of 123I-IAZA in healthy volunteers.* Nuclear medicine communications, 1999. **20**(6): p. 559–567.

153. Stypinski, D., McQuarrie, S. A., Wiebe, L. I., Tam, Y. K., Mercer, J. R., & McEwan, A. J., *Dosimetry estimations for 123I-IAZA in healthy volunteers.* Journal of nuclear medicine: official publication, Society of Nuclear Medicine, 2001. **42**(9): p. 1418–1423.

154. Nawar, M.F., & Türler, A., *New strategies for a sustainable 99mTc supply to meet increasing medical demands: Promising solutions for current problems.* Frontiers in chemistry, 2022. **10**.

155. Linder, K.E., Chan, Y. W., Cyr, J. E., Malley, M. F., Nowotnik, D. P., & Nunn, A. D. , *TcO(PnA.O-1-(2-nitroimidazole)) [BMS-181321], a new technetium-containing nitroimidazole complex for imaging hypoxia: synthesis, characterization, and xanthine oxidase-catalyzed reduction.* Journal of medicinal chemistry, 1994. **37**(1): p. 9–17.

156. Kusuoka, H., Hashimoto, K., Fukuchi, K., & Nishimura, T., *Kinetics of a putative hypoxic tissue marker, technetium-99m-nitroimidazole (BMS181321), in normoxic, hypoxic, ischemic and stunned myocardium.* Journal of nuclear medicine : official publication, Society of Nuclear Medicine, 1994. **35**(8): p. 1371–1376.

157. Shi, C.Q., Sinusas, A. J., Dione, D. P., Singer, M. J., Young, L. H., Heller, E. N., Rinker, B. D., Wackers, F. J., & Zaret, B. L., *Technetium-99m-nitroimidazole (BMS181321): a positive imaging agent for detecting myocardial ischemia.* Journal of nuclear medicine : official publication, Society of Nuclear Medicine, 1995. **36**(6).

158. Rumsey, W.L., Kuczynski, B., Patel, B., Bauer, A., Narra, R. K., Eaton, S. M., Nunn, A. D., & Strauss, H. W., *SPECT imaging of ischemic myocardium using a technetium-99m-nitroimidazole ligand.* Journal of nuclear medicine : official publication, Society of Nuclear Medicine, 1995. **36**(8): p. 1445–1450.

159. Fukuchi, K., Kusuoka, H., Watanabe, Y., Fujiwara, T., & Nishimura, T., *Ischemic and reperfused myocardium detected with technetium-99m-nitroimidazole.* Journal of nuclear medicine : official publication, Society of Nuclear Medicine, 1996. **37**(5): p. 761–766.

160. Ballinger, J.R., Kee, J. W., & Rauth, A. M. (1996). *In vitro and in vivo evaluation of a technetium-99m-labeled 2-nitroimidazole (BMS181321) as a*

marker of tumor hypoxia. Journal of nuclear medicine : official publication, Society of Nuclear Medicine, 1996. **37**(6): p. 1023–1031.

161. Melo, T., Duncan, J., Ballinger, J. R., & Rauth, A. M., *BRU59-21, a second-generation 99mTc-labeled 2-nitroimidazole for imaging hypoxia in tumors.* Journal of nuclear medicine : official publication, Society of Nuclear Medicine, 2000. **41**(1): p. 169–176.

162. Zhang, X., Melo, T., Rauth, A. M., & Ballinger, J. R., *Cellular accumulation and retention of the technetium-99m-labelled hypoxia markers BRU59-21 and butylene amine oxime.* Nuclear medicine and biology, 2001. **28**(8): p. 949–957.

163. Hoebers, F.J., Janssen, H. L., Olmos, A. V., Sprong, D., Nunn, A. D., Balm, A. J., Hoefnagel, C. A., Begg, A. C., & Haustermans, K. M. (2002). , *Phase 1 study to identify tumour hypoxia in patients with head and neck cancer using technetium-99m BRU 59-21. .* European journal of nuclear medicine and molecular imaging, 2002. **29**(9): p. 1206–1211.

164. Preshlock, S., M. Tredwell, and V. Gouverneur, ^{18}*F-Labeling of Arenes and Heteroarenes for Applications in Positron Emission Tomography.* Chemical Reviews, 2016. **116**(2): p. 719-766.

165. Halder, R. and T. Ritter, ^{18}*F-Fluorination: Challenge and Opportunity for Organic Chemists.* The Journal of Organic Chemistry, 2021. **86**(20): p. 13873-13884.

166. Kim, D.W., et al., *Facile Nucleophilic Fluorination Reactions Using tert-Alcohols as a Reaction Medium: Significantly Enhanced Reactivity of Alkali Metal Fluorides and Improved Selectivity.* The Journal of Organic Chemistry, 2008. **73**(3): p. 957-962.

167. Roeda, D. and F. Dollé. *Recent Developments in the Chemistry of [*^{18}*F]Fluoride for PET*. 2014.

168. Zhou, D., et al., *[^{18}F]Tosyl fluoride as a versatile [^{18}F]fluoride source for the preparation of ^{18}F-labeled radiopharmaceuticals.* Scientific Reports, 2023. **13**(1): p. 3^{18}2.

169. Mossine, A.V., et al., *Development of customized [^{18}F] fluoride elution techniques for the enhancement of copper-mediated late-stage radiofluorination.* Scientific Reports, 2017. **7**(1): p. 233.

170. Lemaire, C.F., et al., *Fast Production of Highly Reactive No-Carrier-Added [^{18}F]Fluoride for the Labeling of Radiopharmaceuticals.* Angewandte Chemie International Edition, 2010. **49**(18): p. 3161-3164.

171. Maisonial-Besset, A., et al., *Base/Cryptand/Metal-Free Automated Nucleophilic Radiofluorination of [^{18}F]FDOPA from Iodonium Salts: Importance of Hydrogen Carbonate Counterion.* European Journal of Organic Chemistry, 2018. **20**18(48): p. 7058-7065.

172. Richarz, R., et al., *Neither azeotropic drying, nor base nor other additives: a minimalist approach to ^{18}F-labeling.* Organic & Biomolecular Chemistry, 2014. **12**(40): p. 8094-8099.

173. Orlovskaya, V., et al., *Tetrabutylammonium tosylate as inert phase-transfer catalyst: The key to high efficiency SN2 radiofluorinations.* Applied Radiation and Isotopes, 2020. **163**: p. 109195.

174. Fedorova, O., et al., *Automated synthesis of the 16α-[^{18}F] fluoroestradiol ([^{18}F]FES): Minimization of precursor amount and resulting benefits.* Radiochimica Acta, 2020. **108**: p. 979-988.

175. Coenen, H.H. and J. Ermert, *^{18}F-labelling innovations and their potential for clinical application.* Clinical and Translational Imaging, 2018. **6**(3): p. 169-193.

176. Graham, T.J.A., et al., *Enantioselective Radiosynthesis of Positron Emission Tomography (PET) Tracers Containing [^{18}F]Fluorohydrins.* Journal of the American Chemical Society, 2014. **136**(14): p. 5291-5294.

177. Taylor, N.J., et al., *Derisking the Cu-Mediated ^{18}F-Fluorination of Heterocyclic Positron Emission Tomography Radioligands.* Journal of the American Chemical Society, 2017. **139**(24): p. 8267-8276.

178. van der Born, D., et al., *Fluorine*-18 *labelled building blocks for PET tracer synthesis.* Chemical Society Reviews, 2017. **46**(15): p. 4709-4773.

179. Deng, X., Rong, J., Wang, L., Vasdev, N., Zhang, L., Josephson, L., & Liang, S. H., *Chemistry for Positron Emission Tomography: Recent Advances in 11 C-, ^{18}F-, 13 N-, and 15 O-Labeling Reactions.* Angewandte Chemie (International ed. in English), 2019. **58**(9): p. 2580–2605.

180. Way, J., & Wuest, F., *Fully automated synthesis of 4-[^{18}F]fluorobenzylamine based on borohydride/NiCl2 reduction.* Nuclear medicine and biology, 2013. **40**(3): p. 430–436. .

181. Heinz, E.J.a.H.C., *No-Carrier-Added [^{18}F]Fluorobenzene Derivatives as Intermediates for Built-up Radiosyntheses.* Current Radiopharmaceuticals, 2010. **3**(2).

182. Shen, B., Ehrlichmann, W., Uebele, M., Machulla, H. J., & Reischl, G. (2009). . , 67(9), , *Automated synthesis of n.c.a. [^{18}F]FDOPA via nucleophilic aromatic substitution with [^{18}F]fluoride.* Applied radiation and isotopes : including data, instrumentation and methods for use in agriculture, industry and medicine,, 2009. **67**(9): p. 1650–1653.

183. Coenen, H. and J. Ermert, *Direct Nucleophilic ^{18}F-Fluorination of Electron Rich Arenes: Present Limits of No-Carrier-Added Reactions.* Current Radiopharmaceuticals, 2010. **3**: p. 163-173.

184. Pike, V.W. and F.I. Aigbirhio, *Reactions of cyclotron-produced [^{18}F]fluoride with diaryliodonium salts—a novel single-step route to no-carrier-added [*18*]fluoroarenes.* Journal of the Chemical Society, Chemical Communications, 1995(21): p. 2215-2216.

185. W., P.V., *Hypervalent aryliodine compounds as precursors for radiofluorination.* Journal of labelled compounds & radiopharmaceuticals, 20^{18}. **61**(3): p. 196–227.

186. Mu, L., et al., *^{18}F-Radiolabeling of Aromatic Compounds Using Triarylsulfonium Salts.* European Journal of Organic Chemistry, 2012. **2012**.

187. Ermert, J., et al., *Comparison of pathways to the versatile synthon of no-carrier-added 1-bromo-4-[^{18}F]fluorobenzene.* Journal of Labelled Compounds and Radiopharmaceuticals, 2004. **47**: p. 429-441.

188. Wuest, F. and T. Kniess, *Synthesis of 4-[^{18}F]fluoroiodobenzene and its application in Sonogashira cross-coupling reactions.* Journal of Labelled Compounds and Radiopharmaceuticals, 2003. **46**: p. 699-713.

189. Ross, T.L., et al., *Nucleophilic ^{18}F-Fluorination of Heteroaromatic Iodonium Salts with No-Carrier-Added [^{18}F]Fluoride.* Journal of the American Chemical Society, 2007. **129**(25): p. 80^{18}-8025.

190. Woodfield, J., V. Bouvet, and F. Wuest, *ChemInform Abstract: Synthesis of 4-[^{18}F]Fluorohalobenzenes and Palladium-mediated Cross-coupling Reactions for the Synthesis of ^{18}F-Labeled Radiotracers.* ChemInform, 2014. **45**.

191. Woodfield, J. and F. Wuest, *Automated radiosynthesis of no-carrier-added 4-[^{18}F] fluoroiodobenzene: A versatile building block in ^{18}F radiochemistry.* Journal of labelled compounds & radiopharmaceuticals, 2014. **57**: p. 104-9.

192. Chun, J.-H. and V.W. Pike, *Single-step syntheses of no-carrier-added functionalized [^{18}F]fluoroarenes as labeling synthons from diaryliodonium salts.* Organic & Biomolecular Chemistry, 2013. **11**(37): p. 6300-6306.

193. Telu, S., et al., *Syntheses of mGluR5 PET radioligands through the radiofluorination of diaryliodonium tosylates.* Organic & Biomolecular Chemistry, 2011. **9**(19): p. 6629-6638.

194. Jacobson, O., D.O. Kiesewetter, and X. Chen, *Fluorine*-18 *Radiochemistry, Labeling Strategies and Synthetic Routes.* Bioconjugate Chemistry, 2015. **26**(1): p. 1-^{18}.

195. Cardinale, J., et al., *Carrier-effect on palladium-catalyzed, nucleophilic ^{18}F-fluorination of aryl triflates.* Journal of Labelled Compounds and Radiopharmaceuticals, 2012. **55**(12): p. 450-453.

196. Lee, E., Kamlet, A. S., Powers, D. C., Neumann, C. N., Boursalian, G. B., Furuya, T., Choi, D. C., Hooker, J. M., & Ritter, T. (2011). *A fluoride-derived electrophilic late-stage fluorination reagent for PET imaging.* Science (New York, N.Y.), 2011. **334**: p. 639–642.

197. Lee, E., J.M. Hooker, and T. Ritter, *Nickel-Mediated Oxidative Fluorination for PET with Aqueous [^{18}F] Fluoride.* Journal of the American Chemical Society, 2012. **134**(42): p. 17456-17458.

198. Zlatopolskiy, B.D., et al., *A Practical One-Pot Synthesis of Positron Emission Tomography (PET) Tracers via Nickel-Mediated Radiofluorination.* ChemistryOpen, 2015. **4**(4): p. 457-462.

199. Tredwell, M., Preshlock, S. M., Taylor, N. J., Gruber, S., Huiban, M., Passchier, J., Mercier, J., Génicot, C., & Gouverneur, V., *A general copper-mediated nucleophilic ^{18}F fluorination of arenes.* Angewandte Chemie (International ed. in English), 2014. **53**(30): p. 7751–7755.

200. Mossine, A.V., et al., *Synthesis of [^{18}F]Arenes via the Copper-Mediated [^{18}F]Fluorination of Boronic Acids.* Organic Letters, 2015. **17**(23): p. 5780-5783.

201. Zhang, Z., et al., *Synthesis and evaluation of ^{18}F-labeled CJ-042794 for imaging prostanoid EP4 receptor expression in cancer with positron emission tomography.* Bioorganic & Medicinal Chemistry Letters, 2017. **27**(10): p. 2094-2098.

202. Tang, T., et al., *Preparation and evaluation of L- and D-5-[^{18}F]fluorotryptophan as PET imaging probes for indoleamine and tryptophan 2,3-dioxygenases.* Nuclear Medicine and Biology, 2017. **51**: p. 10-17.

203. Giglio, B., et al., *Synthesis of 5-[F]Fluoro-α-methyl Tryptophan: New Trp Based PET Agents.* Theranostics, 2017. **7**: p. 1524-1530.

204. Campbell, M.G. and T. Ritter, *Late-Stage Fluorination: From Fundamentals to Application.* Organic Process Research & Development, 2014. ^{18}(4): p. 474-480.

205. Mossine, A.V., Brooks, A. F., Makaravage, K. J., Miller, J. M., Ichiishi, N., Sanford, M. S., & Scott, P. J., *Synthesis of [^{18}F]Arenes via the Copper-Mediated [^{18}F]Fluorination of Boronic Acids.* Organic Letters, 2015. **17**(23): p. 5780–5783.

206. Valdez, C.A., Tripp, J. C., Miyamoto, Y., Kalisiak, J., Hruz, P., Andersen, Y. S., Brown, S. E., Kangas, K., Arzu, L. V., Davids, B. J., Gillin, F. D., Upcroft, J. A., Upcroft, P., Fokin, V. V., Smith, D. K., Sharpless, K. B., & Eckmann, L., *Synthesis and electrochemistry of 2-ethenyl and 2-ethanyl derivatives of 5-nitroimidazole and antimicrobial activity against Giardia lamblia.* Journal of medicinal chemistry, 2009. **52**(13): p. 4038–4053.

207. Tawari, N.R., Bairwa, R., Ray, M. K., Rajan, M. G., & Degani, M. S., *Design, synthesis, and biological evaluation of 4-(5-nitrofuran-2-yl)prop-2-en-1-one derivatives as potent antitubercular agents.* Bioorganic & medicinal chemistry letters, 2010. **20**(21): p. 6175–6178.

208. Tawari, N.R. and M.S. Degani, *Pharmacophore modeling and density functional theory analysis for a series of nitroimidazole compounds with antitubercular activity.* Chemical biology & drug design, 2011. **78**(3): p. 408-417.

209. Chai, W.L.F.A.a.C.L.L., *Purification of Laboratory Chemicals*. 6th Edition ed. 2009.

210. Lahdenpohja, S.O., et al., *Fast and efficient copper-mediated ^{18}F-fluorination of arylstannanes, aryl boronic acids, and aryl boronic esters without azeotropic drying.* EJNMMI Radiopharmacy and Chemistry, 2019. **4**(1): p. 28.

211. Chen, W., et al., *Arene radiofluorination enabled by photoredox-mediated halide interconversion.* Nature Chemistry, 2022. **14**(2): p. 216-223.

212. Barthel, H., et al., *In vivo evaluation of [^{18}F]fluoroetanidazole as a new marker for imaging tumour hypoxia with positron emission tomography.* British Journal of Cancer, 2004. **90**(11): p. 2232-2242.

213. Wei, H., Li, D., Yang, X., Shang, H., Fan, S., Li, Y., & Song, D., *Design and Synthesis of Vandetanib Derivatives Containing Nitroimidazole Groups as Tyrosine Kinase Inhibitors in Normoxia and Hypoxia.* Molecules, 2016. **21**(12): p. 1693.

214. Mevellec, L.A., Pasquier, Elisabeth T. J., Descamps, S., Mercey, G. J. M., Wroblowski, B., Vialard, J. E., Meerpoel, L., Jeanty, Matthieu L., Jousseaume, Thierry Francois A. J., *Preparation of substituted 4,5,6,7-tetrahydro-pyrazolo[1,5-a]pyrazine derivatives and 5,6,7,8-tetrahydro-4H-pyrazolo[1,5-a][1,4]diazepine derivatives as ROS1 inhibitors*. 2015, Janssen Pharmaceutica NV, Belgium. p. 287.

215. Verma, S.K., et al., *Solvent free, N,N'-carbonyldiimidazole (CDI) mediated amidation.* Tetrahedron Letters, 2012. **53**(19): p. 2373-2376.

216. Larrivée-Aboussafy, C., et al., *DBU Catalysis of N,N'-Carbonyldiimidazole-Mediated Amidations.* Organic Letters, 2010. **12**(2): p. 324-327.

217. Haas, B., et al., *Predicting relative efficiency of amide bond formation using multivariate linear regression.* Proceedings of the National Academy of Sciences, 2022. **119**.

218. Métro, T.-X., et al., *Comprehensive Study of the Organic-Solvent-Free CDI-Mediated Acylation of Various Nucleophiles by Mechanochemistry.* Chemistry – A European Journal, 2015. **21**(36): p. 12787-12796.

219. Taimoory, S.M., Sadraei, S. I., Fayoumi, R. A., Nasri, S., Revington, M., & Trant, J. F., *Preparation and Characterization of a Small Library of Thermally-Labile End-Caps for Variable-Temperature Triggering of Self-Immolative Polymers.* The Journal of Organic Chemistry, 20^{18}. **83**(8): p. 4427–4440.

220. Mohammadpoor-Baltork, I., Alivan, H.;, *Efficient and selective deprotection of aryl aldehyde diacetates catalyzed by tin(II) chloride dihydrate.* Indian Journal of Chemistry, Section B: Organic Chemistry Including Medicinal Chemistry, 1999. **38B**(10): p. 1223-1225.

221. Mo, F., et al., *Direct Conversion of Arylamines to Pinacol Boronates: A Metal-Free Borylation Process.* Angewandte Chemie International Edition, 2010. **49**(10): p. 1846-^{18}49.

222. Doyle, M.P., Siegfried, B. and Dellaria Jr., J.F., *Alkyl Nitrite-Metal Halide Deamination Reactions. 2. Substitutive Deamination of Arylamines by Alkyl Nitrites and Copper(II) Halides. A Direct and Remarkably Efficient Conversion of Arylamines to Aryl Halides.* The Journal of Organic Chemistry, 1977. **42**: p. 2426-2429.

223. Qiu, D., Jin, L., Zheng, Z., Meng, H., Mo, F., Wang, X., Zhang, Y., & Wang, J., *The Journal of organic chemistry.* Synthesis of pinacol arylboronates from aromatic amines: a metal-free transformation, 2013. **78**(5): p. 1923–1933.

224. Vraka, C., et al., *LogP, a yesterday's value?* Nuclear Medicine and Biology, 2017. **50**: p. 1-10.

225. Morand, P., et al., *Hypoxia-specific tumor imaging with 18F-fluoroazomycin arabinoside.* Journal of Nuclear Medicine, 2005. **46**(1): p. 106.

226. Uzuegbunam, B.C., D. Librizzi, and B. Hooshyar Yousefi *PET Radiopharmaceuticals for Alzheimer's Disease and Parkinson's Disease Diagnosis, the Current and Future Landscape*. Molecules, 2020. **25**, DOI: 10.3390/molecules25040977.

227. PÉREZ NARIO, A., *Síntese e caracterização pré-clínica de um novo derivado de 2-nitroimidazol como potencial traçador PET para imagem de hipóxia tumoral.*, in *Doutorado em Tecnologia Nuclear*. 2020: Instituto de Pesquisas Energéticas e Nucleares, IPEN-CNEN/SP, São Paulo. p. 160.

228. Mohamed, M.F.A. and G.E.-D.A. Abuo-Rahma, *Molecular targets and anticancer activity of quinoline–chalcone hybrids: literature review.* RSC Advances, 2020. **10**(52): p. 31139-31155.

229. Maydt, D., et al., *Chemical reactivity and biological activity of chalcones and other α,β-unsaturated carbonyl compounds.* Xenobiotica, 2013. **43**(8): p. 711-718.

230. Zhuang, C., et al., *Chalcone: A Privileged Structure in Medicinal Chemistry.* Chemical Reviews, 2017. **117**(12): p. 7762-7810.

231. Dhillon, S., et al., *Advances in Aβ imaging probes: a comprehensive study of radiolabelled 1,3-diaryl-2-propen-1-ones for Alzheimer's disease: a review.* RSC Advances, 2023. **13**: p. 35877-35903.

232. Capponi, P.C., Mari, M., Ferrari, E., & Asti, M., *Radiolabeled Chalcone Derivatives as Potential Radiotracers for β-Amyloid Plaques Imaging.* Molecules (Basel, Switzerland), 2023. **28**(7).

233. Ono, K., et al., *Curcumin has potent anti-amyloidogenic effects for Alzheimer's β-amyloid fibrils in vitro.* Journal of Neuroscience Research, 2004. **75**(6): p. 742-750.

234. Yang, F., Lim, G. P., Begum, A. N., Ubeda, O. J., Simmons, M. R., Ambegaokar, S. S., Chen, P. P., Kayed, R., Glabe, C. G., Frautschy, S. A., & Cole, G. M., *Curcumin inhibits formation of amyloid beta oligomers and fibrils, binds plaques, and reduces amyloid in vivo.* The Journal of biological chemistry, 2005. **280**(7): p. 5892–5901.

235. Mari, M., et al., *Applications of Radiolabelled Curcumin and Its Derivatives in Medicinal Chemistry.* International Journal of Molecular Sciences, 2021. **22**(14): p. 7410.

236. Wongso, H., *Natural product-based radiopharmaceuticals: Focus on curcumin and its analogs, flavonoids, and marine peptides.* Journal of Pharmaceutical Analysis, 2022. **12**(3): p. 380-393.

237. Zeng, F., & Goodman, M. M., *Fluorine*-18 *radiolabeled heterocycles as PET tracers for imaging β-amyloid plaques in Alzheimer's disease.* Current topics in medicinal chemistry, 2013. **13**(8): p. 909–919.

238. Allott, L., et al., *Development of a fluorine*-18 *radiolabelled fluorescent chalcone: evaluated for detecting glycogen.* EJNMMI Radiopharmacy and Chemistry, 2020. **5**.

239. Stempien-Otero, A., et al., *Mechanisms of Hypoxia-induced Endothelial Cell Death: ROLE OF p53 IN APOPTOSIS*.* Journal of Biological Chemistry, 1999. **274**(12): p. 8039-8045.

9. ANNEXES

Annex A. ^{1}H-NMR tert-butyl 2-(2-nitro-1H-imidazol-1-yl)acetate.

(300 MHz, Chloroform-d) δ 7.17 (d, J=0.96 Hz, 1H); 7.10 (d, J=0.96 Hz, 1H), 5.01 (s, 2H), 1.46 (s, 9H).

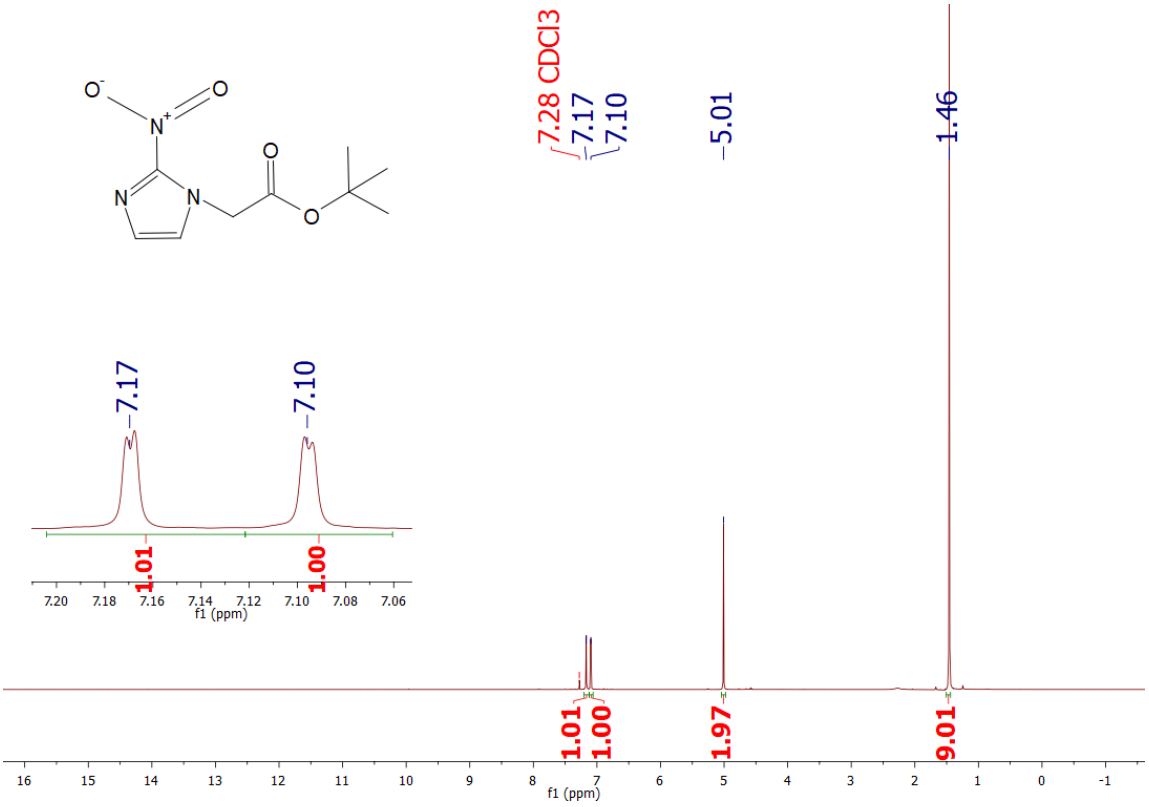

Annex B. ^{1}H-NMR 2-(2-nitro-1H-imidazol-1-yl)acetic acid (300 MHz, Methanol-d4) δ 7.32 (s, 1H), 7.03 (s, 1H), 5.10 (s, 2H).

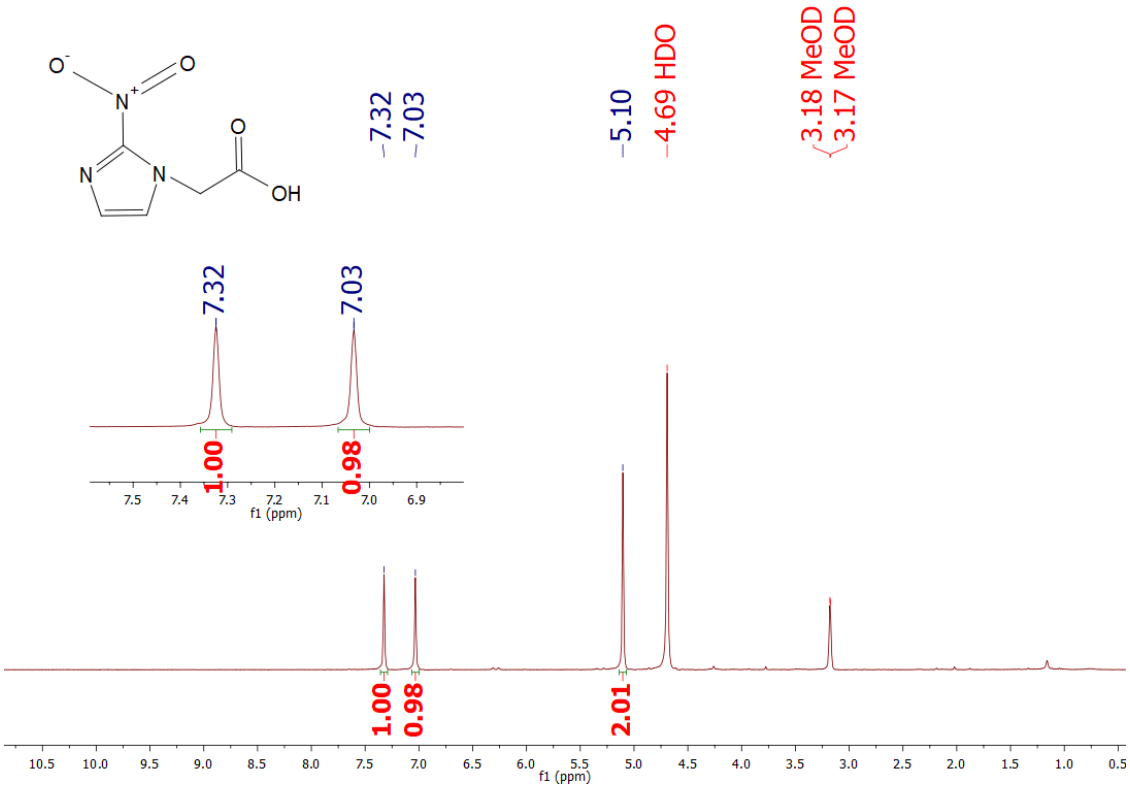

Annex C. ^{1}H-NMR N-(4-fluorobenzyl)-2-(2-nitro-1H-imidazol-1-yl)acetamide (600 MHz, DMSO-d6) δ 8.84 (t, J = 5.5 Hz, 1H); 7.64 (s, 1H); 7.32 (dd, J = 8.2, 5.8 Hz, 2H); 7.20 (s, 1H), 7.17 (d, J = 8.2 Hz, 2H); 5.17 (s, 2H), 4.32 (d, J = 5.5 Hz, 2H).

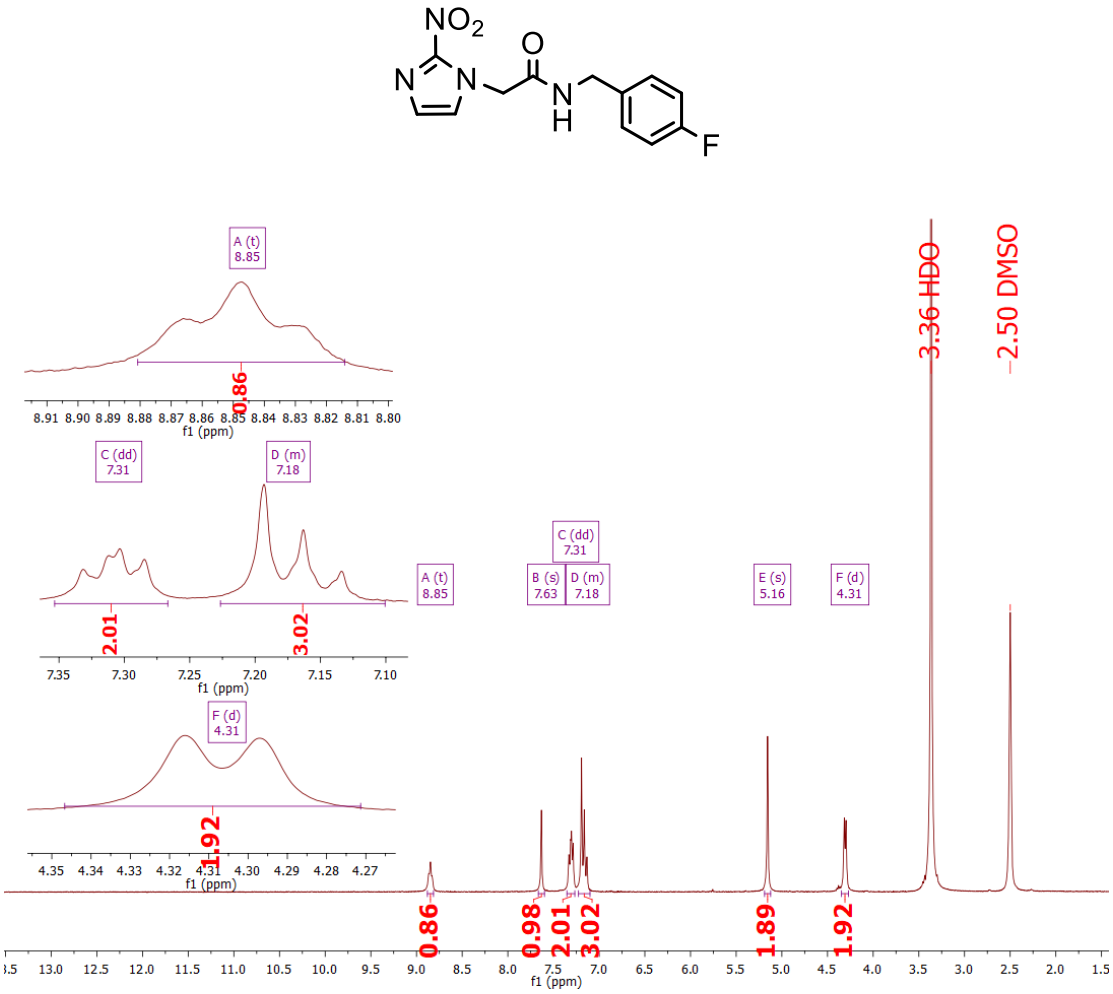

Annex D. (4-((2-(2-nitro-1H-imidazol-1-yl)acetamido)methyl)phenyl)boronic acid pinacol ester ^{1}H-NMR (600 MHz, DMSO-d6) δ 8.87 (t, J = 5.9 Hz, 1H), 7.65 (d, J = 8.0 Hz, 2H), 7.63 (s, 1H), 7.30 (d, J = 8.0 Hz, 2H), 7.20 (s, 1H), 5.[18] (s, 2H), 4.35 (d, J = 5.9 Hz, 2H), 1.30 (s, 12H).

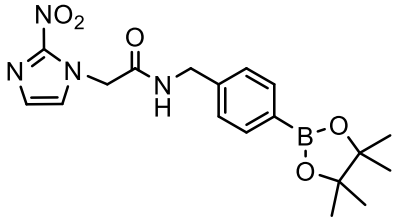

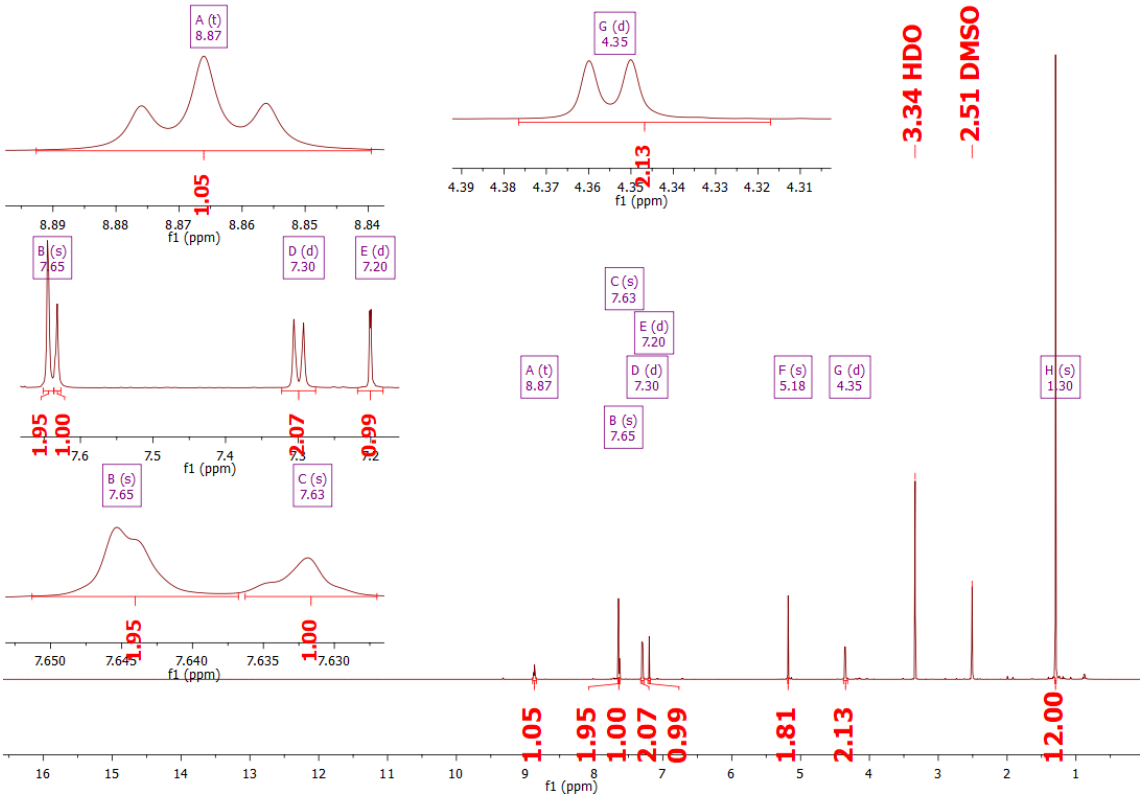

Annex E. (4-((2-(2-nitro-1H-imidazol-1-yl)acetamido)methyl)phenyl)boronic acid pinacol ester ^{13}C-NMR DEPTQ (151 MHz, DMSO-d_6) δ 167.44, 166.22, 145.40, 142.85, 134.93, 129.28, 127.94, 127.13, 84.07, 52.06, 42.80, 25.14.

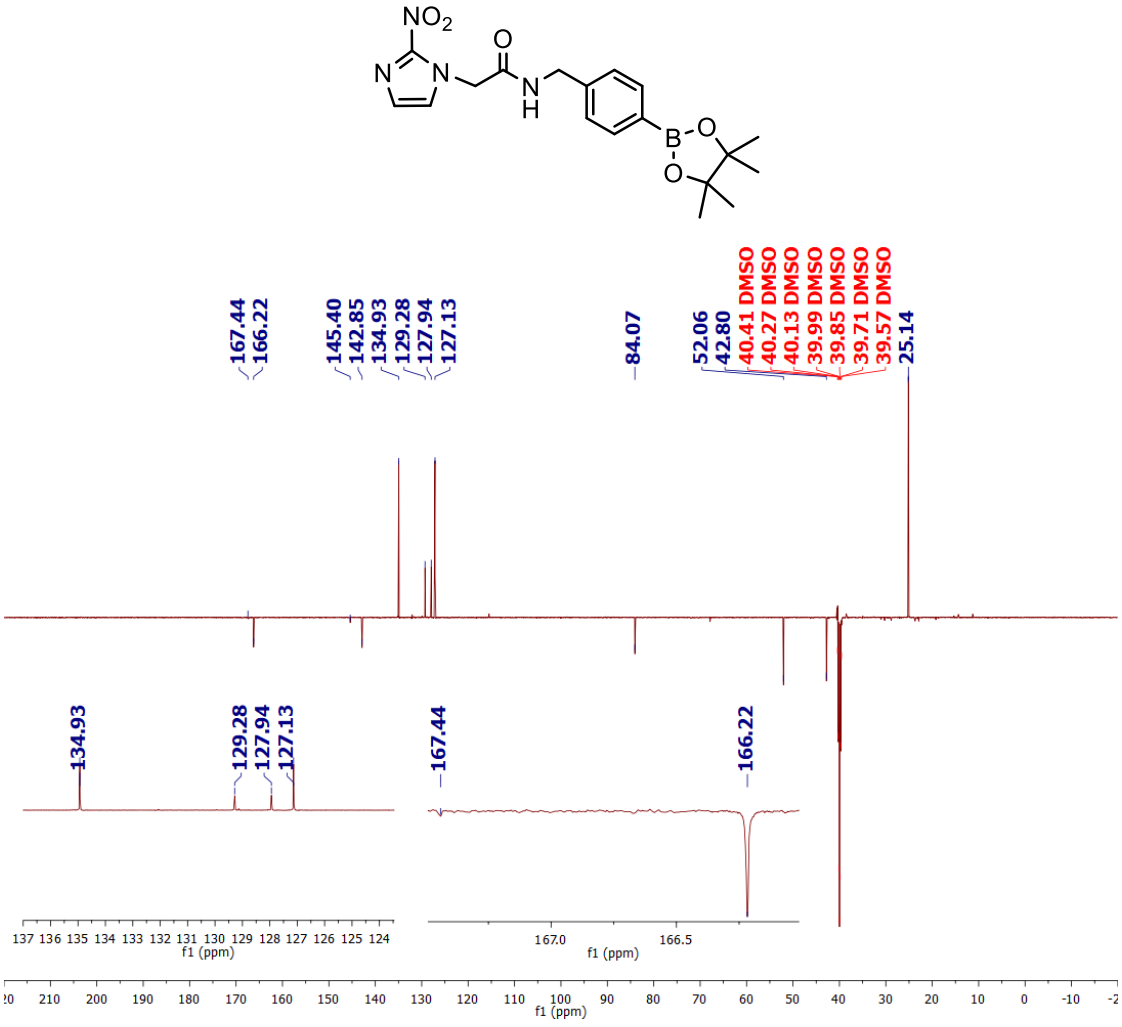

Annex F. ion trap mass spectrometry of (4-((2-(2-nitro-1H-imidazol-1-yl)acetamido)methyl)phenyl)boronic acid pinacol ester, MW= 386,20 g/mol.

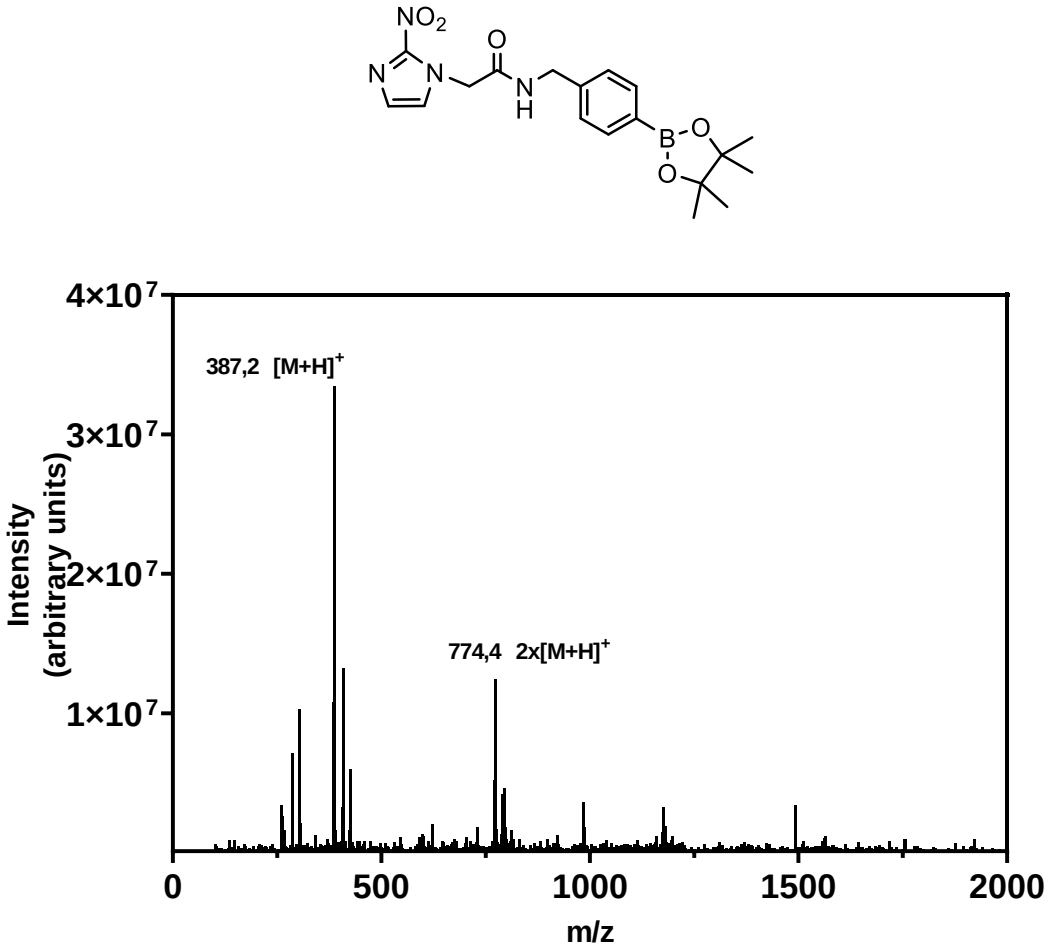

Annex G. Infrared spectra of (4-((2-(2-nitro-1H-imidazol-1-yl)acetamido)methyl)phenyl)boronic acid pinacol ester.

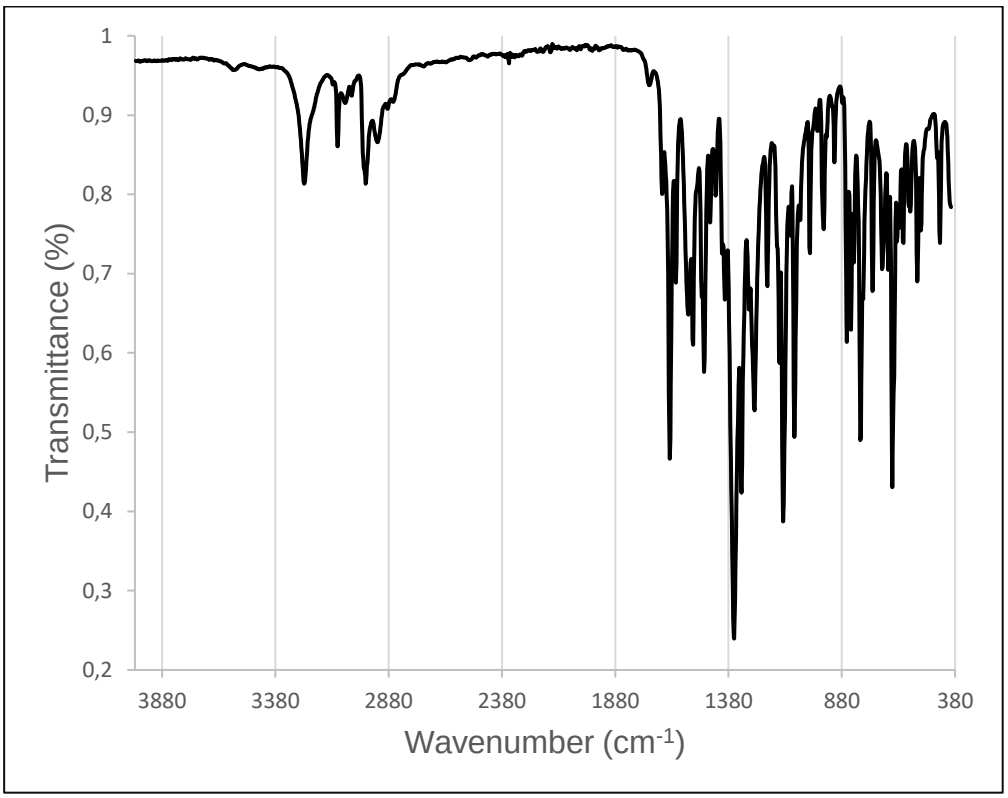

Annex H. 5-nitro-2-furaldehyde diacetate ^{1}H NMR (300 MHz, Chloroform-d) δ 7.73 (s, 1H), 7.30 (d, J = 3.6 Hz, 1H), 6.75 (d, J = 3.6 Hz, 1H), 2.19 (s, 6H);

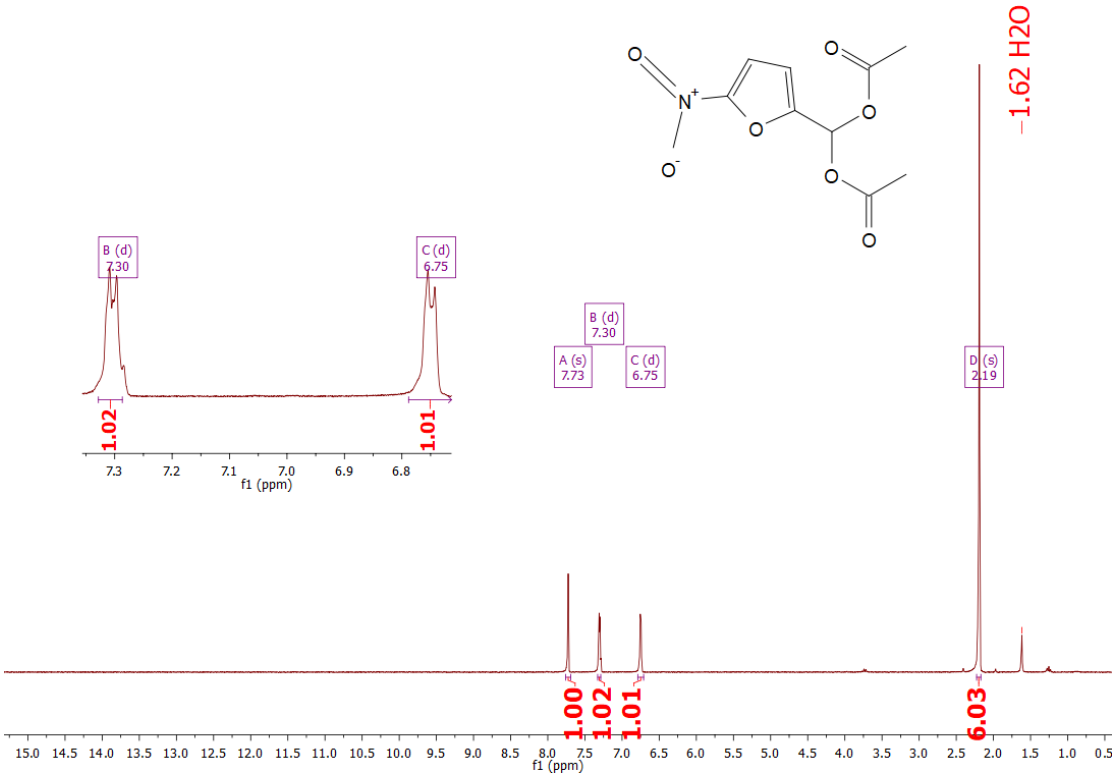

Annex I. 5-nitro-2-furaldehyde ^{1}H NMR (600 MHz, Chloroform-*d*) δ 9.85 (s, 1H), 7.44 (dd, *J* = 3.8, 0.4 Hz, 1H), 7.38 (d, *J* = 3.8 Hz, 1H).

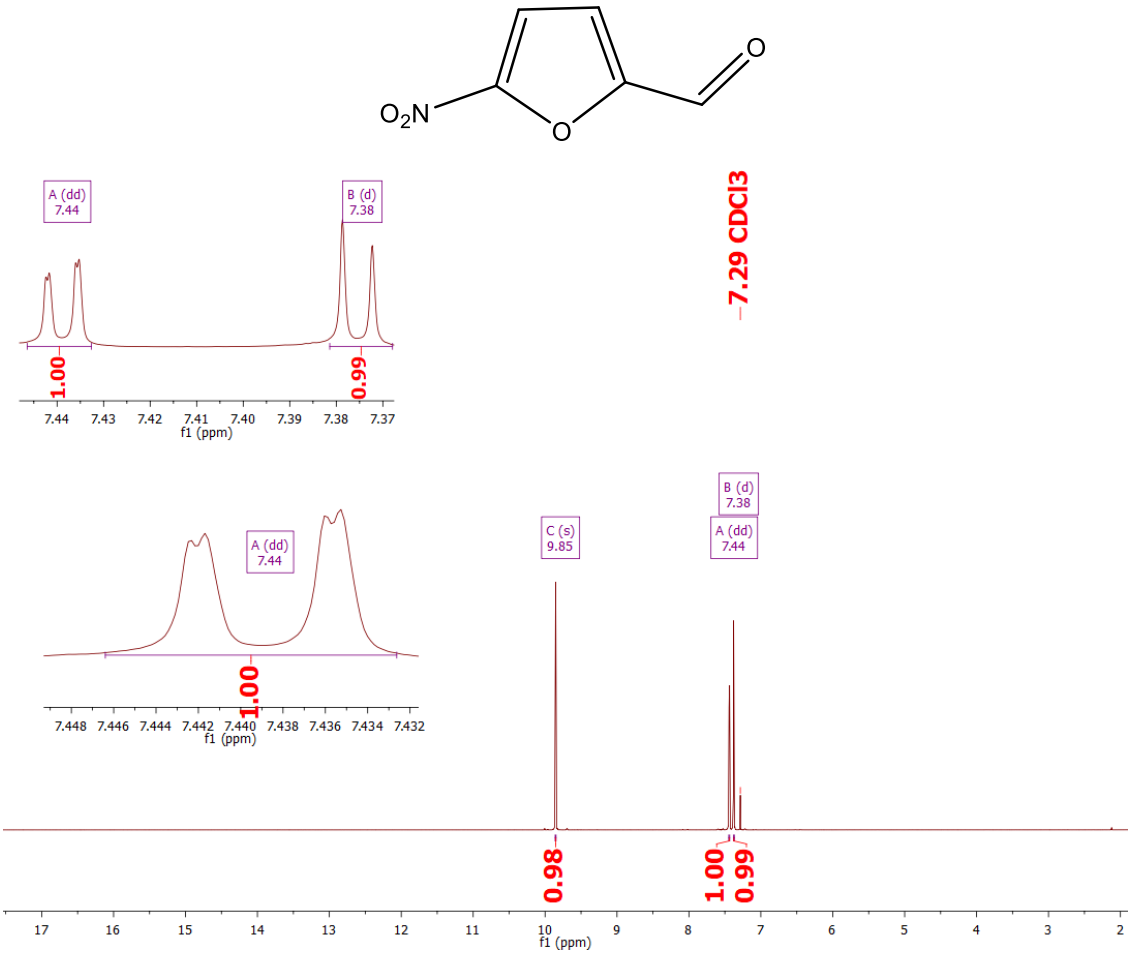

Annex J. (E)-1-(4-fluorophenyl)-3-(5-nitrofuran-2-yl)prop-2-en-1-one. **^{1}H NMR** (600 MHz, DMSO-d_6) δ 8.26 – 8.20 (m, 2H), 7.89 (d, *J* = 15.6 Hz, 1H), 7.83 (d, *J* = 3.9 Hz, 1H), 7.61 (d, *J* = 15.6 Hz, 1H), 7.47 (d, *J* = 3.9 Hz, 1H), 7.45 – 7.41 (m, 2H).

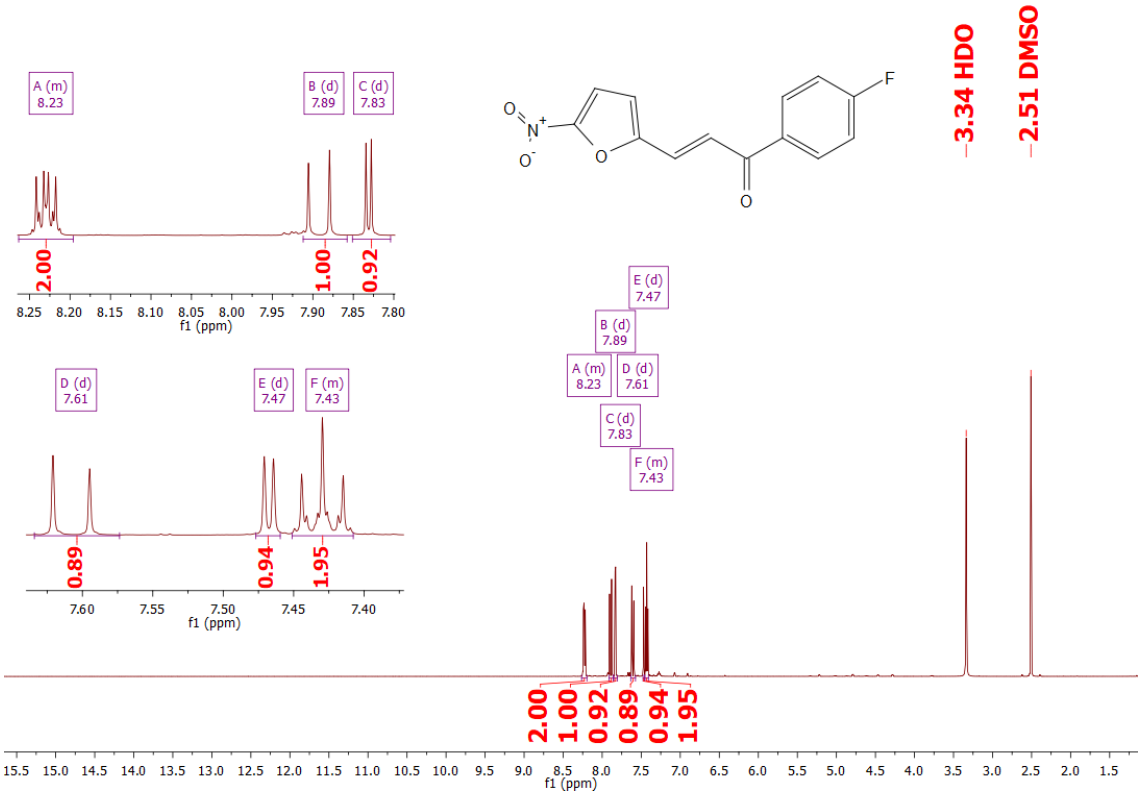

Annex K. 4-acetylphenylboronic acid pinacol ester **^{1}H NMR** (600 MHz, Chloroform-d) δ 7.85 – 7.77 (m, 4H), 2.51 (s, 3H), 1.26 (s, 12H).

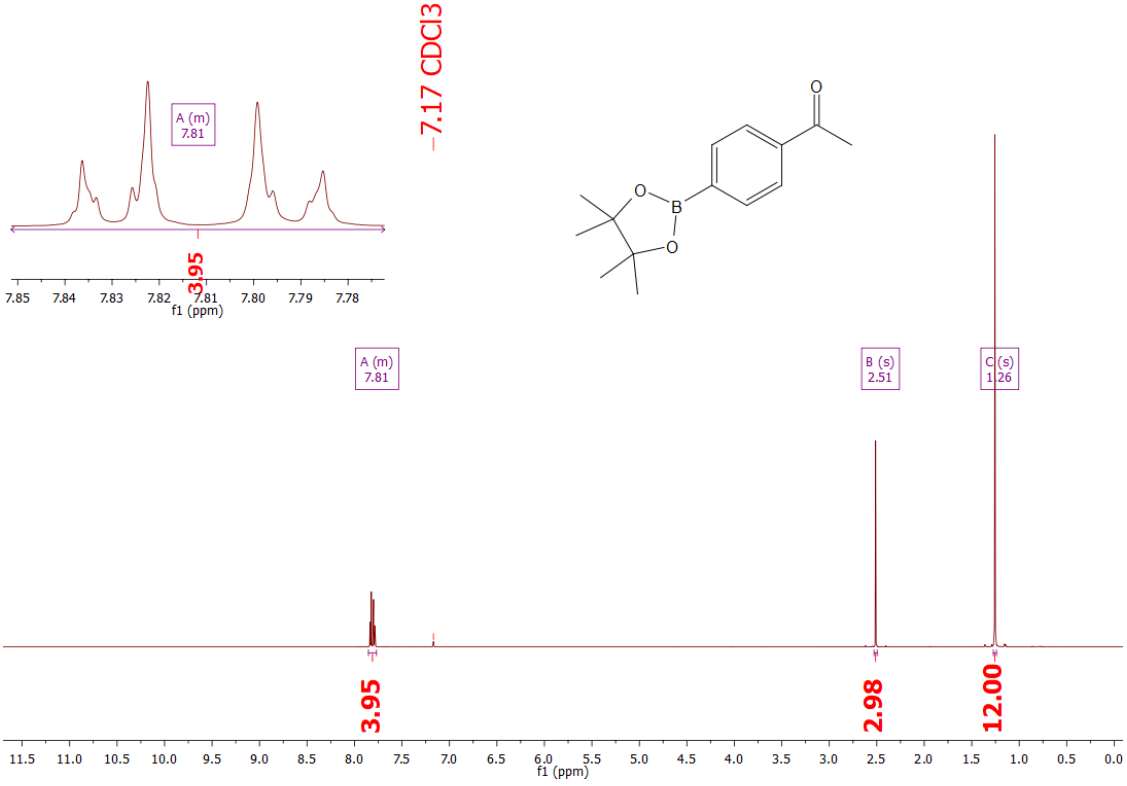

Annex J. (E)-(4-(3-(5-nitrofuran-2-yl)acryloyl)phenyl)boronic acid pinacol ester. ^{1}H NMR (600 MHz, DMSO-d_6) δ 8.12 – 8.10 (m, 2H), 7.89 – 7.84 (m, 3H), 7.83 (d, J = 3.9 Hz, 1H), 7.62 (d, J = 15.6 Hz, 1H), 7.47 (d, J = 3.9 Hz, 1H), 1.33 (s, 12H).

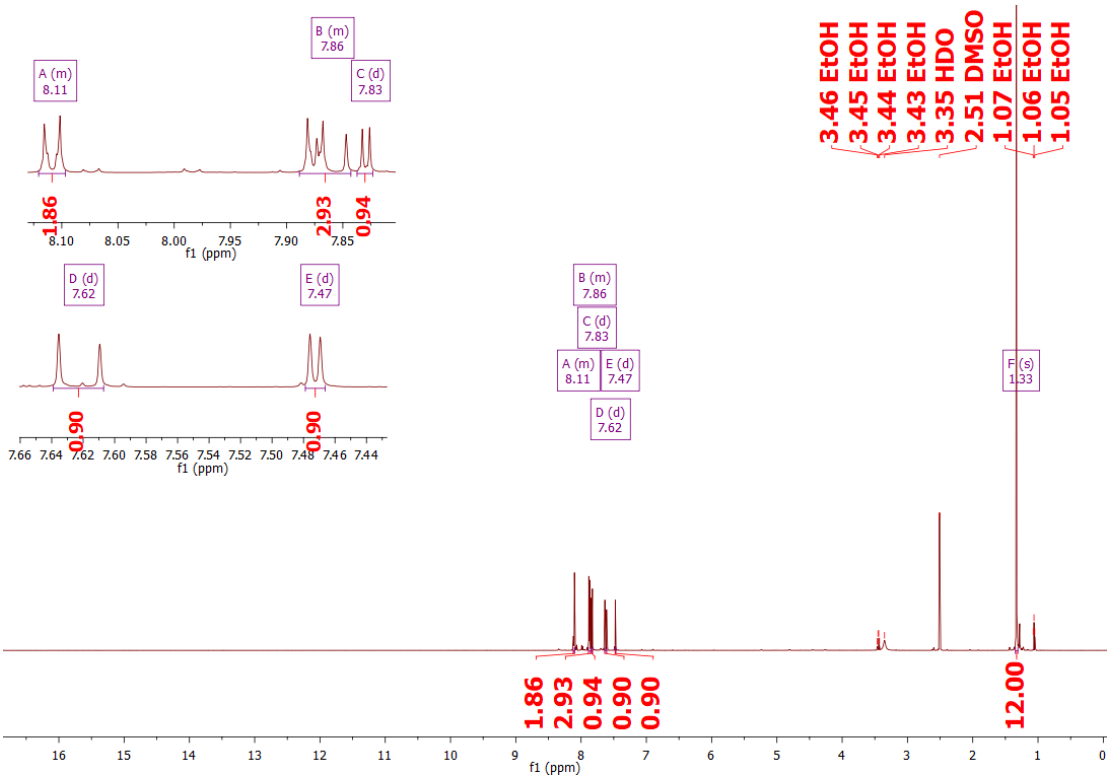

Annex K. (E)-(4-(3-(5-nitrofuran-2-yl)acryloyl)phenyl)boronic acid pinacol ester. **^{13}C-NMR DEPTQ** (151 MHz, DMSO) δ 188.89, 153.60, 152.50, 139.30, 135.30, 129.41, 128.28, 125.31, 118.52, 115.26, 84.62, 25.15.

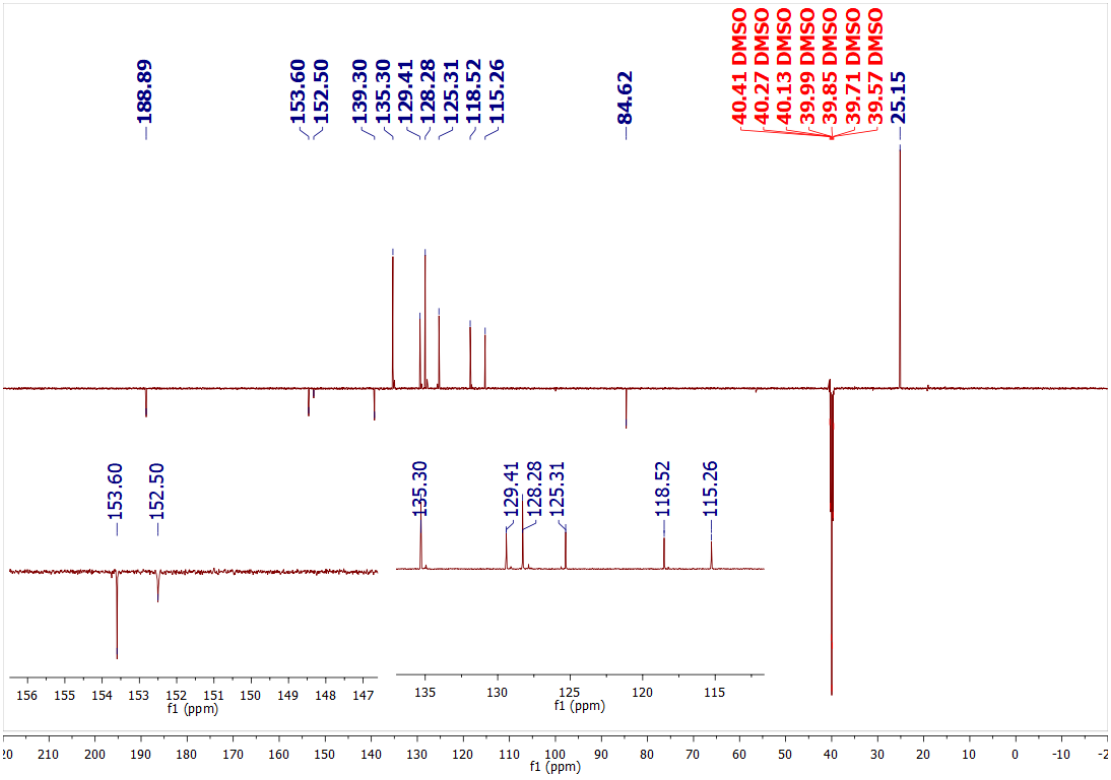

Anex L. (E)-(4-(3-(5-nitrofuran-2-yl)acryloyl)phenyl)boronic acid pinacol ester. **ESI-mass spectrometry**. MW=369,18 g/mol.

User Spectra

Fragmentor Voltage	Collision Energy	Ionization Mode
200	0	Esi

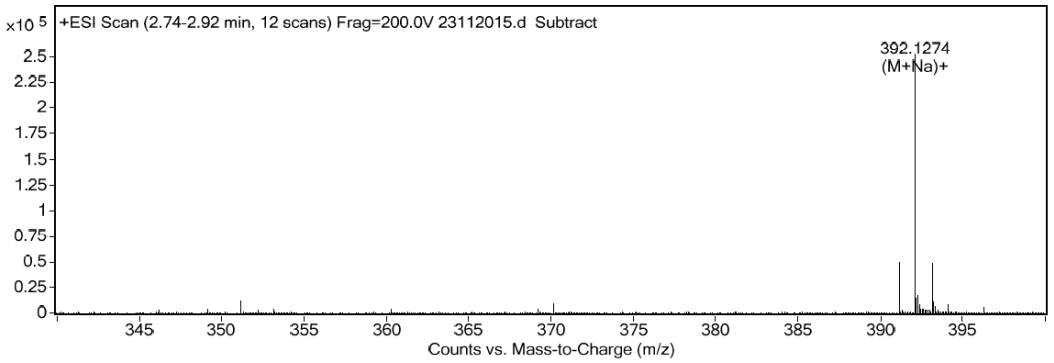

Formula Calculator Results

Formula	Ion Formula	Mass	Calc Mass	m/z	Calc. m/z	Diff (mDa)	Diff (ppm)	DBE	Ion Species
C19 H20 [11B] N O6	C19 H20 [11B] N Na O6	369.1382	369.1384	392.1274	392.1276	0.17	0.43	11	(M+Na)+

Anex M. Infrarred spectra of (E)-(4-(3-(5-nitrofuran-2-yl)acryloyl)phenyl)boronic acid pinacol ester

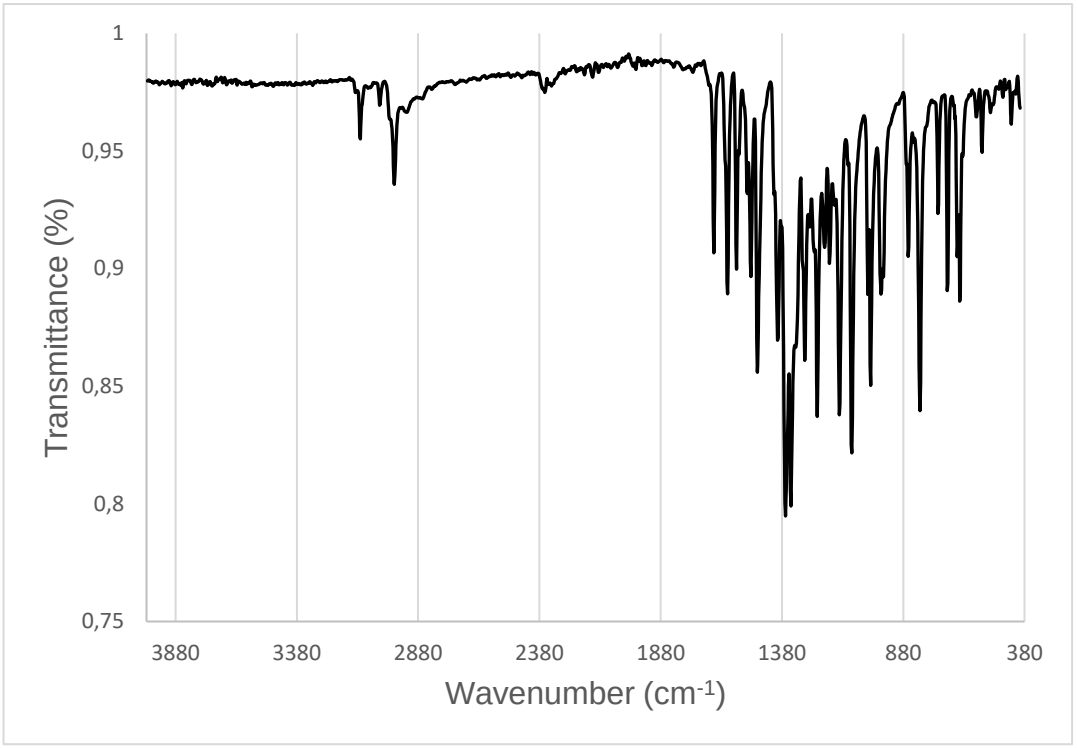

INSTITUTO DE PESQUISAS ENERGÉTICAS E NUCLEARES
Diretoria de Pesquisa, Desenvolvimento e Ensino
Av. Prof. Lineu Prestes, 2242 – Cidade Universitária CEP: 05508-000
Fone/Fax(0XX11) 3133-8908
SÃO PAULO – São Paulo – Brasil
http://www.ipen.br

O IPEN é uma Autarquia vinculada à Secretaria de Desenvolvimento, associada à Universidade de São Paulo e gerida técnica e administrativamente pela Comissão Nacional de Energia Nuclear, órgão do Ministério da Ciência, Tecnologia, Inovações e Comunicações.